

# Calculation of the electronic and optical properties of colloidal nanostructures using the comprehensive method based on atomic effective pseudopotentials

Dissertation  
with the aim of achieving a doctoral degree  
at the Faculty of Mathematics, Informatics and Natural Sciences  
Department of Chemistry  
University of Hamburg



Anastasia Karpulevich

February, 2020



The present work was carried out in the period from October 2015 till February 2020 in the Institute of Physical Chemistry at the University of Hamburg in the group of Prof. Dr. Gabriel Bester.

The recommended experts:

Prof. Dr. Gabriel Bester, the University of Hamburg

Prof. Dr. Horst Weller, the University of Hamburg

Date of disputation: 15.05.2020



# Contents

<b>Abstract</b>	<b>vii</b>
<b>Zusammenfassung</b>	<b>ix</b>
<b>List of publications</b>	<b>xi</b>
<b>List of abbreviations</b>	<b>xiii</b>
<b>1 Introduction</b>	<b>1</b>
1.1 Crystal lattice in solid state physics . . . . .	1
1.2 Semiconductor materials . . . . .	2
1.3 Semiconductor nanostructures and their applications . . . . .	4
<b>2 Computational methods</b>	<b>7</b>
2.1 Many-body Hamiltonian . . . . .	7
2.2 Density functional theory . . . . .	9
2.2.1 Exchange-correlation functionals . . . . .	11
2.2.2 Plane wave basis and pseudopotentials . . . . .	12
2.3 Atomic effective pseudopotentials . . . . .	14
2.4 Configuration interaction theory . . . . .	19
2.5 Single-particle, quasiparticle and optical band gaps . . . . .	20
2.5.1 Exciton fine structure . . . . .	22
<b>3 Motivation</b>	<b>25</b>
<b>4 Method development</b>	<b>27</b>
4.1 Nanocrystals: structure and relaxation . . . . .	27
4.1.1 Valence force field model for core-shell QDs . . . . .	29
4.2 Non-spherical atomic effective pseudopotentials for passivant atoms	31
4.2.1 Passivant potential derivation . . . . .	32
4.2.2 Passivant potentials for different crystallographic directions .	37

4.2.3	Atomistically passivated Si nanostructures . . . . .	38
4.2.4	Atomistic passivation for other semiconductor materials . . .	43
4.3	Correction of the single-particle band gap . . . . .	45
4.3.1	$\beta$ -correction influence on the bulk band structure and $e/h$ effective masses . . . . .	45
4.3.2	$\beta$ -correction for the band offsets in core-shell QDs . . . . .	48
4.3.3	$\beta$ -correction influence on the wave functions . . . . .	49
4.4	Dielectric screening function for colloidal QDs . . . . .	51
4.4.1	Constant screening . . . . .	52
4.4.2	Microscopic screening . . . . .	52
4.4.3	Modified Penn model for $\epsilon_{in}$ . . . . .	53
4.4.4	Macroscopic screening . . . . .	54
4.4.5	Macroscopic screening in reciprocal space and its restrictions	56
<b>5</b>	<b>Results and discussion</b>	<b>61</b>
5.1	Optical transitions in ZnS 2D nanoplatelets . . . . .	61
5.2	Solvent-dependent dielectric screening . . . . .	64
5.2.1	The role of the polarization terms . . . . .	64
5.2.2	Optical properties of CdSe and InP QDs in non-polar solvents	66
5.2.3	The role of the shape and crystal structure (CdSe QDs) . . .	70
5.2.4	The role of the passivant length (CdSe QDs) . . . . .	71
5.3	QD-QD coupled systems . . . . .	73
5.3.1	Coupled systems of Si QDs with different QD radius . . . . .	73
5.3.2	Formation of bonding–antibonding states in coupled systems of small Si, InP and CdSe QDs . . . . .	74
5.3.3	InP QDs in close-packed films: absorption peak shift . . . . .	76
5.4	Core-shell CdSe/CdS QDs with the sharp and alloyed interface . . .	78
5.4.1	The role of the CdS shell thickness . . . . .	78
5.4.2	The role of the CdSe core size . . . . .	81
<b>6</b>	<b>Summary and outlook</b>	<b>85</b>
	<b>Acknowledgements</b>	<b>103</b>
	<b>List of Chemicals</b>	<b>105</b>
	<b>Declaration on oath</b>	<b>107</b>

# Abstract

The quantum mechanical treatment of the electronic properties of colloidal semiconductor nanostructures, as used in experimental settings, remains a challenging task till today. Colloidal nanocrystals such as quantum dots or quantum wires with less than a thousand atoms are rarely synthesized and investigated experimentally, but that is the maximum size which can be treated by standard *ab initio* methods with a reasonable amount of computational resources, despite a great step forward in the parallel computing during the last decade. However, the theoretical understanding of the experimentally observed phenomena is of utmost importance. In this work a new comprehensive theoretical method is presented, which requires very moderate computational resources, but provides accurate *ab initio* results for the whole experimental range of sizes (from hundreds to more than 100 000 atoms) and dimensions (nanoplatelets, quantum wires, and quantum dots) of the colloidal nanostructures. The method allows a direct comparison between calculated and experimentally measured electronic and optical properties by including the effect of atomistic surface passivation and the influence of surrounding medium via a dielectric screening function.

In Chapter 1 a general overview of the physical properties of semiconductors is given. The role of the quantum confinement effect and its implications on possible applications by changing the scale from macroscopic to the nanometers is discussed. Diverse implementations of colloidal semiconductors in photovoltaics, in various types of electronic devices from lasers to personal computers, and even in biology and medicine determine the highest interest in studying their properties, both theoretically and experimentally.

In Chapter 2 existing theoretical *ab initio* methods, which provide atomistic description of the investigated molecular and crystal systems, are reviewed. Different approximations used to model the single atoms, bulk periodic crystals and finally experimental-sized nanostructures are gradually introduced. The atomic effective pseudopotential method is introduced in detail, and possible directions for further development of this computationally effective approach are indicated in Chapter 3.

In Chapter 4 recent progress in the theoretical method development is presented. First, a model, that simplifies the colloidal nanocrystal construction and structure relaxation, is introduced. The main part of this section is devoted to the further development of the atomic effective pseudopotential method, namely the non-spherical atomic effective potentials, and their implementation for the atomistic surface passivation. Additionally, the implementation of the empirical correction of the single-particle band gap is given in detail. Besides, the existing approaches to include the influence from a dielectric environment around nanocrystal are thoroughly reviewed and new approaches are presented.

In Chapter 5 the high transferability of the method presented in Chapter 3 and 4 is demonstrated and several examples of possible applications in close relation to the experimental data are shown, starting from ZnS nanoplatelets absorption spectra, optical properties of single and coupled CdSe (group II-VI), InP (group III-V) and Si (group IV) quantum dots up to the calculation of the electronic properties of giant core-shell CdSe/CdS quantum dots of more than 50 000 atoms with sharp and alloyed interface.

Finally, in Chapter 6 the results are summarized and further possible extensions and implementations of the developed computational approach are outlined.

# Zusammenfassung

Bis heute ist die quantenmechanische Berechnung der elektronischen Eigenschaften von in Experimenten genutzten kolloiden Halbleiter Nanostrukturen eine Herausforderung. Kolloide Nanokristalle wie Quantenpunkte oder Quantum Drähte mit weniger als eintausend Atomen werden selten synthetisiert und experimentell untersucht. Dies ist allerdings das Größenlimit von *ab initio* Methoden, welches mit vertretbarem Aufwand berechnet werden kann, trotz großer Fortschritte paralleler Computer in den vergangenen 10 Jahren. Allerdings ist das theoretische Verständnis der experimentell beobachteten Phänomene von entscheidender Bedeutung. In dieser Arbeit wird eine neue umfassende theoretische Methode vorgestellt, welche nur moderate Rechenleistung benötigt, aber zu *ab initio* Rechnungen vergleichbare Ergebnisse gibt. Damit können die gesamte experimentelle Größenbandbreite von Nanokristallen (von Hunderten bis mehr als 100 000 Atome) und Dimensionen (Nanoplättchen, Quanten Drähte und Quantenpunkte) berechnet werden, welches den direkten Vergleich von theoretisch und experimentell bestimmten elektronischen und optischen Eigenschaften ermöglicht. Der Einfluss der atomaren Oberflächenpassivierung und des umgebenden Mediums mittels einer dielektrischen Abschirmfunktion kann untersucht werden.

Im ersten Kapitel werden die allgemeinen physikalischen Eigenschaften von Halbleitern eingeführt. Der Einfluss des Quantum Confinement Effekts auf mögliche Anwendungen durch den Wechsel von makroskopischer zur Nanoskala wird diskutiert. Die diversen Anwendungsmöglichkeiten von kolloiden Halbleiter Nanopartikeln in Photovoltaik, elektronischen Bauteilen für Laser und Laptops sowie in der Biologie und Medizin unterstreichen die Wichtigkeit der Untersuchung ihrer Eigenschaften, sowohl theoretisch als auch experimentell.

Im zweiten Kapitel werden existierende *ab initio* Methoden diskutiert, welche atomare Auflösung der untersuchten molekularen und kristallinen Systeme geben. Verschiedene Näherungen um einzelne Atome, periodische Festkörper oder Nanostrukturen experimenteller Größe zu beschreiben werden erläutert. Die atomare effektive Pseudopotential Methode wird im Detail eingeführt und weitere Entwick-

lungsmöglichkeiten für zukünftige Anwendungen dieser günstigen rechengestützten Methode sind in Kapitel 3 beschrieben.

Im vierten Kapitel wird der aktuelle Fortschritt in der Methodenentwicklung präsentiert. Zuerst wird ein Model vorgestellt, welches die Konstruktion und Strukturoptimierung der Kolloiden Nanokristalle vereinfacht. Danach wird die Weiterentwicklung einer atomaren effektiven Pseudopotential Methode, basierend auf nicht sphärischen atomaren effektiven Potentialen und die Implementierung atomarer Oberflächenpassivierung vorgestellt. Zusätzlich wird auf die empirische Korrektur der Einteilchen Bandlücke eingegangen. Existierende Methoden um den Einfluss eines dielektrischen Mediums um einen Nanokristall zu modellieren werden vorgestellt und einige neue Ansätze präsentiert.

Im fünften Kapitel wird die Übertragbarkeit der in Kapitel 3 und 4 vorgestellten Methode an verschiedenen Beispielen gezeigt. So werden Adsorptionsspektren von ZnS Nanoplättchen sowie optische Eigenschaften von einzelnen und gekoppelten CdSe (Gruppe II-VI), InP (Gruppe III-V) und Si (Gruppe 4) Quantenpunkten vorgestellt. Abschließendes Beispiel ist die Berechnung der elektronischen Eigenschaften der großen Kern/Schale CdSe/CdS Quantenpunkte mit mehr als 50 000 Atomen und scharfer oder legierter Grenzfläche.

Abschließend werden die Ergebnisse in Kapitel 6 zusammengefasst und weitere mögliche Erweiterungen und Implementierungen für die entwickelte Rechenmethode diskutiert.

# List of publications

- H. Bui, A. Karpulevich and G. Bester “Excitonic fine structure of zincblende and wurtzite colloidal CdSe nanocrystals and comparison to effective mass results”, *Physical Review B*, 101(11), 115414 (2020).
- A. Karpulevich, H. Bui, Z. Wang, S. Hapke, C.P. Ramírez, H. Weller and G. Bester “Dielectric response function for colloidal semiconductor quantum dots”, *The Journal of Chemical Physics*, 151(22), 224103 (2019).
- L. Dai, R. Lesyuk, A. Karpulevich, A. Torche, G. Bester and C. Klinké “From Wurtzite Nanoplatelets to Zinc Blende Nanorods: Simultaneous Control of Shape and Phase in Ultrathin ZnS Nanocrystals”, *The Journal of Physical Chemistry Letters*, 10 (24), 3828-3835 (2019).
- A. Karpulevich, H. Bui, D. Antonov, P. Han and G. Bester “Nonspherical atomic effective pseudopotentials for surface passivation”, *Physical Review B*, 94 (20), 205417 (2016).

Publications that are not part of the dissertation:

- A.A. Karpulevich, E.G. Maksimov, N.N. Sluchanko, A.N. Vasiliev and V.Z. Paschenko “Highly efficient energy transfer from quantum dot to allophycocyanin in hybrid structures”, *Journal of Photochemistry and Photobiology B: Biology*, 160, 96-101 (2016).



# List of abbreviations

AEP	Atomic effective pseudopotential
BA	Bonding-antibonding (state or splitting)
CB	Conduction band
CBM	Conduction band minimum
CF	Crystal field
CI	Configuration Interaction
DB	Dark-bright (splitting)
DFT	Density-functional theory
e	Electron
FS	Fine structure
h	Hole
HOMO	Highest occupied molecular orbital
LDA	Local density approximation
LUMO	Lowest unoccupied molecular orbital
NC	Nanocrystal
NPL	Nanoplatelet
QD	Quantum dot
QP	Quasiparticle
QW	Quantum wire
SC	Single configuration
SO	Spin-orbit
SP	Single-particle
SEP	Semi-empirical pseudopotential
SEPM	Semi-empirical pseudopotential methods
VB	Valence band
VBM	Valence band maximum
VFF	Valence force field
WZ	Wurtzite
ZB	Zincblende

**Materials:**

CdSe	Cadmium selenide
CdS	Cadmium sulfide
InP	Indium phosphide
InAs	Indium arsenide
Si	Silicon
ZnS	Zinc selenide

# Chapter 1

## Introduction

### 1.1 Crystal lattice in solid state physics

The atoms in a crystal can be mathematically represented as points in a three-dimensional real-space lattice. If these lattice points are arranged in a periodic fashion, this reflects the periodic properties of the atoms in the crystal. The lattice, which specifies a periodic array with repeated units, called a Bravais lattice [1], and which meets the condition:

$$\mathbf{R} = n_1\mathbf{a}_1 + n_2\mathbf{a}_2 + n_3\mathbf{a}_3 \quad , \quad (1.1)$$

where  $\mathbf{a}_{1,2,3}$  are primitive vectors, and the indexes  $n_{1,2,3}$  are integers which define the crystallographic planes. For example, the [111] crystallographic direction in a cube corresponds to the  $[n_1n_2n_3]$  direction from the point of origin. Vector  $\mathbf{R}$  is a three-dimensional translation vector, i.e. the Bravais lattice is exactly same for any choice of  $\mathbf{R}$ , as well as any quantity of the crystal ( $f(\mathbf{r} + \mathbf{R}) = f(\mathbf{r})$ ).

A volume of space that, when translated through all the vectors in a Bravais lattice, just fills all of the space without overlaps or gaps is called a primitive cell, and the number of the Bravais lattice points within the primitive cell forms its basis. The Wigner-Seitz cell is one of the most common types of primitive cell and is defined as a region of space that is closer to particular lattice point than to any other lattice point. The primitive cell which is chosen that way, that it contains exactly one lattice point, is called a Wigner-Seitz cell.

If we consider a Bravais lattice in real space and a plane wave  $f = e^{i\mathbf{k}\mathbf{r}}$  for a general reciprocal vector  $\mathbf{k}$ , the set of vectors  $\mathbf{G}$  which fulfil the periodic condition  $e^{i\mathbf{G}\cdot(\mathbf{r}+\mathbf{R})} = e^{i\mathbf{G}\cdot\mathbf{r}}$  will form the reciprocal representation of a given Bravais lattice. The primitive vectors constructing the reciprocal lattice can be generated from the

real-space primitive vectors in the following way:

$$\mathbf{b}_1 = 2\pi \frac{\mathbf{a}_2 \times \mathbf{a}_3}{\mathbf{a}_1 \cdot (\mathbf{a}_2 \times \mathbf{a}_3)} ; \mathbf{b}_2 = 2\pi \frac{\mathbf{a}_3 \times \mathbf{a}_1}{\mathbf{a}_1 \cdot (\mathbf{a}_2 \times \mathbf{a}_3)} ; \mathbf{b}_3 = 2\pi \frac{\mathbf{a}_1 \times \mathbf{a}_2}{\mathbf{a}_1 \cdot (\mathbf{a}_2 \times \mathbf{a}_3)} . \quad (1.2)$$

The translation vector  $\mathbf{G}$  in reciprocal space can be written as (see Ref.[2] for the details):

$$\mathbf{G} = k_1 \mathbf{b}_1 + k_2 \mathbf{b}_2 + k_3 \mathbf{b}_3 , \quad (1.3)$$

where the indexes  $k_{1,2,3}$  are called Miller indexes, and they describe the crystallographic planes orthogonal to the reciprocal lattice vector, for example, the **(111)** Miller plane in cube corresponds to the plane orthogonal to  $(k_1 k_2 k_3)$  direction from the origin point. Round brackets are used to avoid confusion with crystallographic directions in real space. The primitive cell, that corresponds to a Wigner-Seitz cell in reciprocal space, is called Brillouin zone.

Most experimental methods for determining the atomic structure of crystals are based on the idea of light scattering, in particular, the X-ray diffraction [3], where the reciprocal lattice formalism is extremely useful. The periodic crystal structure determines the range of energies of an electron that the bulk crystal may have within it and thereby the corresponding electronic band structure. Band theory [4] has been successfully used to explain different physical properties of solids, such as electrical resistance and optical absorption, and forms the foundation of the understanding of transistors, solar cells, and other solid-state devices.

## 1.2 Semiconductor materials

In the ground state of a system the total energy is minimal and the electrons are located at the lowest possible energy levels. The property which distinguishes semiconductors from other bulk materials is the existence of an energy gap (or band gap) between the highest occupied energy band (valence band maximum, VBM) and the lowest unoccupied energy band (conduction band minimum, CBM) in their electronic band structure [5, 6]. The resistance of semiconductor materials falls as the temperature rises and therefore their electrical conductivity can change with varying conditions.

Semiconductors are broadly used in everyday life. Silicon (Si) holds the first place in semiconductor devices, in particular, the metal-oxide silicon field-effect transistors (MOSFETs) were the key component of the digital revolution in 21st century [7, 8]. Indium Phosphide (InP) and Indium Arsenide (InAs) with superior electron mobility are widely implemented in high-power and high-frequency elec-

tronics [9]. Cadmium Selenide (CdSe) and Cadmium Sulfide (CdS) materials are implemented in photoresistors and instruments utilizing infrared light [10]. Zinc Sulfide (ZnS) is a large-gap semiconductor which is widely used as an efficient photocatalyst[11].

The majority of bulk semiconductor materials are highly-periodic crystal structures. In quantum mechanics, periodic boundary conditions are usually used to treat the large bulk crystals, where the detailed configuration of the surface does not affect the electronic properties, i.e. the large periodic crystal is approximated by infinite repetition of the corresponding primitive cell. The materials, considered in this work, either possess diamond or zincblende (ZB) crystal structure, with the face-centered cubic Bravais lattice and two-atom basis in the primitive cell (materials such as Si, InP, InAs), or wurtzite (WZ) crystal structure, in a hexagonal close-packed form with four-atom basis in the primitive cell (materials such as ZnS) [2]. Some of the materials, for example, CdSe or CdS, may form in the ZB or WZ crystal structure depending on the synthesis conditions [12, 13, 14]. The Si bulk crystal unit (unit cell), primitive and the corresponding Brillouin zone together with the band structure in reciprocal space are shown in Fig. 1.1.

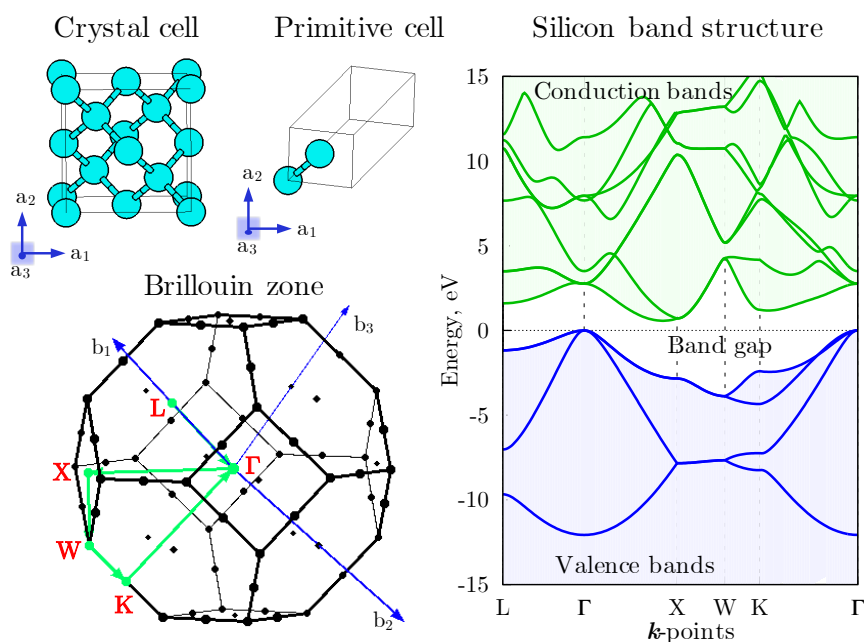


Figure 1.1: Left panel: Si bulk (ZB structure) crystal unit cell and the primitive cell in real space together with the corresponding Brillouin zone in reciprocal space. Right panel: the electronic band structure with valence (blue) and conduction (green) bands plotted through the high-symmetry points of the Brillouin zone (green arrows).

Under the influence of electrical or optical excitation, an electron might be pro-

moted from the valence to the conduction band, leaving behind in the valence band a local positive charge called a hole. Electron and hole together form a neutral quasiparticle called an exciton, where the distance between electron and hole defined as an exciton Bohr radius. The electron and hole of the exciton might recombine back to the ground state via one of the multiple relaxation channels, which can be subdivided in radiative, i.e. accompanied by light (photon) emission, and non-radiative. If the decay of the exciton is accompanied with the light emission, this process is called fluorescence [15].

### 1.3 Semiconductor nanostructures and their applications

Semiconductor nanostructures with at least one dimension below their exciton Bohr radius evoke high scientific interest due to their tunable optical and chemical properties caused by confinement effect and high surface-to-volume ratio [5, 16]. The confinement effect originates from an increase in kinetic energy of electron and hole, which outweighs the shrinkage of potential energy, and leads to discrete electronic states formation [17, 18].

Ultra-thin 2D nanocrystals (NCs) like nanoplatelets (NPLs) possess uniform thickness after synthesis and have broad potential applications such as laser diodes, high electron mobility transistors, and infrared detectors [19, 20, 21]. Considerable progress in the synthesis techniques colloidal quantum wires (QWs) and quantum dots (QDs), especially for CdSe and CdS materials, has allowed obtaining the stable fractions of colloidal nanostructures with narrow particle size distributions and high intensity of the fluorescence in visible and infrared range [22, 23, 24]. This leads to many opportunities for new applications including lasers [25], fluorescent labeling of biological molecules and cells [26, 27, 28, 29], light-emitting diodes [30], in particular display components [31] and smart windows [32], as well as solar cells [33]. Another very promising research direction is studying the electronic transport in the close-packed QD arrays, which already have shown outstanding efficiency as multiple-exciton generators and enable new fabrication methods for low-cost and flexible thermometric devices and power inverters, superior to natural materials systems [34, 35, 36].

Many-compound QDs such as core-shell and core-shell-shell NCs demonstrate very high and stable fluorescence due to the elimination of the surface defects [37, 38] and increased photoconductivity. The alloyed interface in core-shell QDs suppresses blinking and Auger recombination [39, 40], which promises wide perspectives for potential practical usage of this new generation of colloidal nanostructures.

The relative alignment of the electron ( $e$ ) and hole ( $h$ ) in core-shell QDs, which depends on the relative core and shell material offsets and confinement, subdivides these nanostructures into several types (see Fig. 1.2).

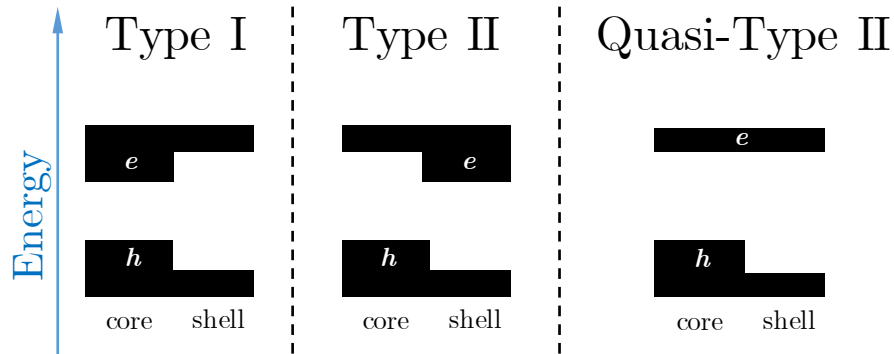


Figure 1.2: Schematic representation of the different types of core-shell QDs, depending on the relative band offsets of core and shell material.

For type-I core-shell QDs, electron and hole are localized either both in the core or both in the shell, whereas type-II QDs demonstrate spatial isolation of the electron and hole. The intermediate case forms a class of quasi-type II QDs [41]. Both type-I and type-II core-shell QDs have very promising perspectives of the next-generation bio-compatible fluorescent markers [42, 43], besides, type-II core-shell QDs, due to spatial charge separation, have engaging perspectives in photovoltaics for the next generation of solar cells [44].



## Chapter 2

# Computational methods

The Schrödinger equation is a cornerstone of quantum mechanics. Exact solution of the Schrödinger equation for an atomic or molecular system is in fact full and complete description of this system, which enables the prediction of its physicochemical properties. However, the exact solutions are not possible even for the small systems of interest due to the complexity of the electrons behavior in condensed matter. Therefore, any algorithm attempting to calculate the physical properties of the atomic system relies on approximations. In this thesis, the basic concepts of ab initio calculations will be introduced and existing theoretical approaches for modeling the ground and excited states of the systems consisting of more than 1000 atoms will be presented.

### 2.1 Many-body Hamiltonian

The electronic properties of an atomic or molecular structure can, in general, be explained in terms of quantum mechanics. Prediction of the electronic and geometric structure of the system requires the calculation of its total energy and subsequent minimization of this energy concerning electronic and nuclear coordinates [45]. The stationary, or time-independent, Schrödinger equation for a system of  $M$  nuclei and  $N$  electrons [46, 47] can be written as:

$\hat{H}\Psi = E\Psi$ , where

$$\hat{H} = \left[ -\sum_I^M \frac{\hbar^2}{2M_I} \nabla_I^2 - \sum_i^N \frac{\hbar^2}{2m_e} \nabla_i^2 \right] + \frac{e^2}{4\pi\epsilon_0} \left[ \frac{1}{2} \sum_I^M \sum_{J \neq I}^M \frac{Z_I Z_J}{|\mathbf{R}_I - \mathbf{R}_J|} + \frac{1}{2} \sum_i^N \sum_{j \neq i}^N \frac{1}{|\mathbf{r}_i - \mathbf{r}_j|} - \sum_i^N \sum_I^M \frac{Z_I}{|\mathbf{r}_i - \mathbf{R}_I|} \right]. \quad (2.1)$$

The full many-body Hamiltonian from Eq. (2.1) includes kinetic energies of all nuclei and electrons of the system (first two terms, respectively) as well as the potential energy, resulting from nuclei-nuclei, electron-electron and electron-nuclei Coulomb interaction terms (last three terms, respectively). The indices  $i$  and  $j$  run over the electronic degrees of freedom and  $I$  and  $J$  run over nuclei degrees of freedom.

For simplicity, atomic units will be used, which means that the inversed Coulomb constant  $4\pi\epsilon_0$ , the reduced Plank constant  $\hbar$  as well as the electron mass  $m_e$  and the elementary charge  $e$  will be equalized to 1 and no longer written explicitly.

The exact solution of the many-body Schrödinger equation even for the small molecular systems is a literally impossible task. One of the key approximations which are widely used nowadays is the Born-Oppenheimer, or frozen-core, approximation [48, 49]. The idea is that the electrons in the system move much faster than the atomic nuclei because the atomic cores are several orders of magnitude heavier than electrons. Therefore, it can be assumed that atomic cores are fixed, nuclei kinetic energy is equal to 0 and the nuclei-nuclei Coulomb interaction term turns into a constant additional energy  $E(\mathbf{R}_I)$ . Thus, the many-body problem transforms into a many-electron problem, and the electronic Hamiltonian can be written as:

$$\hat{H}_e = -\frac{1}{2} \sum_i^N \nabla_i^2 + \frac{1}{2} \sum_i^N \sum_{j \neq i}^N \frac{1}{|\mathbf{r}_i - \mathbf{r}_j|} - \sum_i^N \sum_I^M \frac{Z_I}{|\mathbf{r}_i - \mathbf{R}_I|} + E(\mathbf{R}_I) \quad . \quad (2.2)$$

The wave functions  $\Psi$  of the many-electron systems must be antisymmetric, because electrons are fermions, and the exchange of any two electrons should fulfill the Pauli principle [50]. The antisymmetry leads to the spatial separation between electrons with the same spin, therefore the electron-electron Coulomb interaction is reduced by a Coulomb-like term called the exchange energy [45]. The exchange energy might be directly included in the electronic Hamiltonian, as in the Hartree-

Fock approximation [51, 52] which will be addressed in more detail in Section 2.4. In fact, electrons with opposite spins are also spatially separated, which leads to a further reduction of the electron-electron Coulomb interaction, but at the same time increases the electron kinetic energy. These effects can be included in the correlation energy term [53].

It is possible to solve the many-body electron problem for simple systems like electron gas using quantum Monte Carlo simulations [54]. However, this is not applicable for complex structures like molecules or crystals.

## 2.2 Density functional theory

An alternative solution to the many-electron Schrödinger equation is to replace the many-electron wave function  $\Psi$  in the model system with the electron density. According to the Hohenberg-Kohn theorems [55], the ground state density  $n(\mathbf{r})$  is uniquely defined by the external potential, coming from the electron-nuclei interactions and external fields, and a universal functional for the energy  $E$  can be defined in terms of the density. The exact ground state is the global minimum value of this functional. These theorems underlie the density functional theory (DFT), which is widely used to calculate the electronic properties of metals and semiconductors.

The second major development step for DFT theory was performed by Kohn and Sham [56], who have shown that it is formally possible to replace the many-electron wave function  $\Psi$  by a set of the single-particle wave functions, or orbitals,  $\psi_i$ . The electron density in this case can be written as:

$$n(\mathbf{r}) = \sum_i f_i |\psi_i(\mathbf{r})|^2 \quad , \quad (2.3)$$

where  $f_i$  is an occupation number.

Within these approximations, the Kohn-Sham total energy functional in Eq. (2.2), in accordance with what was mentioned above, can be represented in the following way [57]:

$$\begin{aligned} E &= E^{\text{kinetic}} + E^{\text{ext}} + E^{\text{H}} + E^{\text{XC}} + E^{\text{nuclei}} = \\ &= -\frac{1}{2} \sum_i^{N_{\text{occ}}} \int \psi_i^* \nabla^2 \psi_i d\mathbf{r} + \int n(\mathbf{r}) \left( -\sum_I \frac{Z_I}{|\mathbf{r} - \mathbf{R}_I|} \right) d\mathbf{r} + \\ &+ \frac{1}{2} \iint \frac{n(\mathbf{r})n(\mathbf{r}')}{|\mathbf{r} - \mathbf{r}'|} d\mathbf{r}d\mathbf{r}' + \int n(\mathbf{r}) \varepsilon_{\text{XC}}[n(\mathbf{r})] d\mathbf{r} + E(\mathbf{R}_I) . \end{aligned} \quad (2.4)$$

Here the  $E^{\text{kinetic}}$  term includes the kinetic energy of the electrons,  $E^{\text{ext}}$  comprise the electron-nuclei (external potential) interactions, Hartree functional  $E^{\text{H}}$  contains Coulomb interactions between electrons,  $E^{\text{nuclei}}$  the interactions between nuclei, which is constant due to the frozen-core approximation, and the  $E^{\text{XC}}$  term is the exchange-correlation functional (see Section 2.2.1 for details). Unfortunately, except for very simple systems, it is not possible to define exact exchange-correlation functional. Possible approximations will be considered in the next subsection.

The Kohn-Sham orbitals are initially completely unspecified, but, in agreement with the Hohenberg-Kohn theorems, the minimal total energy of the system corresponds to a certain type of the single-particle orbitals. And only the minimum value of the Kohn-Sham functional has a physical meaning: ground state energy of the system with  $N$  electrons and the defined nuclei positions.

Utilizing the Hohenberg-Kohn theorems, the ground state energy functional from Eq. (2.4) can be minimized with respect to the orbitals  $\psi_i^*(\mathbf{r})$  by taking the derivatives from its components according to the chain rule (as long as  $E^{\text{nuclei}}$  is a constant, the derivative is equal to 0) :

$$\frac{\delta E^{\text{kinetic}}}{\delta \psi_i^*(\mathbf{r})} + \left[ \frac{\delta E^{\text{ext}}}{\delta n(\mathbf{r})} + \frac{\delta E^{\text{H}}}{\delta n(\mathbf{r})} + \frac{\delta E^{\text{XC}}}{\delta n(\mathbf{r})} \right] \frac{\delta n(\mathbf{r})}{\delta \psi_i^*(\mathbf{r})} = \varepsilon_i \psi_i(\mathbf{r}) \quad . \quad (2.5)$$

It is assumed that the single-particle wave functions are in the field of the effective Kohn-Sham potential  $V_{\text{eff}}$  that describes all the interactions of a single electron with the environment (other electrons and nuclei) [56]. With this approximation, the many-electron problem with the system of the single-particle Schrödinger equations is represented as follows:

$$\left( -\frac{1}{2}\nabla^2 + V^{\text{eff}}(\mathbf{r}) \right) \psi_i(\mathbf{r}) = \varepsilon_i \psi_i(\mathbf{r}) \quad , \quad \text{where} \\ V^{\text{eff}}(\mathbf{r}) = V^{\text{ext}}(\mathbf{r}) + V^{\text{Hartree}}[n(\mathbf{r})] + V^{\text{xc}}[n(\mathbf{r})] \quad . \quad (2.6)$$

From Eq. (2.5) and Eq. (2.6) it can be seen, that the effective Kohn-Sham potential  $V_{\text{eff}}$  consists of terms, which depend on the electron density and, therefore, indirectly depend on the single-particle wave functions. In other words, any change of the Kohn-Sham orbitals will affect also  $V_{\text{eff}}$ , and vice versa. It means that the Kohn-Sham system of equations must be solved self-consistently [57].

The Kohn-Sham wave functions satisfy the orthonormal condition [5], which can be expressed in form of a Kronecker delta:

$$\int \psi_i^*(\mathbf{r})\psi_j(\mathbf{r})d\mathbf{r} = \langle \psi_i | \psi_j \rangle = \delta_{i,j} ; \delta_{i,j} = \begin{cases} 0 & \text{if } i \neq j \\ 1 & \text{if } i = j \end{cases} . \quad (2.7)$$

The self-consistent solution of Eq. (2.6), therefore, form a complete and orthonormal set of Kohn-Sham wave functions, which will reproduce the ground state density  $n^{\text{scf}}(\mathbf{r})$  (Eq. (2.3)).

### 2.2.1 Exchange-correlation functionals

As it was already mentioned, the calculation of the exchange-correlation energy functional in the model system is a non-trivial task. One of the most precise options is the *GW* approximation, in which the exchange-correlation functional is approximated by the single-particle Green's function  $G$  and the screened Coulomb interaction  $W$ , which are not expanded beyond the first term *iGW* [58, 59]. This is a precise method that allows performing high-quality calculations, but only for structures no larger than several dozen atoms due to high computational demand. It means, the method can only be used for small molecules or bulk crystal structures.

Maybe one of the oldest but still widely used for the crystal nanostructures exchange-correlation functional is based on the local density approximation (LDA) [60]. LDA assumes that the exchange-correlation energy  $\varepsilon_{XC}(\mathbf{r})$  of an electronic system per electron at a coordinate  $\mathbf{r}$  in the non-homogeneous system is indeed locally homogeneous. The derivative from  $E^{\text{XC}}$  can be written as:

$$\frac{\delta E^{\text{XC}}}{\delta n(\mathbf{r})} = V^{\text{xc}}[n(\mathbf{r})] = \int \varepsilon_{XC}^{\text{hom}}[n(\mathbf{r})] + n(\mathbf{r}) \frac{\delta \varepsilon_{XC}^{\text{hom}}[n(\mathbf{r})]}{\delta n(\mathbf{r})} d\mathbf{r} . \quad (2.8)$$

LDA-based  $V^{\text{XC}}$  give reasonable computational results for the non-spin-polarized non-magnetic materials, which match the properties of the goal object - semiconductor nanocrystals - since no external field is considered. The accurate prediction happens partly due to cancellations of the errors, produced by this approximation (overestimation of the exchange and underestimation of the correlation effect [45]). The LDA approximation generally underestimates the band gap in semiconductor materials due to the charge delocalization [61], which, however, can be corrected empirically (see Section 4.3 for details).

There are also more advanced (but also less universal and/or computationally more demanding) methods, like the Generalized Gradient Approximation (GGA), where the gradient of the density is also included in the  $E^{\text{XC}}$  functional [62], hybrid functionals [63, 64] and many others which are beyond the scope of this project and therefore will be not described in detail.

### 2.2.2 Plane wave basis and pseudopotentials

For practical purposes it is necessary to expand the Kohn-Sham orbitals using a set of basis functions. Kohn-Sham wave function can be written as a linear expansion of the arbitrary basis set  $\{\varphi_\alpha(\mathbf{r})\}$ :

$$\psi_i(\mathbf{r}) = \sum_{\alpha} c_{\alpha i} \varphi_{\alpha}(\mathbf{r}) \quad . \quad (2.9)$$

Here  $c_{\alpha i}$  are linear expansion coefficients. There are many different approaches on how to actually represent Kohn-Sham orbitals within DFT framework, for example, Gaussian or Slater orbitals [65] or a linear combination of atomic orbitals [5]. The plane wave basis set is the most commonly used for the solid crystals and will be reviewed in detail.

According to Bloch's theorem [2, 66], each wave function in a periodic solid crystal can be written as a product of a lattice-periodic component  $u(\mathbf{k}, \mathbf{r} + \mathbf{R}) = u(\mathbf{k}, \mathbf{r})$  and a plane wave component  $e^{i\mathbf{k}\mathbf{r}}$ :

$$\varphi_i(\mathbf{k}, \mathbf{r}) = e^{i\mathbf{k}\mathbf{r}} \cdot u(\mathbf{k}, \mathbf{r}) \quad . \quad (2.10)$$

The function  $u(\mathbf{k}, \mathbf{r})$  of a periodic crystal can be also expanded using plane wave basis set with reciprocal lattice vector  $\mathbf{G}$ :

$$u(\mathbf{k}, \mathbf{r}) = \sum_{\mathbf{G}} c_{\mathbf{k}, \mathbf{G}} e^{i\mathbf{G}\mathbf{r}} \quad , \quad (2.11)$$

and the Kohn-Sham wave functions from Eq. (2.9) can be represented in reciprocal space as:

$$\psi_i(\mathbf{k}, \mathbf{r}) = \sum_{\mathbf{G}} c_{i, (\mathbf{k} + \mathbf{G})} e^{i(\mathbf{k} + \mathbf{G})\mathbf{r}} \quad . \quad (2.12)$$

It is very convenient and computationally efficient to solve Kohn-Sham equations (Eq. (2.6)) in reciprocal space. The plane waves approach is also suitable for non-periodic systems such as nanocrystals, which can be modeled by supercells, crystal units larger than a bulk unit cell, which must be included in the calculation explicitly due to violated periodic boundary conditions [67].

One of the main disadvantages of the plane wave basis set is that in reality Kohn-Sham wave functions strongly oscillate near atomic nuclei, and an enormous number of plane waves is needed to describe these oscillations. Additionally, it is impossible to perform all-electron plane wave calculations for systems of practical

interest. Fortunately, these restrictions can be overcome with the pseudopotential approach.

The pseudopotential approach replaces the real external potential  $V^{\text{ext}}$  (responsible for the electron-nucleus interactions) under the certain radius in proximity of the atom core  $r_{\text{cut}}$  with the  $V^{\text{PSP}}$ , which includes both atomic nucleus and core electrons. This approximation results in a smoothed wave functions  $\psi_i$  inside  $r_{\text{cut}}$  which can be described with a moderate-sized plane wave basis set [68]. Please note, that outside the  $r_{\text{cut}}$  both pseudopotential and corresponding wave functions coincide with the exact potential for a specific atomic configuration (see Fig. 2.1). It is also important, that orthonormal properties of the wave functions (Eq. (2.7)) remain conserved.

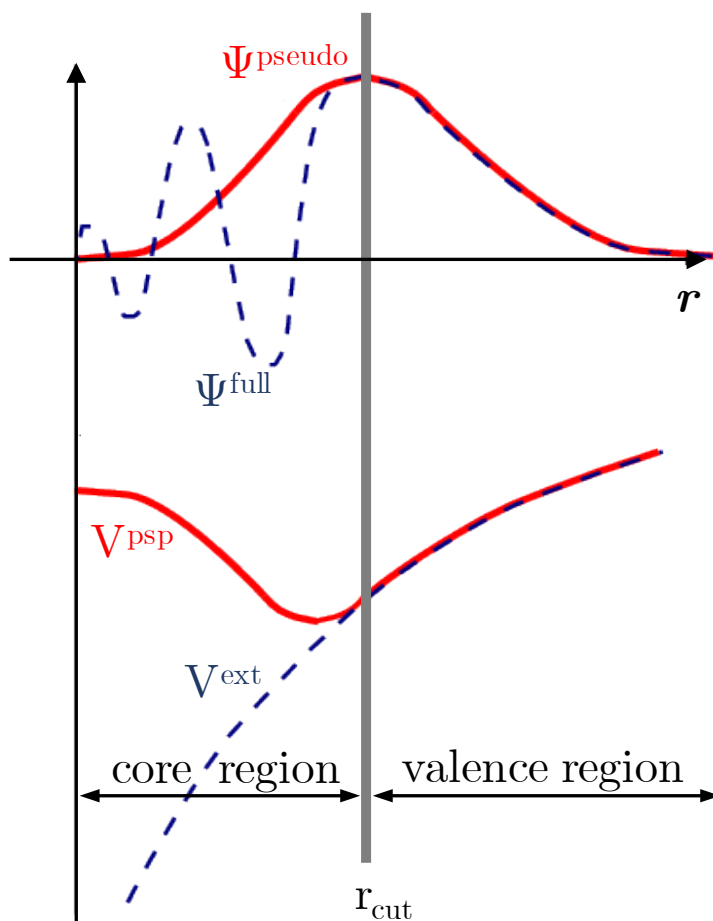


Figure 2.1: Schematic representation of the pseudopotential  $V^{\text{PSP}}$  and the pseudo-wave function in real space (red), compared to the exact external potential  $V^{\text{ext}}$  and corresponding wave function (blue). Reproduced in agreement with Ref.[45].

Additionally, a plane wave cutoff  $|\mathbf{k} + \mathbf{G}| < \mathbf{G}_{\text{cut}}$  is introduced to reduce the basis set, namely only the reciprocal lattice vectors whose kinetic energy lower

than a predefined kinetic energy maximum  $-\frac{1}{2}|\mathbf{G}_{\text{cut}}|^2 < E_{\text{cut}}^{\text{kinetic}}$  are used in the basis set, as long as high frequency (high energy) plane waves will only give very minor improvements to the total wave function representation. Pseudopotential approximation gives results very close to the fully self-consistent calculations [49].

The pseudopotentials for different atom types have a high degree of transferability in different atomic configurations and require moderate computational costs which allow using this approach for the crystal structures consisting of up to thousand atoms [69].

## 2.3 Atomic effective pseudopotentials

Experimental-sized colloidal nanostructures usually contain from hundreds to hundred-thousands of atoms, most of this size range exceeding the standard DFT-LDA computational limit. To address the nanostructures consisting of many thousands of atoms, the atomic effective pseudopotentials (AEPs) were developed [70]. AEPs can be considered as a further step into the evolution of empirical and semi-empirical pseudopotentials (SEP), which allows bypassing the bottle-neck of classical DFT methods – the self-consistent loop.

The Kohn-Sham equations (Eq. (2.6)) are normally solved self-consistently, and the electron density of the system is updated until convergence to the ground state density  $n^{\text{scf}}$ . Here the norm-conserving pseudopotential  $V^{\text{psp}}$  in the Kleinman and Bylander separable form is considered, which includes a position-dependent local part and an angular momentum  $l$ -dependent non-local part. The latter also includes spin-orbit (SO) coupling [71, 72]. The effective potential  $V^{\text{eff}}$  from Eq. (2.6) can be expressed as:

$$\widehat{V}^{\text{eff}} = V^{\text{psp,loc}} + V^{\text{Hartree}}[n] + V^{\text{xc}}[n] + \sum_{lm} |\chi_{lm}^{KB}\rangle E_l^{KB} \langle \chi_{lm}^{KB}| \quad , \quad (2.13)$$

where the last term in Eq. (2.13) is the non-local part of the pseudopotential,  $E_l^{KB}$  are the Kleinman-Bylander eigenvalue and  $\chi_{lm}^{KB}$  the normalized Kleinman-Bylander projectors. The real-space implementation of the non-local part of the pseudopotential including (optionally) spin-orbit interactions is possible without self-consistent loop using the basis of spin-angular functions (see Ref.[73] for details).

The starting point for the AEPs derivation is the local part of the self-consistent

effective potential  $V^{\text{eff}}(\mathbf{r})$ :

$$V^{\text{loc}}(\mathbf{r}) = V^{\text{psp,loc}}(\mathbf{r}) + V^{\text{Hartree}}[n^{\text{scf}}] + V^{\text{xc}}[n^{\text{scf}}] \quad .$$

In this equation  $V^{\text{psp,loc}}$  are the norm-conserving pseudopotentials constructed using the approach of Troullier and Martins [74].

Since the periodic boundary conditions are used, the potential  $V^{\text{loc}}(\mathbf{r})$  is a periodic function and can be expanded in a Fourier series,

$$V^{\text{loc}}(\mathbf{r}) = \sum_{|\mathbf{G}| \leq \mathbf{G}_{\text{cut}}} V^{\text{loc}}(\mathbf{G}) e^{i\mathbf{G}\mathbf{r}} \quad ,$$

leading to the reciprocal-space potential,

$$V^{\text{loc}}(\mathbf{G}) = \frac{1}{\Omega_c} \int_{\Omega_c} V^{\text{loc}}(\mathbf{r}) e^{-i\mathbf{G}\mathbf{r}} d^3\mathbf{r} \quad , \quad (2.14)$$

where  $\Omega_c$  is the volume of the simulation supercell.

Let's consider an inversely symmetric real-space potential,  $V(\mathbf{r}) = V(-\mathbf{r})$ . The reciprocal-space potential obeys the symmetry  $V^{\text{loc}}(\mathbf{G}) = V^{\text{loc}*}(-\mathbf{G})$ , and the special case of a spherically symmetric real space potential  $V(\mathbf{r}) = V(|\mathbf{r}|)$  leads to a vanishing imaginary part of the reciprocal-space potential as well as a spherical symmetry of the latter one,  $V(\mathbf{G}) = V(|\mathbf{G}|)$ . Respectively, any deviation from the inversion symmetry of the real-space potential would lead to a non-zero imaginary part in the reciprocal-space potential.

In the AEP method [70], the total potential is defined as a sum of atom centered pseudopotentials:

$$V^{\text{loc}}(\mathbf{r}) = \sum_{\alpha}^{N_{\text{species}}} \sum_n^{N_{\alpha}} v_{\alpha}(\mathbf{r} - \boldsymbol{\tau}_{\alpha n}) \quad , \quad (2.15)$$

for the system with  $N_{\alpha}$  atoms of type  $\alpha$ . Each atom is centered at the position  $\boldsymbol{\tau}_{\alpha n}$ . The total reciprocal-space potential is defined as:

$$\begin{aligned} V^{\text{loc}}(\mathbf{G}) &= \sum_{\alpha}^{N_{\text{species}}} \sum_n^{N_{\alpha}} e^{-i\mathbf{G}\cdot\boldsymbol{\tau}_{\alpha n}} \tilde{v}_{\alpha}(\mathbf{G}) \quad \text{with} \quad (2.16) \\ \tilde{v}_{\alpha}(\mathbf{G}) &= \frac{1}{\Omega_c} \int_{\infty} v_{\alpha}(\mathbf{r}) e^{-i\mathbf{G}\mathbf{r}} d^3\mathbf{r} \quad , \end{aligned}$$

where  $v_{\alpha}(\mathbf{G})$  without volume normalisation  $\Omega_c$  can be written as:

$$v_{\alpha}(\mathbf{G}) = \int_{\infty} v_{\alpha}(\mathbf{r}) e^{-i\mathbf{G}\mathbf{r}} d^3\mathbf{r} = \Omega_c \tilde{v}_{\alpha}(\mathbf{G}) \quad .$$

With this definition, Eq.(2.16) becomes:

$$V^{\text{loc}}(\mathbf{G}) = \frac{1}{\Omega_c} \sum_{\alpha}^{N_{\text{species}}} \sum_n^{N_{\alpha}} e^{-i\mathbf{G}\cdot\boldsymbol{\tau}_{\alpha n}} v_{\alpha}(\mathbf{G}) \quad . \quad (2.17)$$

Here  $v_{\alpha}(\mathbf{G})$  are the AEPs for the different atomic types. The AEPs have been defined as spherically symmetric in real space which translates into a reciprocal-space potential with real part only,  $v_{\alpha}(\mathbf{G}) = v_{\alpha}(|\mathbf{G}|)$ . It is needed in order to make the AEPs transferable for different crystal structures. The spherical approximation applied to bulk materials using AEPs [70, 73], or traditional empirical pseudopotentials [75, 76, 77, 78, 79], or semi-empirical pseudopotentials [80, 81] leads to insignificant errors in the eigenvalues resulting in a band gap deviations of around 60 meV [80], or, more specifically, of 87 meV for Si, 57 meV for InP and 8 meV for CdSe [70].

For the material interfaces, like in an alloy or core-shell nanostructures, weights are introduced to account for the difference in the chemical environment compared to the binary or pure bulk system. Including the weights  $\omega_{\alpha n} = n_{\alpha n}/4$  for the tetrahedrally coordinated materials (where  $n_{\alpha n}$  is the number of next neighbours of type  $\alpha$ ) changes Eq. (2.17) in the following way [73]:

$$V^{\text{loc}}(\mathbf{G}) = \frac{1}{\Omega_c} \sum_{\alpha}^{N_{\text{species}}} v_{\alpha}(\mathbf{G}) \sum_n^{N_{\alpha}} e^{-i\mathbf{G}\cdot\boldsymbol{\tau}_{\alpha n}} \omega_{\alpha n} \quad . \quad (2.18)$$

Back to the binary systems, one should note, that the AEPs cannot be taken directly from DFT calculation but can be determined via  $v_{\pm}$  potential, defined as:

$$v_{\pm} = v_a \pm v_c \quad , \quad (2.19)$$

which can be used for a binary system, in order to find the cation potential  $v_c$  and the anion potential  $v_a$  for the certain binary material in reciprocal space. The procedure can generally be done also for a mono materials by setting  $v_a = v_c$ . Two slabs along the  $[\mathbf{100}]$  direction with identical atomic coordinates and equal number of cations and anions, but interchanged cation and anion atomic positions are usually used as a binary system, from where the  $V_{(1)}^{\text{loc}}$  and  $V_{(2)}^{\text{loc}}$  can be extracted:

$$\begin{aligned}
 V_{(1)}^{\text{loc}}(\mathbf{r}) &= \sum_i^{N_a} v_a(\mathbf{r} - \boldsymbol{\tau}_i) + \sum_j^{N_c} v_c(\mathbf{r} - \boldsymbol{\tau}_j) \quad , \\
 V_{(2)}^{\text{loc}}(\mathbf{r}) &= \sum_i^{N_c} v_c(\mathbf{r} - \boldsymbol{\tau}_i) + \sum_j^{N_a} v_a(\mathbf{r} - \boldsymbol{\tau}_j) \quad .
 \end{aligned} \tag{2.20}$$

By adding and subtracting  $V_{(1)}^{\text{loc}}$  and  $V_{(2)}^{\text{loc}}$  from Eq. (2.20), the following expressions for  $v_+$  and  $v_-$  can be obtained:

$$\begin{aligned}
 V_{(1+2)}^{\text{loc}}(\mathbf{r}) &= \sum_n^{N_{\text{atoms}}} v_+(\mathbf{r} - \boldsymbol{\tau}_n) \quad , \\
 V_{(1-2)}^{\text{loc}}(\mathbf{r}) &= \sum_n^{N_{\text{atoms}}} (-1)^{n+1} v_-(\mathbf{r} - \boldsymbol{\tau}_n) \quad ,
 \end{aligned} \tag{2.21}$$

or, in reciprocal space:

$$\begin{aligned}
 V_{(1+2)}^{\text{loc}}(\mathbf{G}) &= \frac{1}{\Omega} \left[ \sum_n^{N_{\text{atoms}}} e^{i\mathbf{G}\cdot\boldsymbol{\tau}_n} \right] v_+(\mathbf{G}) \quad , \\
 V_{(1-2)}^{\text{loc}}(\mathbf{G}) &= \frac{1}{\Omega} \left[ \sum_n^{N_{\text{atoms}}} (-1)^{n+1} e^{i\mathbf{G}\cdot\boldsymbol{\tau}_n} \right] v_-(\mathbf{G}) \quad .
 \end{aligned} \tag{2.22}$$

Once again, the potentials  $v_+(\mathbf{G})$  and  $v_-(\mathbf{G})$  are in general complex quantities, but within the spherical approximation framework only the real part is taken into account.

The relative band offsets in AEPs between different materials are taken into account by linking them together using the DFT calculations of heterostructures. The procedure involves the interchange of the cation and anion positions within a 48-atom zincblende (ZB)  $[\mathbf{100}]$  hybrid slab, formed by two 24-atom halves presenting the different materials A and B (see Fig. 2.2).

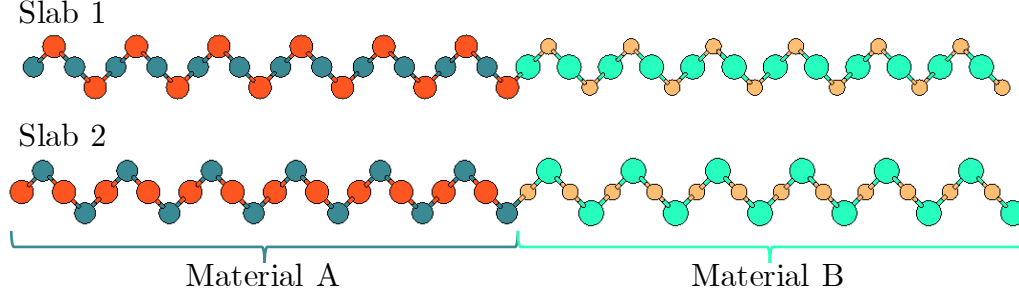


Figure 2.2: Schematic representation of the minimal periodic unit of the 48-atom zincblende (ZB) [100] hybrid slabs, formed by two different materials. Cation/anion positions in slab 1 and slab 2 are interchanged.

The resulting potentials  $V_{(1)}^{\text{loc}}$  and  $V_{(2)}^{\text{loc}}$  can be written similarly to Eq. (2.20):

$$\begin{aligned}
 V_{(1)}^{\text{loc}}(\mathbf{r}) &= \sum_i^{N_a^A} v_a^A(\mathbf{r} - \boldsymbol{\tau}_i) + \sum_j^{N_c^A} v_c^A(\mathbf{r} - \boldsymbol{\tau}_j) + \quad , \\
 &+ \sum_k^{N_a^B} v_a^B(\mathbf{r} - \boldsymbol{\tau}_k) + \sum_l^{N_c^B} v_c^B(\mathbf{r} - \boldsymbol{\tau}_l) \quad , \\
 V_{(2)}^{\text{loc}}(\mathbf{r}) &= \sum_i^{N_c^A} v_c^A(\mathbf{r} - \boldsymbol{\tau}_i) + \sum_j^{N_a^A} v_a^A(\mathbf{r} - \boldsymbol{\tau}_j) + \quad , \\
 &+ \sum_k^{N_c^B} v_c^B(\mathbf{r} - \boldsymbol{\tau}_k) + \sum_l^{N_a^B} v_a^B(\mathbf{r} - \boldsymbol{\tau}_l) \quad . \quad (2.23)
 \end{aligned}$$

If the AEPs of slab A are fixed to the potential  $V^{\text{loc}}$  derived from the DFT bulk calculation, then the  $v_{\pm}$  for slab B can be extracted and corrected, and this procedure should be repeated in chain manner for materials C, D, etc until all material offsets are defined. The linking order is defined by using hybrid structures with the lowest possible crystal lattice mismatch between two materials (see Ref.[70] for details).

To obtain a correct absolute shift of the band energies using AEPs, a series of calculations for each bulk material were performed, with the lattice constant varying by 0.2% in order to obtain the linear dependence of the band gap change versus lattice constant. The extracted deformation potentials were interpolated over different  $V(\mathbf{G} = 0)$ , and the final  $V^{\text{AEP}}(\mathbf{G} = 0)$  value was fixed based on the literature values of the deformation potential [82].

It has been shown, that crystal structures containing up to 100 000 atoms can be treated at an atomistic *ab initio* level comparable to DFT-LDA using the AEP

formalism [73]. Before the development of the *ab initio* methods, parametric approaches based on the effective mass approximation [83] were used to provide theoretical predictions in comparison with existing experiments. However, while it is always possible to fit an effective mass model to the experimental results with only a few parameters, the underlying physics remains not clear and the prediction capacities of these models for non-optimized properties are very low [84].

## 2.4 Configuration interaction theory

The single-particle wavefunctions obtained from the DFT-LDA or AEP method can be used to construct the ground state Slater determinant  $\Phi_0$  [85, 72]:

$$\Phi_0(\mathbf{r}_1, \sigma_1; \dots; \mathbf{r}_N, \sigma_N) = A[\psi_1(\mathbf{r}_1, \sigma_1) \dots \psi_N(\mathbf{r}_N, \sigma_N)] , \quad (2.24)$$

where  $A$  is the antisymmetrising operator,  $N$  the total number of electrons in the system and  $\sigma$  is the spin variable. The excited states can be calculated using a screened configuration interaction (CI) approach [86, 87] where the exciton states are constructed using a linear combination of single-excited Slater determinants,  $\Phi_i^j$ :

$$\Psi^{ex} = \sum_i^{N_i} \sum_j^{N_j} c_{i,j} \Phi_i^j , \quad (2.25)$$

where  $c_{i,j}$  are expansion coefficients. In  $\Phi_i^j$ , an electron is promoted from an occupied (valence) state  $\psi_i$  to an unoccupied (conduction) state  $\psi_j$  and  $N_{i,j}$  stays for the number of valence and conduction states included in the CI expansion. Now the CI method approaches again the many-body level of theory, but, instead of many-electron wave functions, many configurations are implemented. With the basis set of Eq. (2.25) the exciton energies  $E^{ex}$  can be obtained solving the following equation:

$$\sum_k^{N_i} \sum_l^{N_j} c_{k,l} H_{ijkl} = c_{i,j} E^{ex} , \quad (2.26)$$

and the many-body Hamiltonian matrix elements can be calculated based on the

Hartree-Fock method [51, 52], as a difference between initial and final configuration:

$$\begin{aligned}
 H_{ijkl} &= \langle \Phi_i^j | H | \Phi_k^l \rangle = (\varepsilon_j - \varepsilon_i) \delta_{i,k} \delta_{j,l} - J_{ijkl} + K_{ijkl}, \text{ where} & (2.27) \\
 J_{ijkl} &= \sum_{\sigma_1, \sigma_2} \iint \psi_k^*(\mathbf{r}_1, \sigma_1) \psi_j^*(\mathbf{r}_2, \sigma_2) W \psi_i(\mathbf{r}_1, \sigma_1) \psi_l(\mathbf{r}_2, \sigma_2) d\mathbf{r}_1 d\mathbf{r}_2, \\
 K_{ijkl} &= \sum_{\sigma_1, \sigma_2} \iint \psi_k^*(\mathbf{r}_1, \sigma_1) \psi_j^*(\mathbf{r}_2, \sigma_2) W \psi_l(\mathbf{r}_1, \sigma_1) \psi_i(\mathbf{r}_2, \sigma_2) d\mathbf{r}_1 d\mathbf{r}_2.
 \end{aligned}$$

The Coulomb integral  $J$  describes the classical electron-electron interaction, and the exchange integral  $K$  is a Coulomb-like term which appears because of the antisymmetry of the wave functions [50, 88]. The  $W = 1/(\epsilon(\mathbf{r}_1, \mathbf{r}_2)|\mathbf{r}_1 - \mathbf{r}_2|)$  term represents the screened Coulomb interaction with certain dielectric function  $\epsilon$ , which will be described in detail in Section 4.4.

## 2.5 Single-particle, quasiparticle and optical band gaps

The solution of the single-particle (SP) Schrödinger equation using the AEP formalism defines the single-particle gap  $E_0$  as:

$$E_0 = \varepsilon_{e0} - \varepsilon_{h0}, \quad (2.28)$$

where  $\varepsilon_{e0}$  and  $\varepsilon_{h0}$  are the single-particle eigenvalues of the lowest unoccupied and the highest occupied orbital of the bulk crystal or the nanostructure, respectively.

Colloidal nanocrystals (NCs) are usually surrounded by an environment with corresponding dielectric properties. The dielectric mismatch between the nanocrystal and the surrounding medium leads to a surface polarization potential  $V_s$ , which corresponds to the classic electrostatic potential caused by a point charge inside the NC [86, 89]. This polarization effect must be included in the electron and hole self-energies of the exciton [90, 89] since these describe local charge properties. The polarization self-energies can be accounted for in the first principle *ab initio* methods, mainly using the *GW* approximation (see Section 2.2.1 for details), but with a large computational expense. For spherical nanostructures an analytic solution exists [89] which was shown to be in good agreement with first-principles result for

spherical QDs [91, 92]:

$$\sum_i^{\text{pol}} = \frac{1}{2} \sum_{\sigma} \int \psi_i^*(\mathbf{r}, \sigma) V_s(\mathbf{r}) \psi_i(\mathbf{r}, \sigma) d\mathbf{r} \quad , \quad (2.29)$$

$$\begin{aligned} \text{where } V_s(\mathbf{r}) = & \frac{1}{2R} \sum_{l=0}^{\infty} \frac{\epsilon_{\text{in}} - \epsilon_{\text{out}}}{\epsilon_{\text{out}} + l(\epsilon_{\text{in}} + \epsilon_{\text{out}})} \\ & \times \begin{cases} \frac{(l+1)(|\mathbf{r}|/R)^{2l}}{\epsilon_{\text{in}}} , & \text{if } |\mathbf{r}| < R \\ \frac{-l(|\mathbf{r}|/R)^{-2(l+1)}}{\epsilon_{\text{out}}} , & \text{if } |\mathbf{r}| > R \end{cases} \quad , \quad (2.30) \end{aligned}$$

where  $R$  denotes the radius of the QD,  $|\mathbf{r}|$  is the distance from the QD center, and  $l$  is the orbital angular momentum quantum number. When the dielectric constant of the QD  $\epsilon_{\text{in}}$  is equal to the dielectric constant of the medium  $\epsilon_{\text{out}}$ , the polarization potential  $V_s$  vanishes. The discontinuity at  $|\mathbf{r}| = R$  is smoothed out by the function  $1 - e^{-(r-R)^2/\lambda^2}$ , where  $\lambda = 0.163a_0$  in agreement with the width of the transition region defined in Ref.[93] is used. The quasiparticle (QP) band gap can be written as:

$$E_{\text{QP}} = E_0 + \sum_{e0}^{\text{pol}} + \sum_{h0}^{\text{pol}} \quad . \quad (2.31)$$

The optical, or excitonic, band gap corresponds to the creation of an interacting electron-hole pair, and can be obtained from the quasiparticle gap by subtracting the total electron-hole Coulomb interaction [91]. This corresponds to the single-configuration approach in CI:

$$E_{\text{opt}} = E_{\text{QP}} - J^{\text{total}} = E_0 + \sum_{e0}^{\text{pol}} + \sum_{h0}^{\text{pol}} - J^{\text{total}} \quad . \quad (2.32)$$

The relation between different energy terms considered in this work are shown schematically in Fig. 2.3. The subdivision of  $J^{\text{total}}$  into  $J^{\text{micro}}$  and  $J^{\text{pol}}$  will be explained in Section 4.4.4. For simplicity, the equations in the single-configuration (SC) approximation (no interaction between configurations) will be introduced, although a fully correlated CI approach is used in this work for the excited state calculations. The final results for isolated NCs, however, have very moderate contributions from the correlation between different configurations, so that the single-configuration picture is quantitatively quite accurate.

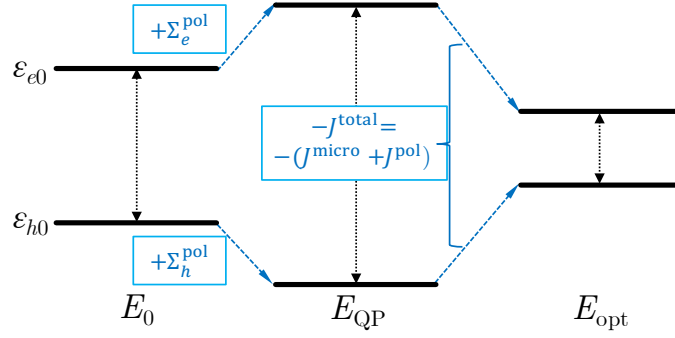


Figure 2.3: Scheme of the different energy gaps and the contributing energy terms from Eq. (2.28), Eq. (2.31) and Eq. (2.32). Reprinted from [94].

The exciton binding energy, taking in account Eq. (2.31) and Eq. (2.32), can be defined as following:

$$E_{\text{ex.bind}} = E_{\text{QP}} - E_{\text{opt}} \quad . \quad (2.33)$$

### 2.5.1 Exciton fine structure

The optical absorption features observed experimentally in the QDs are strongly influenced by the exciton fine structure (FS), which is sensitive to the crystal symmetry and exchange interactions. In particular, a resonant Stokes shift [95, 96] originate from the exciton dark-bright (DB) splitting. The lowest exciton FS formation starting from SP configuration in spherical QDs with ZB and WZ crystal structure and the role of the Coulomb and exchange interactions is shown schematically in Fig. 2.4. In experiments the absorption peak at room temperature corresponds to the first bright exciton state and the emission peak corresponds to the phonon-assisted long-term emission from the dark exciton state [84, 97]. In case of WZ structure, the hole states  $h_0$  and  $h_1$  are non-degenerate due to crystal field (CF) splitting.

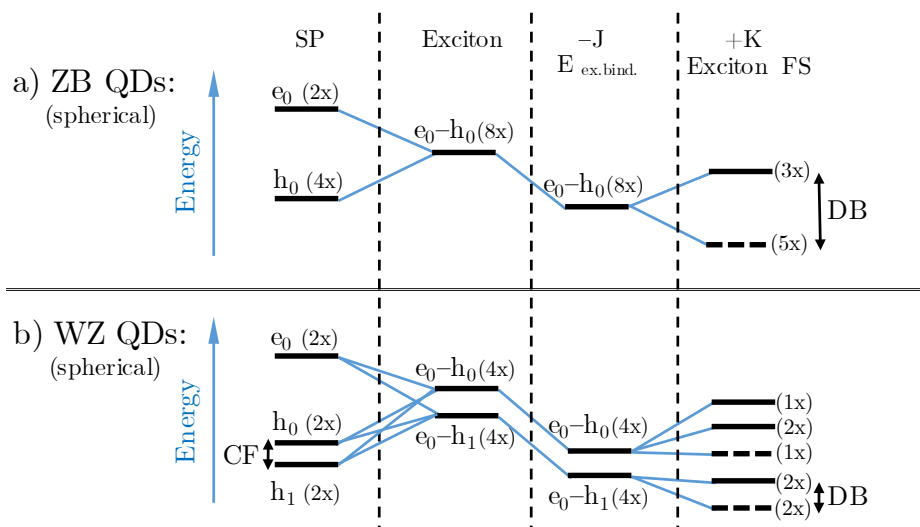


Figure 2.4: Schematic representation of the exciton FS formation from ground state electron (e, unoccupied) and hole (h, occupied) states (SO coupling included) for ZB and WZ spherical nanocrystals. Dashed lines in the exciton FS denote the optically passive dark states, where optical transition is forbidden due to selection rules [98], and optically active bright states are plotted with the solid lines. The difference in energy between first dark and first bright exciton state corresponds to DB splitting.

As it is represented in Fig. 2.4, the Coulomb interactions  $J$  (Eq. (2.27)) are generally long-distant and mostly determine the exciton binding energy ( $E_{\text{ex.bind}}$ , hundreds of meV range), whereas the exchange interactions  $K$  (Eq. (2.27)) are short-distant and responsible for the exciton FS splitting (tens of meV range).



## Chapter 3

# Motivation

The AEP approach inherits the imperfections of the local density approximation (LDA) used in the AEP generation, in particular, the delocalization of the electron charge [61] and consequently an underestimation of the single-particle band gap. Additionally, the spherical approximation used in the AEP derivation procedure is not suitable for atoms at the surface.

The treatment of the surface remained at a quality well below a full-fledged self-consistent *ab initio* treatment. Either the surface atoms were assumed to generate an electronic pseudopotential with a Gaussian shape determined by two or three parameters (depth, width, and distance from the surface atom) that could be adjusted to free the optical gap of surface states [99, 100], or the nanostructure was embedded in another artificial large band gap material [101, 102, 103]. A recent procedure [104] to extract passivant potentials based on DFT calculations and the semi-empirical approach [80, 81] used a spherical real-space description, required the adjustment of a passivant center (somewhat shifted with respect to the passivant position – already hinting at the non-spherical character of the passivant) and the fit to an ad-hoc Yukawa potential. These procedures were justified, to a certain extent, for large nanocrystals (NCs) [105, 106] or quantum wires (QWs) [107], where the electronic states in the proximity of the band gap region are well localized inside the nanostructure and only remotely affected by surface atoms. However, the influence of the surface on the electronic and optical properties is known to be significant. Moreover, the surface sensitivity represents one of the possible applications [108, 109, 110, 111, 112] of these nanostructures. Therefore, an accurate quantitative accounting of the surface effects is desirable.

The optical properties of the NCs are very sensitive not only to the crystal size due to the confinement effect. Even though the details of the surface passivation and ligands have been investigated theoretically to some extent based on *ab initio* calculations of very small NCs [113, 114, 115], the NCs are often also affected by the

embedding environment [86, 116]. The latter effect, i.e. the influence of the solvent and surface ligands dielectric properties on the optics is less understood and studied, and lacks connection between theory and experiment. Therefore, a detailed review of the different theoretical approaches [72, 91, 93, 117, 118, 119] and evaluation of the dielectric mismatch between crystal structure and surrounding media influence onto the optical properties of the NCs is necessary.

# Chapter 4

## Method development

### 4.1 Nanocrystals: structure and relaxation

All possible kinds of nanoparticles, in particular QDs and QWs, can be constructed using simple algorithms which allow cutting a certain shape out of bulk material. The optimal bulk lattice constant is defined from DFT calculations by finding the energy minimum of the bulk system. The results are listed in the Table 4.1 for the considered semiconductor materials.

Compound	$a_0$ (DFT)	$a_0$ (exp.)
CdSe (ZB)	6.13 Å	6.08 Å
CdSe (WZ)	a=4.33 Å; c=7.06 Å	a=4.30 Å; c=7.01 Å
CdS (ZB)	5.85 Å	5.82 Å
CdS (WZ)	a=4.14 Å; c=6.74 Å	a=4.13 Å; c=6.75 Å
InP (ZB)	5.90 Å	5.87 Å
InAs (ZB)	6.08 Å	6.06 Å
Si (ZB)	5.48 Å	5.43 Å
ZnS (WZ)	a=3.83 Å; c=6.25 Å	a=3.82 Å; c=6.26 Å

Table 4.1: Lattice constants for zincblende (ZB) and wurtzite (WZ) (see Section 1.2 for crystal structure details) bulk semiconductor materials, considered in this work, obtained after DFT optimisation, in comparison with experimental values from Ref.[120]. In the case of the WZ crystal structure both lattice parameters,  $c$  and  $a$ , are specified.

Even though the strain may affect the electronic properties of the nanocrystals (NCs) [121], most of the one-compound NCs might be constructed from the bulk material using the corresponding bulk lattice constant without further relaxation, and no considerable change of their electronic properties is observed (see Fig. 4.1).

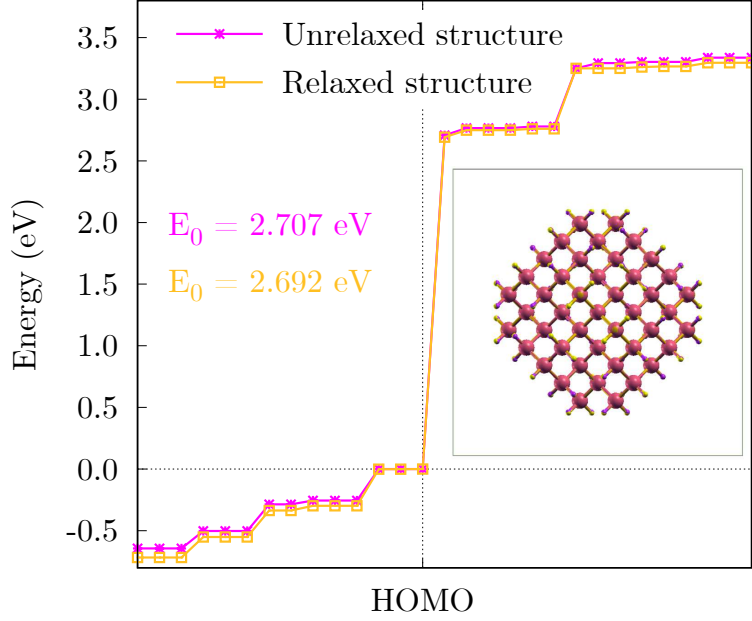


Figure 4.1: Eigenvalues near band gap for Si QD with  $R = 7.0 \text{ \AA}$ , calculated using DFT method before (pink stars) and after (yellow squares) structure relaxation. Inset: QD crystal structure before (pink) and after (yellow) relaxation

Average atom-atom distance follows the linear trend with respect to the number of atoms in the structure ( $N_{atoms}^{-1/3}$ ), i.e. the deviation between inter-atomic distance in the confined system and in bulk material is negligible for large systems and should increase for small ones [16]. Fig. 4.1 indicates, however, that the average atom-atom distances for Si atoms are not considerably changed after relaxation even for small QD (163 atoms including passivants) - only slight shift of passivant atoms is captured. Any compression effects on the NC surface are not observed. Therefore,  $E_0$  gap and eigenstates near band gap are not affected by the relaxation (meV deviations) in case of one-compound QDs. Similar results were obtained for InP and CdSe QDs.

Since passivant atom positions are changing after relaxation, the relaxed atom-to-passivant distance change is important for the slab surface during the AEP construction procedure (see Section 4.2.1 for details) and was done using the DFT code ABINIT [122]. In the NC construction code, atom-to-passivant distance defined from slab is used, however, an additional algorithm for the surface passivation is implemented, which allows avoiding experimentally unstable configurations, in particular surface atoms with three passivants and close distances between two neighboring passivants.

### 4.1.1 Valence force field model for core-shell QDs

For the heterogeneous (core-shell) NCs the lattice constant mismatch between core and shell material leads to considerable changes in their electronic and optical properties. The relaxation of the core-shell interface is therefore necessary.

A combination of conjugate-gradient methods with standard molecular dynamics [45, 123] is the state-of-art precise way for structure relaxation. However, these algorithms are rather computationally demanding and not suitable for systems with more than 1000 atoms. The valence force field (VFF) model of Keating [124, 125] is a computationally cheap alternative, which gives a reasonable quality of the interface relaxation. In this method the elastic energy per atom is calculated:

$$U_i = \frac{3\alpha}{16r_0^2} \sum_{j=1}^4 (\mathbf{r}_{ij}^2 - r_0^2)^2 + \frac{3\beta}{8r_0^2} \sum_{j=1}^4 \sum_{k>j}^4 \left( \mathbf{r}_{ij} \cdot \mathbf{r}_{ik} + \frac{r_0^2}{3} \right)^2, \quad (4.1)$$

where  $r_0$  is the equilibrium bond length of the corresponding bulk material,  $\mathbf{r}_{ij}$  is a vector between an atom  $i$  and its nearest neighbour  $j$ . The first part of Eq. (4.1) defines the bond stretching terms and the second part accounts the bond bending angle terms. The  $\alpha$  and  $\beta$  are the corresponding parameters, which can be derived for each bulk semiconductor material from the experimentally measured macroscopic elastic constants  $c_{11}$ ,  $c_{12}$  and  $c_{44}$ [124, 125]:

$$c_{11} = \frac{1}{a_0}(\alpha + 3\beta); \quad c_{12} = \frac{1}{a_0}(\alpha - \beta); \quad c_{44} = \frac{4}{a_0} \frac{\alpha\beta}{(\alpha + \beta)}. \quad (4.2)$$

If the atom  $k$  and atom  $j$  belong to different materials (core-shell interface), the averaged bond-bending constant is used. The elastic parameters used for InAs/InP and CdSe/CdS materials within the VFF framework are specified in the Table 4.2.

Compound	VFF( $\alpha$ )	VFF( $\beta$ )
CdSe	32.230	5.218
CdS	40.289	5.534
InP	32.614	4.342
InAs	43.842	4.677

Table 4.2: Bond-stretching ( $\alpha$ ) and bond-bending ( $\beta$ ) constant for bulk semiconductor materials, considered in this work, calculated from [126, 127] using Eq. (4.2).

The total energy of the system is calculated by summing up elastic energies for individual atoms. For the atomic position which differs from  $r_0$  the given atom

receives a penalty in elastic energy according to Eq. (4.1). The VFF relaxation mechanism is based on the total elastic energy minimization and can be separated in two steps. During the first step the gradient of the elastic energy minimization is defined for individual atoms by their random movement, and during the second step the shifts of single atoms are performed according to this gradient until the total energy minimum is reached. The average elastic energy change per atom is used in the code as a main convergence criterion to make the relaxation quality independent from the number of atoms.

To capture the changes with relation to ideal bulk interatomic distances and bond angles, the relaxed InAs/InP core-shell QDs with the sharp and alloyed interface was calculated using VFF method, and bond lengths and bond angles is plotted (Fig. 4.2).

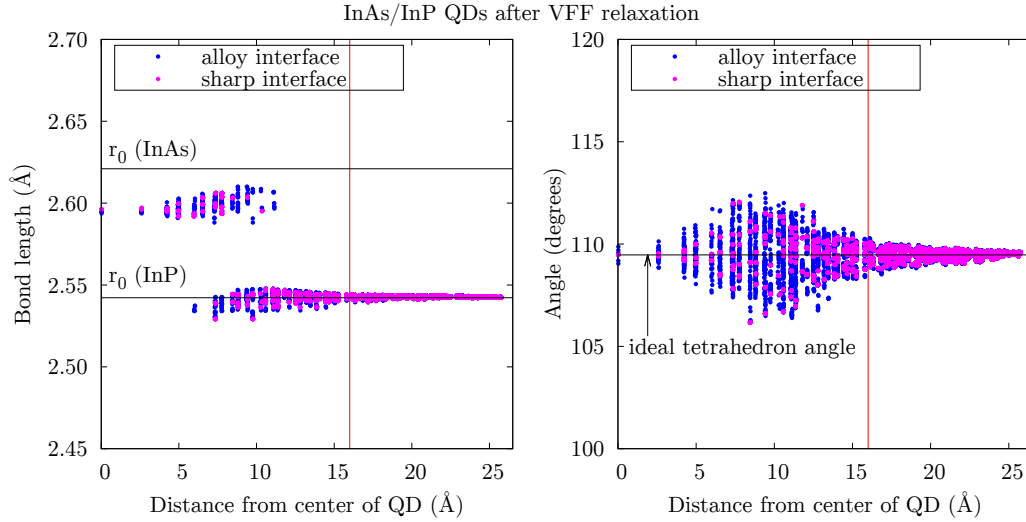


Figure 4.2: Bond lengths (left) and bond angles (right) for the InAs/InP core-shell QDs after VFF relaxation. Final-size cut of  $R = 16\text{\AA}$  is shown with the red line. QD with the sharp interface (pink circles) consists of InAs core with  $R = 8\text{\AA}$  and  $8\text{\AA}$  thick InP shell on top, whereas QD with the alloyed interface (blue circles) consists of InAs core with  $R = 6\text{\AA}$ , the alloyed interface with width  $4\text{\AA}$  and  $6\text{\AA}$  thick InP shell.

The VFF starting point is a compressed quantum dot, and a slight compression ( $0.5 - 1\%$ ) of core material might remain after relaxation. The bond length in the shell corresponds to  $r_0$  for InP, with deviations no more than  $0.3\%$  near the core material. The alloyed interface leads to slightly more deviations from the ideal bond lengths than the sharp interface, but the overall quality of the relaxation is preserved. The angles in InAs/InP QDs are deviating up to  $2.5\%$  from the ideal tetrahedron value, again a bit more in case of the alloyed interface. In order to avoid spurious bond and angle deviations near the QD surface in the final structure

and also to construct a passivant shell, around  $5\text{\AA}$  extra shell thickness should be used for VFF relaxation.

The quality of relaxation is usually defined by calculating the Hellman-Feynman forces [128]. The forces per atom were calculated for the InAs/InP QD with the alloyed interface using ABINIT code before and after VFF relaxation (see Fig. 4.3).

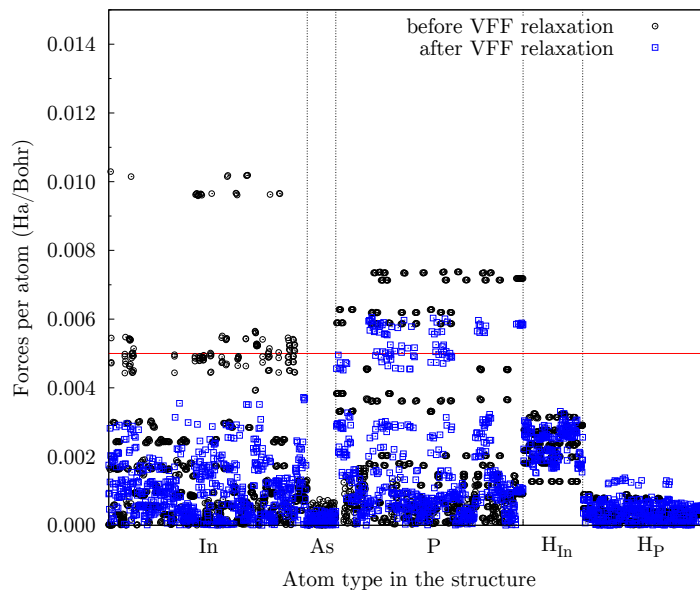


Figure 4.3: Hellman-Feynman forces (cartesian components) per atom for the InAs/InP core-shell QD with the alloyed interface, total  $R = 16\text{\AA}$  (InAs core with  $R = 6\text{\AA}$ , the alloyed interface with width  $4\text{\AA}$  and  $6\text{\AA}$  thick InP shell) before(black) after (blue) VFF relaxation. Relaxation threshold corresponding to the Hellman-Feynman forces  $5 \times 10^{-3}$  Ha/Bohr is shown with the red line.

To reliably converge the total energy minimum in *ab initio*-based ground state calculations, these forces should not exceed  $5 \times 10^{-3}$  Ha/Bohr per atom [129]. The forces after VFF relaxation are considerably lower than in the non-relaxed structure and acceptable for the further ground state and excited state calculations. The VFF method is transferable and can be implemented for other semiconductor materials.

## 4.2 Non-spherical atomic effective pseudopotentials for passivant atoms

As it was mentioned in Section 2.3, spherical AEPs, which were developed previously, are not suitable for surface atoms. Here non-spherical AEPs for the surface, or passivant, atoms are introduced, for which the imaginary part of the potential in

reciprocal space is preserved during the potential derivation process, which corresponds to a real-space potential that has no inversion symmetry. The non-spherical nature of the passivant AEP allows reproducing the surface dipoles which generate a band offset to vacuum.

### 4.2.1 Passivant potential derivation

The passivant potential is introduced by rewriting the potential from Eq. (2.17) explicitly for a binary cation-anion system with two types of passivants denoted by  $v_{H1}$  and  $v_{H2}$ :

$$\begin{aligned} \Omega_c V^{\text{loc}}(\mathbf{G}) &= \left( \sum_n^{N_c} e^{-i\mathbf{G}\cdot\boldsymbol{\tau}_{c,n}} \right) v_c(\mathbf{G}) + \left( \sum_n^{N_a} e^{-i\mathbf{G}\cdot\boldsymbol{\tau}_{a,n}} \right) v_a(\mathbf{G}) + \\ &+ \left( \sum_n^{N_{H1}} e^{-i\mathbf{G}\cdot\boldsymbol{\tau}_{H1,n}} \right) v_{H1}(\mathbf{G}) + \left( \sum_n^{N_{H2}} e^{-i\mathbf{G}\cdot\boldsymbol{\tau}_{H2,n}} \right) v_{H2}(\mathbf{G}) = \\ &= S_c v_c(\mathbf{G}) + S_a v_a(\mathbf{G}) + S_{H1} v_{H1}(\mathbf{G}) + S_{H2} v_{H2}(\mathbf{G}) \quad , \end{aligned}$$

where  $S_{c,a,H1,H2}$  are the structure factors of the cations, anions, and of the passivants  $H1$  and  $H2$  that are bound to the cations or anions, respectively. The structure factors depend only on the atomic positions. Reordering the terms leads to:

$$S_{H1} v_{H1}(\mathbf{G}) + S_{H2} v_{H2}(\mathbf{G}) = \Omega_c V^{\text{loc}}(\mathbf{G}) - S_c v_c(\mathbf{G}) - S_a v_a(\mathbf{G}) \quad , \quad (4.3)$$

where all is known but  $v_{H1,2}(\mathbf{G})$ , which are kept as complex quantities. To solve the equation of two unknowns a second slab is introduced, and both systems are denoted with  $A$  and  $B$ :

$$\begin{aligned} S_{H1}^A v_{H1}(\mathbf{G}) + S_{H2}^A v_{H2}(\mathbf{G}) &= \Omega_c V_A^{\text{loc}}(\mathbf{G}) - \\ &- S_c^A v_c(\mathbf{G}) - S_a^A v_a(\mathbf{G}) \quad , \\ S_{H1}^B v_{H1}(\mathbf{G}) + S_{H2}^B v_{H2}(\mathbf{G}) &= \Omega_c V_B^{\text{loc}}(\mathbf{G}) - \\ &- S_c^B v_c(\mathbf{G}) - S_a^B v_a(\mathbf{G}) \quad . \end{aligned} \quad (4.4)$$

The sum and difference of both equations is taken to obtain the system of equations, used to derive AEPs for atomistic passivant atoms.

Three target properties are considered for the choice of the structures  $A$  and  $B$  used for the passivant AEPs derivation. First, the supercell should be significantly elongated in one dimension, in order to provide a dense grid of  $\mathbf{G}$ -points along this

extended direction. Second, the system should be still manageable for calculations using standard DFT-LDA approach (from the  $V_{(1,2)}^{\text{loc}}$  is obtained). Third, the physical properties of the passivated surface should be representative and transferable for the calculations of the different nanostructures (QWs, QDs). It turns out, that a slab geometry which is schematically shown in Fig. 4.4a) suits all the mentioned conditions. Both systems *A* and *B* differ only by one atomic layer in the length of the slabs used, while the size of the supercell and hence the FFT grid of  $\mathbf{G}$ -vectors is kept constant.

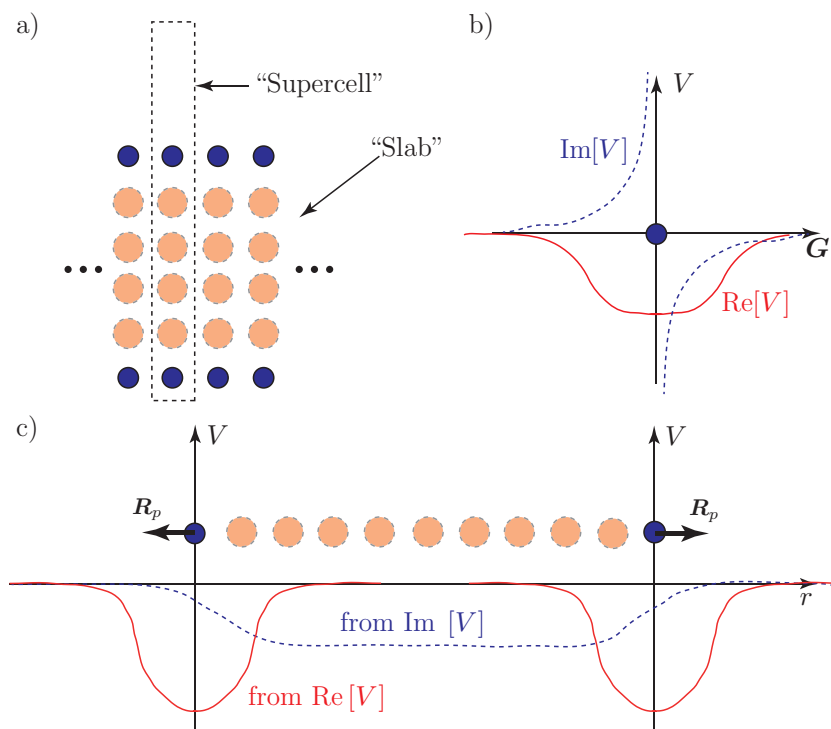


Figure 4.4: a) Schematic representation of the “slab” geometry used to calculate the passivant AEPs. b) Real and imaginary components of the hydrogen (passivant) pseudopotential in reciprocal space. The imaginary part is odd and peaked towards  $\mathbf{G}=0$  with  $\text{Im}[V(\mathbf{G}=0)] = 0$ . c) Potential in real space for two passivants with vectors pointing in opposite directions, corresponding to the situation in the slab geometries. The real space potential (a real quantity) is divided into a part originating from the real reciprocal-space potential and a part originating from the imaginary part of the reciprocal-space potential. Reprinted from [130].

From the full reciprocal-space potential obtained from the self-consistent DFT calculations  $V_{(1,2)}^{\text{loc}}(\mathbf{G})$  only the grid points along the extended direction of the supercell in the direction of the crystallographic growth orientation are used, which is the  $z$ -direction in this case:

$$V_{(1,2)}^{\text{loc}}(\mathbf{G}) \equiv V_{(1,2)}^{\text{loc}}(0, 0, G) \quad . \quad (4.5)$$

The solution of the system of equations formed from Eq. (4.4) gives  $v_{\text{H1,2}}(G)$ , where  $G$  is the length of the considered  $\mathbf{G}$ -vector.

For the real component of  $v_{\text{H1,2}}(G)$  a spherical approximation:  $\text{Re } v_{\text{H1,2}}(G) = \text{Re } v_{\text{H1,2}}(|G|)$  is made. For the imaginary component  $\text{Im } v_{\text{H1,2}}(G) = \text{Im } v_{\text{H1,2}}(|G|)$  is also valid, keeping in mind that  $\text{Im } v_{\text{H1,2}}(G) = -\text{Im } v_{\text{H1,2}}(-G)$ . When the passivant AEPs are extracted from Eq. (4.4) using a slab geometry as in Fig. 4.4a), AEPs for two passivants are obtained. If these passivants are identical (in case of a passivants for a group IV semiconductors such as Si), then their real parts are identical and their imaginary parts have same magnitudes but opposite signs.

This follows the expectation that the asymmetry in real space must be reversed at both interfaces. The real and imaginary parts of the passivant AEP are illustrated in Fig. 4.4b) showing an even real and an odd imaginary potential. The passivant AEPs are stored with the imaginary sign corresponding to the passivant orientation in the slab geometry (pointing upwards).

The contribution of the passivants in Eq. (2.17) to the total reciprocal-space potential is written as:

$$V_{\text{H}}(\mathbf{G}) = \frac{1}{\Omega_c} \sum_n^{N_{\text{H}}} e^{-i\mathbf{G}\cdot\boldsymbol{\tau}_{\text{H}n}} v_{\text{H}}(\mathbf{G}) \approx \frac{1}{\Omega_c} \sum_n^{N_{\text{H}}} e^{-i\mathbf{G}\cdot\boldsymbol{\tau}_{\text{H}n}} \left( \text{Re } v_{\text{H}}(G) + i \frac{\mathbf{G} \cdot \mathbf{R}_p}{|\mathbf{G}||\mathbf{R}_p|} \text{Im } v_{\text{H}}(G) \right) , \quad (4.6)$$

where  $\mathbf{R}_p$  is the real space surface normal vector in Cartesian coordinates, denoting the direction of the antisymmetric component introduced by the imaginary part. Eq. (4.6) represents a generalization of the one-dimensional case where  $\mathbf{G}$  and  $\mathbf{R}_p$  are parallel or anti-parallel to a situation where they have arbitrary orientation. The only known solutions are for the limiting cases of parallel/anti-parallel vectors (prefactor to imaginary part 1/-1) or perpendicular (prefactor to imaginary part 0, keeping spherical (real) potentials in-the-plane). A cosine function (dot-product) connecting both cases is used as the simplest possible assumption. Fig. 4.4c) shows the qualitative situation with the AEP in real space originating from the real and imaginary components of the reciprocal-space passivant AEP.

First, the AEP for the passivants on the surface of Si are derived. Two different slab geometries (slab A and slab B) are shown in Fig. 4.5a). Both slabs are oriented along the  $[\mathbf{111}]$  crystallographic direction and the bonds to the passivant atoms point in this direction as well, forming a normal to the surface. The supercells of around 11.4 nm length are used in order to obtain a dense grid of  $\mathbf{G}$ -points. The DFT calculations are performed with the code ABINIT [122], where the Si-H

bond are structurally relaxed in the  $[111]$  direction. The hydrogen atoms for the III-V and the II-VI materials are actually pseudo-hydrogens with fractional charges as typically used in DFT calculations [104, 131], which return a neutrally charged nanocrystal. One should keep in mind that some experimental situations will differ from this artificial case. The approach suggested, however, does not rely on the use of pseudo-hydrogens with fractional charge, but allows to introduce any atomic passivant.

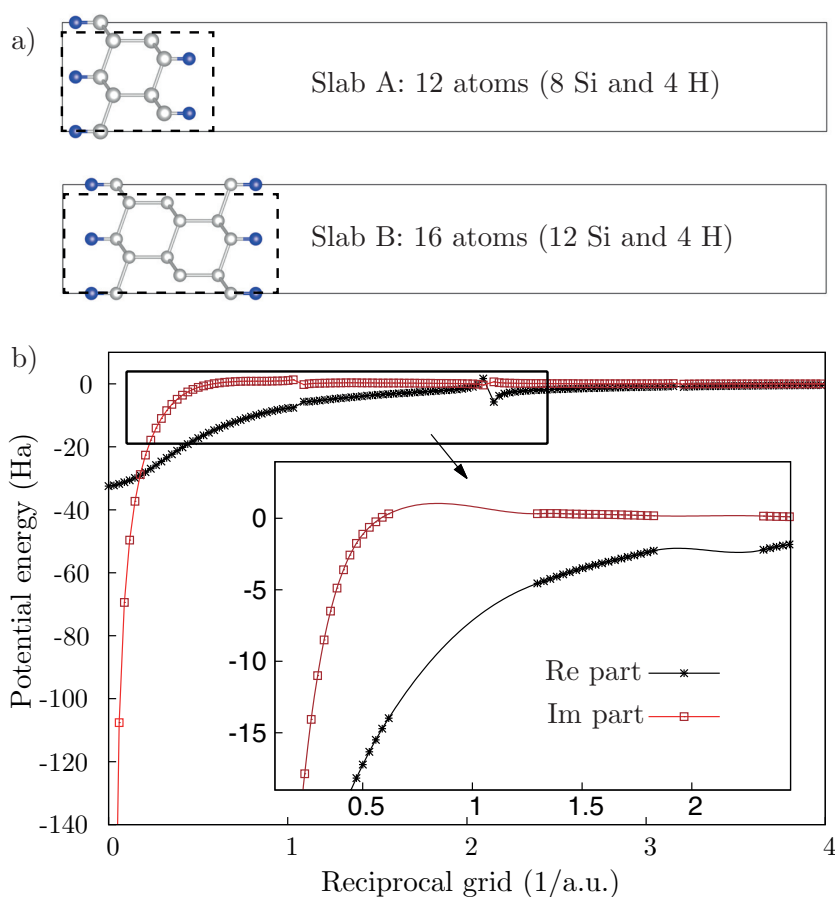


Figure 4.5: a) Atomic positions for silicon (gray) and hydrogen (blue) in slab A and slab B used in the extraction of the passivant AEPs. The slabs have zincblende structure and the passivant atoms (blue) are pointing in the crystallographic  $[111]$  and  $[\bar{1}\bar{1}\bar{1}]$  directions. b) AEPs for the Si passivant as a function of  $|\mathbf{G}|$ , black stars represent the real part and red squares the imaginary part of the potential. The symbols (stars and squares) are the raw data points and the lines reproduce the final AEPs. Reprinted from [130].

The results for the passivant (hydrogen) AEP of silicon are shown in Fig. 4.5b). The real part is shown in black while the imaginary part of the potential is shown in red. The symbols show the discrete data points obtained directly from the processing of the DFT calculations. The straight lines are cubic spline interpolations through the data points. In the region of  $|\mathbf{G}| = n \cdot 2\pi\sqrt{3}/(a_0)$  (case of  $[111]$  crystal

orientation along  $z$ ), where  $n$  is an integer and  $a_0$  the bulk lattice constant, the data point extraction suffers from the error which is intrinsically carried over from the bulk AEPs. Since the goal for the passivant AEP is not to correct the deviations existing within the bulk AEPs, the data points in the vicinity of these  $|\mathbf{G}|$  values are omitted. By using these data points, one may indeed obtain better agreement than by ignoring them for a specific structure, but the transferability to the structures with other dimensions and configurations would be less accurate. The passivant effective potential shows a very steep imaginary part for small  $G$ -values and a rather smooth real part, comparable to the bulk AEPs [70].

Before assessing the quality of the derived pseudopotential for the nanostructures, a single passivant in an empty supercell was considered. To estimate the effect of the newly defined imaginary component of the potential qualitatively, the AEP for an isolated passivant in real space is plotted in Fig. 4.6, orientated via the vector  $\mathbf{R}_p$  (see Eq. (4.6)).

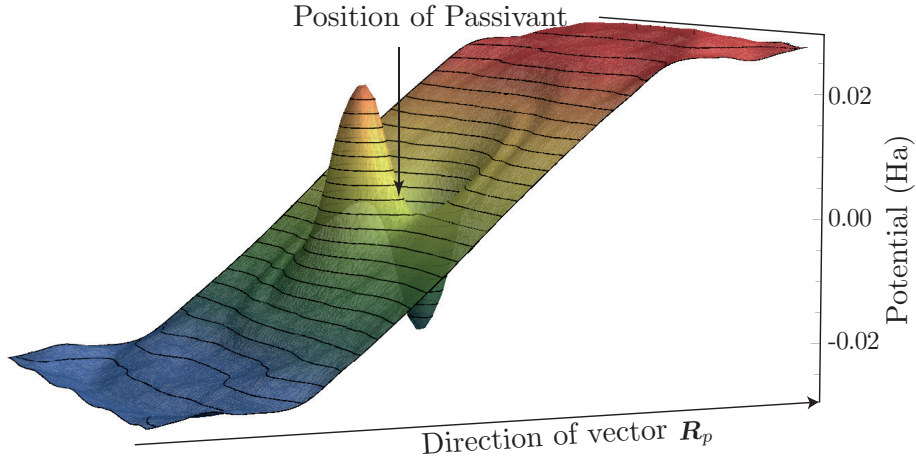


Figure 4.6: Real space potential of an isolated hydrogen passivant, when only the imaginary part of the reciprocal-space AEP is considered. The passivant is oriented by the vector  $\mathbf{R}_p$  (see Eq. (4.6)). Reprinted from [130].

The corresponding spherical real part is significantly deeper and not shown explicitly, i.e., only the imaginary part of the reciprocal-space potential is shown in Fig. 4.6. The asymmetric part exhibits two components: a short-ranged one, localized in the proximity of the passivant core, and a long-ranged component that introduce a clear band-offset type potential, which might be also observed in Fig. 4.5b). In case of experimental systems, the charge transfer around the passivant should form the surface dipole leading to such a band offset. It is reassuring to observe that the imaginary part of the potential is able to capture the correct physics behind.

### 4.2.2 Passivant potentials for different crystallographic directions

To challenge the transferability of the derived AEPs by comparing different slab orientations, several crystallographic surfaces were considered, and the relevant structural information is summarized in Table 4.3.

Crystallographic plane	[100]	[110]	[111]
$N_{\text{Si}}$	16	28	24
$N_{\text{H}}$	4	4	4
$\rho(\text{H})(1/\text{nm}^2)$	13.4	9.4	7.7
$r_{\min}(\text{H-H}) (\text{\AA})$	1.51	3.12	3.87
$E_0$ (DFT) (eV)	0.896	0.906	1.004
$E_0$ (AEP) (eV)	0.987	1.019	1.133

Table 4.3: Structural parameters and band gap at the  $\Gamma$ -point for Si slabs with ZB structure and with different crystallographic orientations. The passivant (hydrogen) density on the surface is given as  $\rho(\text{H})$  and the minimum distance between passivant atoms as  $r_{\min}(\text{H-H})$ .

In Fig. 4.7 the atomic structures of the different surfaces are plotted, the valence band maximum (VBM) and the conduction band minimum (CBM) wave functions calculated with DFT (red) and with AEPs (blue) along with error bars for the eigenvalue differences for states around the band gap, aligned at the VBM level.

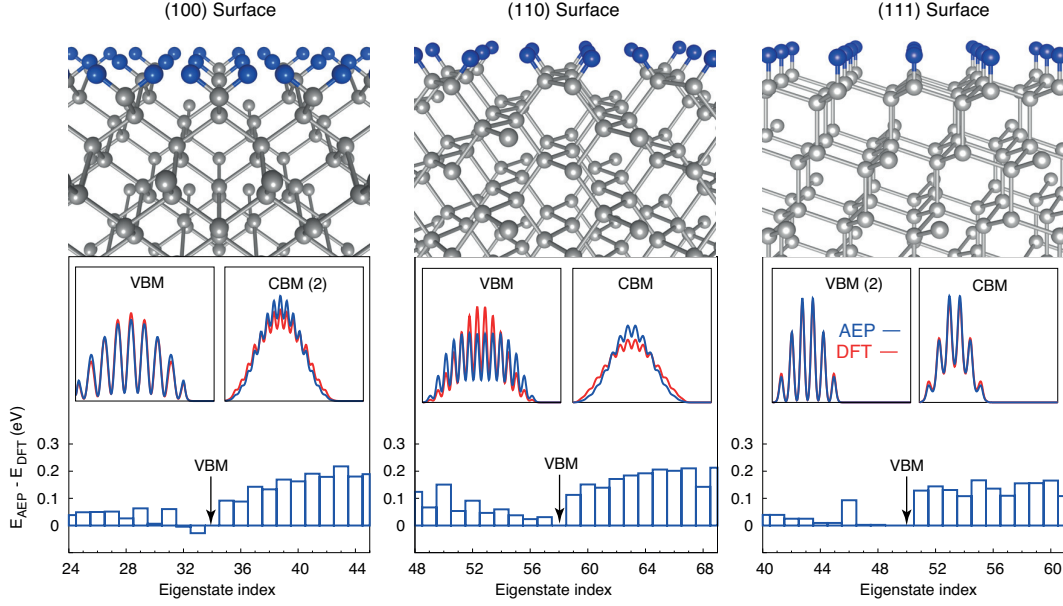


Figure 4.7: Comparison between AEPs and DFT results for  $[100]$ ,  $[110]$  and  $[111]$  surfaces. The geometries of the different slabs are given at the top of the figure. The middle panels show the DFT (red) and AEP (blue) wave functions across the slabs along the growth direction. The degeneracy of the states is given in brackets. The lower part shows the difference between the AEP and the DFT eigenvalues as bar charts. The eigenvalues were aligned with respect to the VBM. Reprinted from [130].

From the Fig. 4.7 it follows that the deviations from DFT results are within a range of 200 meV and occur mainly for the conduction band states. Please note, that the error of the AEP for the bulk band gap of Si is 87 meV [70]. So all the conduction band states suffer from the 87 meV error coming from the bulk Si AEP and of the errors introduced by the passivant AEP. Both errors seem to be of similar magnitude, which substantiates the good quality of the approach.

### 4.2.3 Atomistically passivated Si nanostructures

The areas of application of the AEPs are nanostructures. First, the quality of AEPs was assessed for quantum wires (QWs). A graphical representation of the atomic positions for a Si quantum wire with the radius around  $15\text{\AA}$  and average passivant density on the surface  $\rho(H) = 12.33$  ( $1/\text{nm}^2$ ) is given in Fig. 4.8a).

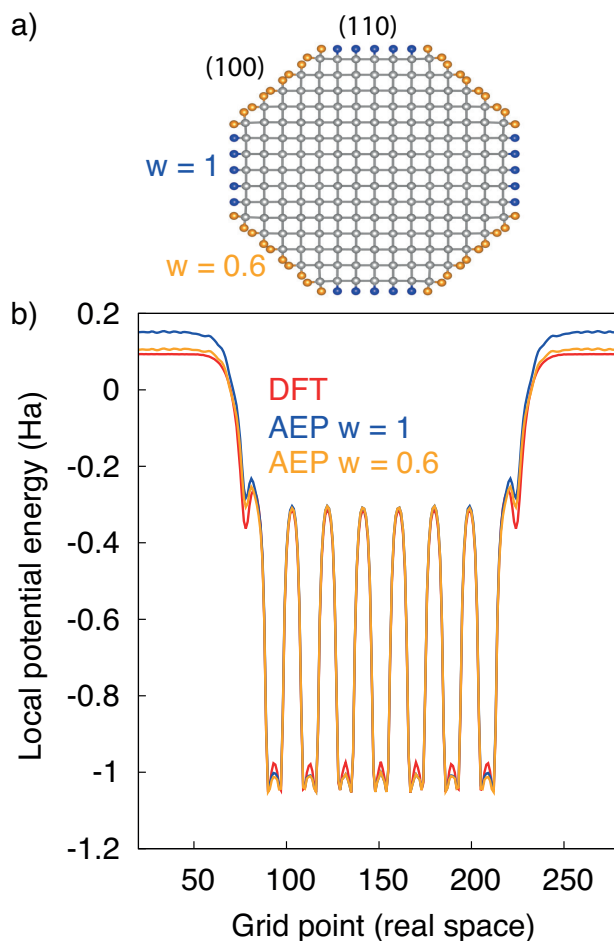


Figure 4.8: a) The geometry of the Si quantum wire with the  $R = 15\text{\AA}$ . The hydrogens carrying a weight parameter ( $w$  in Eq. (4.7)) of  $w = 0.6$  are shown as orange spheres while the unweighted hydrogens ( $w = 1$ ) are shown in blue. b) corresponding local potentials through the center of the QW across XY plane of the supercell. Reprinted from [130].

The local potential is given in Fig. 4.8b) and demonstrates the positive vacuum-offset, introduced by the imaginary part of the passivant potential. The comparison between DFT (red) and AEP (blue) shows that the AEP reproduces the potential very well in general but significantly overestimates the band offset (the blue line in the vacuum region is significantly above the red line), which has direct repercussions on the eigenvalues of excited states close to the vacuum. This effect is related to the density of hydrogen atoms  $\rho(H)$  on the surface. As seen from Table 4.3, the hydrogen atom surface density for Si slabs with  $[100]$  and  $[110]$  crystal direction is significantly higher than for the  $[111]$  Si slab used in the AEP construction. A closer look at the QW geometry, shown in Fig. 4.8a), reveals that its surface is composed of facets corresponding to  $[100]$  and  $[110]$  crystallographic directions. In the  $[100]$  direction, two hydrogen atoms are connected to one Si atom. In order to

Radius (Å)	7.0	11.0	12.5	15.0
$\rho(\text{H})$ (1/nm <sup>2</sup> )	12.49	11.54	11.21	10.56
$E_0$ (DFT) (eV)	2.692	1.877	1.664	1.498
$E_0$ (AEP) (eV)	2.723	1.944	1.755	1.536

Table 4.4: Structural parameters and  $E_0$  band gaps of different Si quantum dots.  $N_{\text{Si}}$  gives the number of Si atoms in the quantum dot and  $N_{\text{H}}$  the number of hydrogen passivants. The hydrogen densities on the surfaces are given as  $\rho(\text{H})$ .

systematically reduce the generated offset based on a density argument, a weight factor  $w$  is applied to the imaginary part, so Eq. (4.6) is modified as:

$$\begin{aligned}
 V_{\text{H}}(\mathbf{G}) = \frac{1}{\Omega_c} \sum_n^{N_{\text{H}}} & e^{-i\mathbf{G}\cdot\boldsymbol{\tau}_{\text{H}n}} (\text{Re } v_{\text{H}}(G) + \\
 & + i \frac{\mathbf{G}\cdot\mathbf{R}_p}{|\mathbf{G}||\mathbf{R}_p|} w \text{Im } v_{\text{H}}(G)) \quad .
 \end{aligned} \tag{4.7}$$

The weight factor  $w = 0.6$  might be applied if a surface atom is passivated by two hydrogen atoms, which corresponds to the ratio of the densities between slab [111] and [100]. The results for the potential in the vacuum region, i.e. the offset, is significantly improved by the use of weights, as can be seen (orange curve) in Fig. 4.8b). The same result might be achieved by the derivation of two separate passivant AEPs, one generated from a [111] slabs and one from a [100] slabs. Both potentials might be used on the respective facets of a Silicon QW with 3.0 nm diameter (as shown in Fig. 4.8a)). The results were improved for states close to the band gap from an error of 30 meV to below 10 meV. However, this improvement on already very small scale, was not systematic for all the states considered. Overall, an improvement of the results is possible using this technique, which has the benefit to contain no weight parameter, but rather more complicated from the derivation procedure.

QDs are the most challenging nanostructures in terms of transferability as the passivant atoms point virtually in all directions. In the AEP approach ideally passivated nanostructures are considered. The structural information as well as the numerical results for the band gaps are given in Table 4.4 for four different silicon quantum dots. It is important to notice, that the  $E_0$  gaps are in good agreement with the DFT results for all the sizes considered.

Next, the quantum dot with the radius 15Å, which represents the size comparable to experiment, was contemplated. The results are presented in Fig. 4.9, where the eigenvalues in a large range of energy as well as the error bars between DFT and AEP results are represented, similar to what is shown in Fig. 4.7. The match

between AEP and DFT calculations is excellent, with the deviations below 50 meV.

The probability density of a wave function  $\psi_i$  corresponds to  $|\psi_i|^2$ . The wave functions are orthonormal by definition and therefore for each wave function  $\psi$  must be fulfilled the condition from Eq. (2.7). The quality of the AEP wavefunction can be judged by projecting them onto the DFT wave functions:

$$\langle \psi_i^{\text{AEP}} | \psi_i^{\text{DFT}} \rangle \leq 1 \quad . \quad (4.8)$$

The closer is the result of projection to 1.0, the more AEP and DFT wave functions are similar to each other (1.0 would mean identical). The actual values are very close to 1.0, with some improvement if the weight parameter (Eq. (4.7)) is implemented. In the lower panel of the Fig. 4.9 selected wave functions as one-dimensional plots across the center of the quantum dot are shown. Wave functions of degenerate eigenstates are summed and their degeneracy is denoted in brackets. The values are the exact numerical values of the projection onto the DFT wave functions. The DFT results (red) and the AEP results with weight (orange) show very good agreement. The insets in the upper part of the Fig. 4.9 shows three-dimensional isosurface-plots of the highest occupied nanocrystal state (HOMO) and the lowest unoccupied nanocrystal state (LUMO), showing clearly confined envelope states.

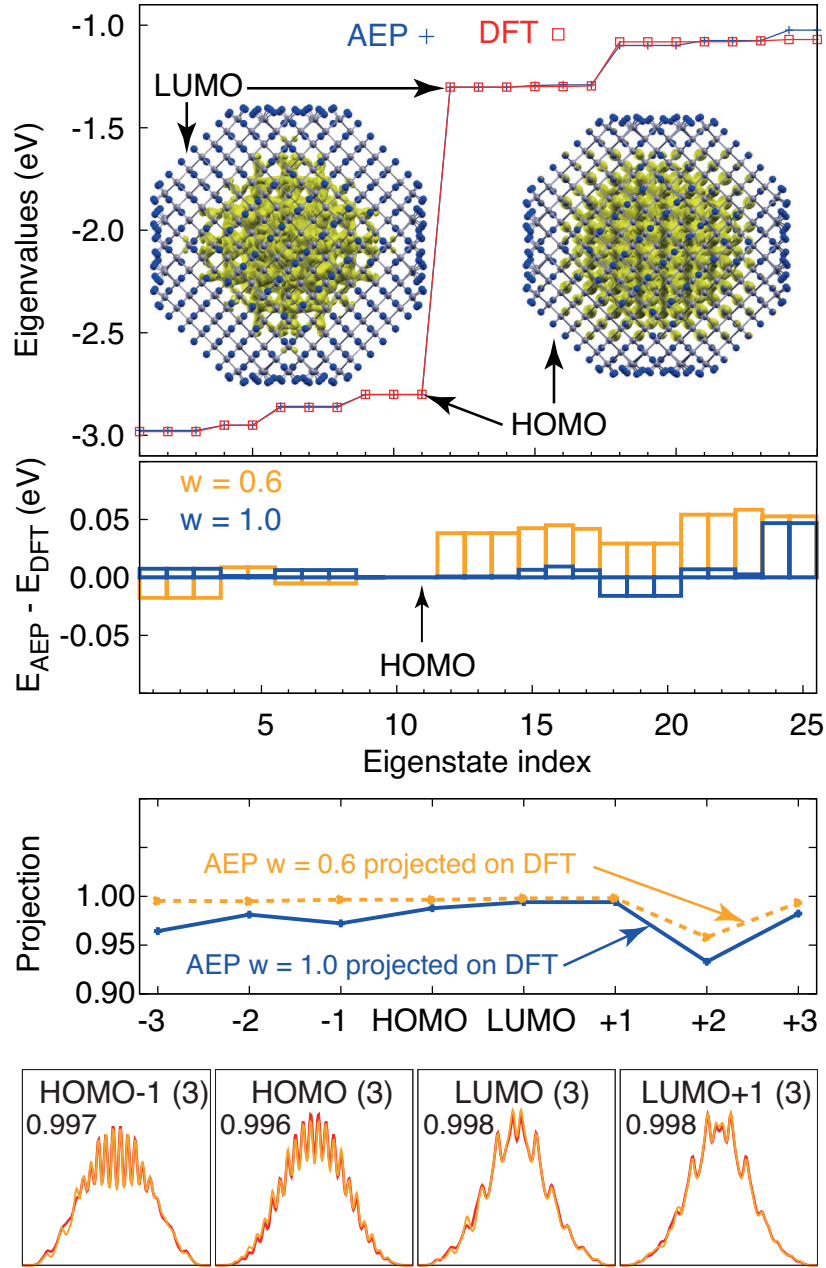


Figure 4.9: DFT and AEP results for a silicon quantum dot with the radius of  $15\text{\AA}$  (see Table 4.4). The eigenvalues and the eigenvalue differences are given in the upper two panels. The projection is calculated as in Eq. (4.8) and describes the quality of the AEP wave functions. Selected wave functions around the band gap are plotted explicitly in one-dimension across the quantum dot in the lower panels. The insets of the upper panel show three-dimensional plots of the isosurfaces of the HOMO and LUMO wave functions. Reprinted from [130].

The importance of the imaginary part (which is responsible for the asphericity of the passivant potential) is reassessed by calculating the eigenvalues and eigenstates using only the real-space component of the AEP. The results of this “spherical ap-

proximation” are shown in Fig. 4.10. The major qualitative discrepancies can be observed in the conduction states (LUMO and above) as well as some quantitative differences occurring in the valence states (HOMO and below). The surface dipoles, which can be modeled by the non-spherical complex passivant AEP, form the band-offset to vacuum which is essential for the correct reproduction of the CB in colloidal nanostructures. The degeneracy of the LUMO is entirely different when the imaginary part of the potential is neglected. The splitting between the HOMO states tends to be overestimated within the spherical passivant approximation.

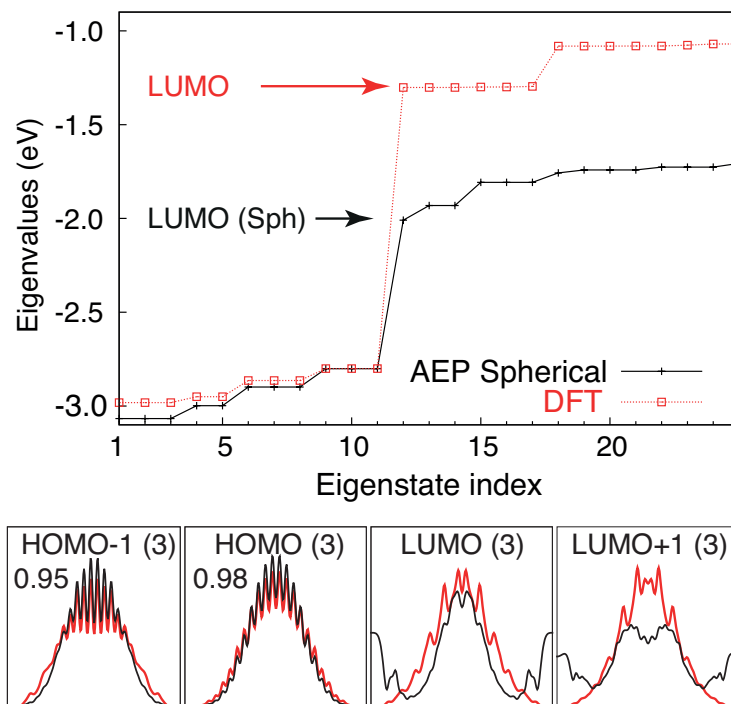


Figure 4.10: Eigenvalues of the Si quantum dot with radius 15 Å (top panel) calculated via DFT and calculated using AEPs without the imaginary component (AEP spherical). Selected wave functions around the band gap calculated with DFT and AEP spherical are shown at the bottom panel). Reprinted from [130].

#### 4.2.4 Atomistic passivation for other semiconductor materials

In order to show AEP method quality for different semiconductor materials, a quantitative comparison of the eigenvalues obtained for Si, InP and CdSe QWs with the radius around 7 Å is performed. Each quantum wire is constructed along the [100] crystallographic direction in case of ZB crystal structure (Si and InP) or along the [0001] direction in case of WZ crystal structure (CdSe). The structural information is given in Table 4.5. The average hydrogen density are similar to the values obtained for the Si QDs (Table 4.4).

QW	Si	InP	CdSe
QW Radius	6.5Å	6.5Å	7Å
$\rho(\text{H})$ (1/nm <sup>2</sup> )	12.47	11.50	11.69
$E_0$ (DFT) (eV)	2.147	1.771	1.475
$E_0$ (AEP) (eV)	2.165	1.911	1.628

Table 4.5: Structural parameters and band gaps of different QWs. The Si and InP QWs have ZB crystal structure while the CdSe QW has WZ structure. The passivant density on the surface is given as  $\rho(\text{H})$ .

The eigenvalues around the band gap are presented in Fig. 4.11. In the upper panels, an energy range in the vicinity of the band gap is shown (aligned at VBM). For all three materials, Si, InP and CdSe the AEP results (blue crosses) are in very good agreement with the DFT results (red squares). Both methods capture the indirect nature of the band gap in Si QW, which results in the reduced LUMO/LUMO+1 energy offset in comparison with the direct band gap bulk materials. However, the LUMO/LUMO+1 states for Si QW are non-degenerate states due to intervalley coupling [132]. The errors between the DFT and the AEP results are given as bar chart in the lower part of the Fig. 4.11, showing that all errors are below 150 meV, which is more than satisfactory. The introduction of the weight factor  $w = 0.6$  for the doubly-passivated surface atoms (orange bars) in comparison with the absent weight factor (blue bars) does not improve the results significantly in this energy range.

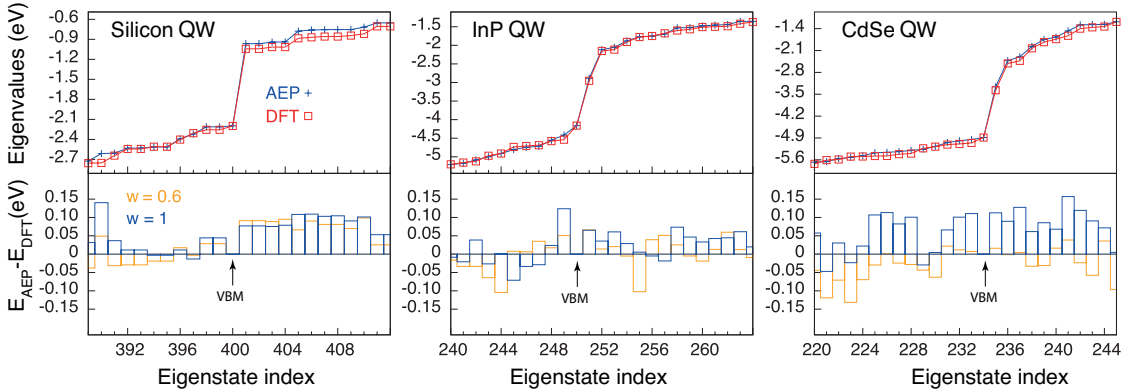


Figure 4.11: Top panels: Eigenvalues for Si, InP and CdSe QWs in the proximity of the band gap. Lower panels: bar charts showing the differences between DFT results and the AEP result including the weight strategy (orange) and the AEP result without weight (blue). Reprinted from [130].

### 4.3 Correction of the single-particle band gap

As mentioned in Section 2.2.1, the AEP approach inherits also the electron charge delocalization= from LDA [61] which leads to an underestimation of the single-particle band gap  $E_0$ . To empirically adjust the band gap to experimental values, the non-local part of the pseudopotential  $V^{\text{psp,nloc}}$  (Eq. (2.13)) should be considered:

$$V^{\text{psp,nloc}} = \sum_{lm} |\chi_{lm}^{KB}\rangle E_l^{KB} \langle \chi_{lm}^{KB} |, \text{ where} \quad (4.9)$$

$$E_l^{KB} = \frac{\langle u_l \delta V_l(\mathbf{r}) | \delta V_l(\mathbf{r}) u_l \rangle}{\langle u_l | \delta V_l(\mathbf{r}) | u_l \rangle} \text{ and } |\chi_{lm}^{KB}\rangle = \frac{|\delta V_l(\mathbf{r}) \psi_{lm}\rangle}{\langle u_l \delta V_l(\mathbf{r}) | \delta V_l(\mathbf{r}) u_l \rangle^{1/2}}.$$

Here  $\delta V_l(\mathbf{r})$  corresponds to the difference of the full pseudopotential  $V^{\text{psp}}$  and its local part  $V^{\text{psp,loc}}$ , the latter is also part of the AEPs. The  $u_l$  is the angular part of the atomistic pseudopotential wave function  $\psi_{lm}$ . For details see also Ref.[73].

The  $\delta V_l(\mathbf{r})$  can be modified in the following way, using the function:

$$\delta V_l(\mathbf{r}) = \delta V_l(\mathbf{r}) + \beta_l \left( 1 + \cos \frac{\pi r}{r_c} \right) \text{ for } r < r_c \quad . \quad (4.10)$$

The  $\beta_l$ -parameter is individually adjusted for every material and angular momentum  $l$  ( $l = 0$  corresponds to the so-called  $s$ -component,  $l = 1$  to the  $p$ -component and  $l = 2$  to the  $d$ -component of the pseudopotential) to fit the bulk band gap to the experimental value. The pseudopotential  $\delta V_l(\mathbf{r})$  is only modified within the cutoff radius  $r_c$  and left unchanged for larger  $r$  values. For most materials,  $r_c = 2.25$  Bohr was used.

#### 4.3.1 $\beta$ -correction influence on the bulk band structure and $e/h$ effective masses

The  $\beta$ -correction for Si bulk semiconductors is shown in Fig. 4.12. The Si pseudopotential was generated with  $V_d$ -components as a local part, thus  $\beta$ -correction can be applied to  $V_s$ - and  $V_p$ -components of the pseudopotential. One should keep in mind, that Si bulk is an indirect-gap material, so the experimental band gap corresponds to the transition between the  $\Gamma$  and the 0.86X  $\mathbf{k}$ -point. The introduced  $\beta$ -correction instigates a slight shift of the CBM from 0.86X to 0.83X  $\mathbf{k}$ -point.

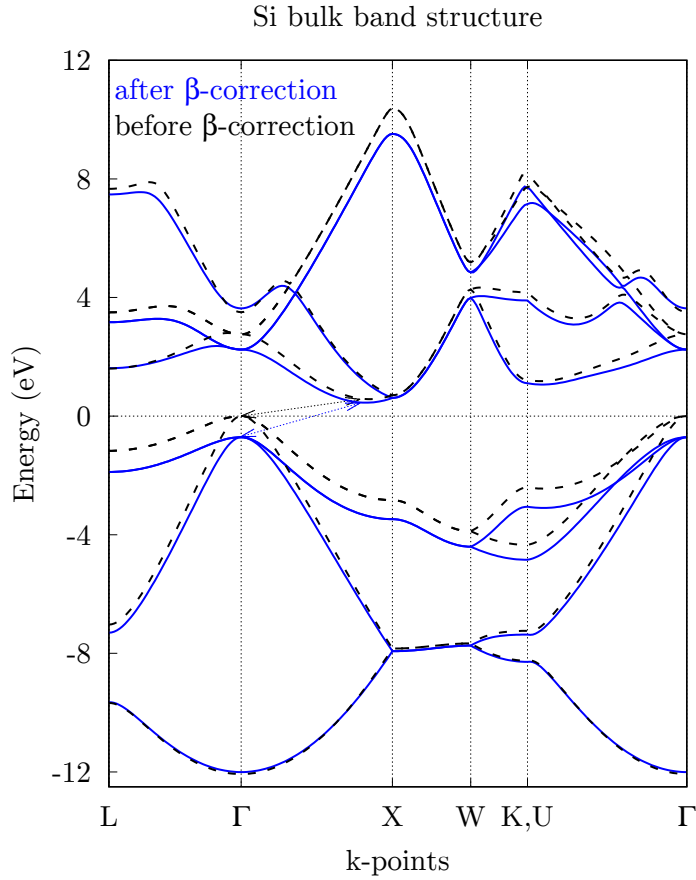


Figure 4.12: Band structure of the Si bulk (without SO coupling) before (black dashed) and after (blue solid)  $\beta$ -correction (see Eq. (4.10)). The chosen  $\beta$  values are specified in Table 4.6. The transition corresponding to the indirect band gap is shown schematically with arrows.

The band structure parameters versus different  $\beta_s$  and  $\beta_p$  values for Si bulk are shown in Fig. 4.13. Any pair of beta-parameters can be chosen along the band gap contour line (blue) to fulfill the band gap correction, therefore some additional band structure parameters such as  $\Gamma$ -X or  $\Gamma$ -L gap can be taken into account (the closer to additional contour lines - the better). It is clear that the perfect fit of all band structure parameters is not feasible, however, the final  $\beta$ -set is aimed to match the minimal deviations from experimental values as well as to choose minimal possible absolute values of the  $\beta$ -parameters.

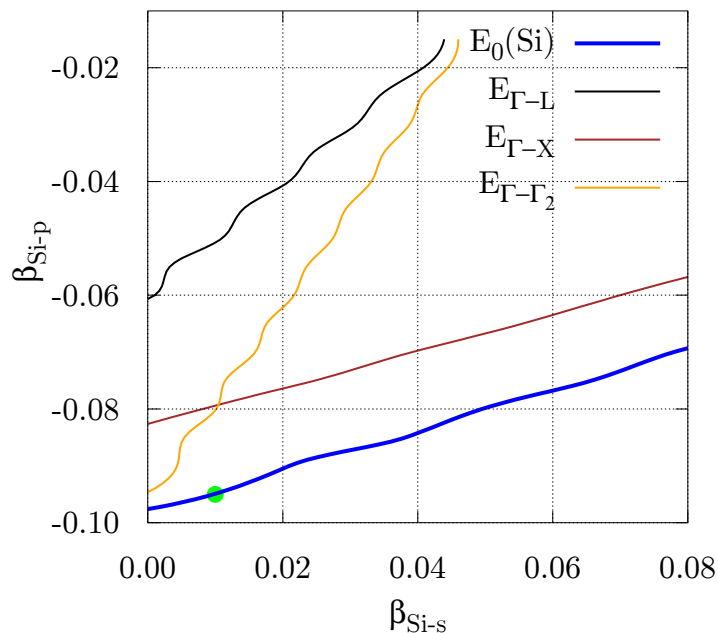


Figure 4.13: Contour lines show the match between calculated and experimentally measured band structure parameters for Si bulk [133], with respect to different  $\beta$ -values. The  $\beta$ -set, which was chosen for the further calculations, is marked by the green point.

$\beta$ -parameters indirectly influence on the effective mass of the electron and hole and also may alter SO band splitting (if implemented). The exact values for the band gap, SO splitting and  $e/h$  effective masses without and with chosen  $\beta$ -correction for Si bulk in comparison with experimental values are shown in Table 4.6. The same procedure for ZnS will be described in detail in Section 5.1. The electron effective mass  $m_e(\text{Si})$  is anisotropic for Si, and therefore is subdivided into a longitudinal ( $\mathbf{100}$ ) component and two ( $\mathbf{110}$ ) and ( $\mathbf{111}$ ) transverse components. For Si, the CBM is mostly formed by the  $V_s$ -component of the pseudopotential, and the VBM is mostly formed by the  $V_p$ -component, that is why mostly the shift of the VBM is observed for chosen  $\beta$ -set in Fig. 4.13.

Si bulk	$E_0$	$\Delta\text{SO}$	$m_{e,l}$	$m_{e,t}$	$m_{hh}$	$m_{lh}$
no $\beta$ -correction	0.56 eV	51 meV	0.90	0.19	0.28	0.20
$\beta_s = 0.01, \beta_p = -0.095$	1.12 eV	54 meV	0.99	0.22	0.30	0.25
experimental values	1.12 eV	44 meV	0.98	0.19	0.46	0.16

Table 4.6: Band gap,  $e$  (at the CBM) and  $h$  (at the VBM) effective mass values for Si bulk semiconductor with and without  $\beta$ -correction in comparison with experimental values [133]. In case of Si, the same  $\beta$ -set is used with and without SO coupling.

The experimental band structure parameters are taken from Ref. [133]. Due to the method restrictions, it is impossible to correct all band structure parameters and effective masses simultaneously. To match the optical absorption experiments, the band gap value at room temperature ( $300K$ ) is used as the main target value for the  $\beta$ -correction. In case of significant deviations for the semiconductor band structure at room temperature and at  $0K$ ,  $\beta$ -parameters set for ideal  $e/h$  effective mass or for experimental band gap at  $0K$  temperature can be chosen differently, depending on the purposes of the following calculations and experimental benchmarks. Although this does not apply to Si, sometimes different  $\beta$ -sets are required depending on whether the SO interactions are considered in the calculation.

### 4.3.2 $\beta$ -correction for the band offsets in core-shell QDs

The  $\beta$ -correction is mostly used to match the experimental band gaps. For core-shell systems, however, it is also important to preserve the correct band offset between core and shell material, which influences the optical properties of the core-shell NCs. The band structures around the band gap without and with  $\beta$ -correction are shown in Fig. 4.14.

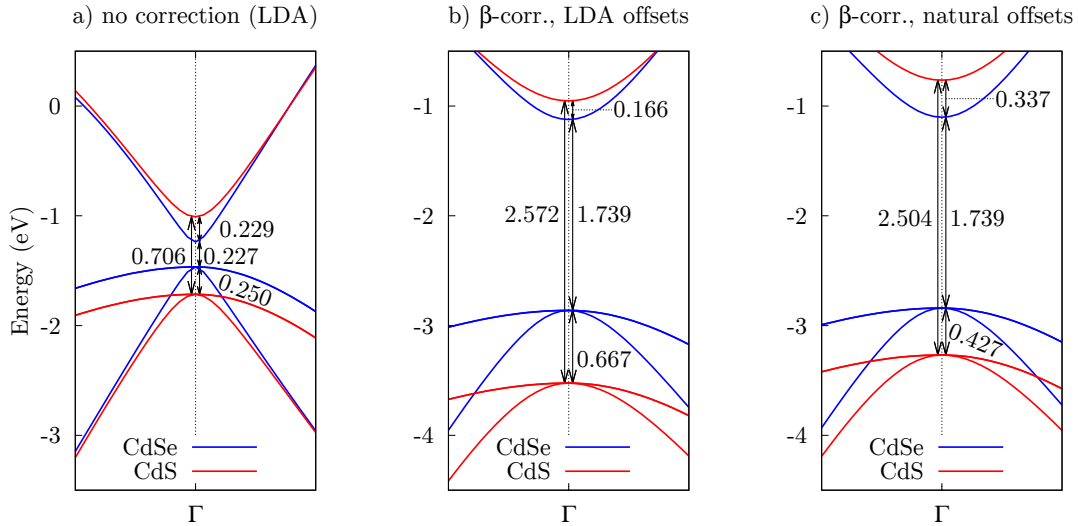


Figure 4.14: Band gaps and band offsets around the  $\Gamma$ -point for ZB CdSe/CdS, aligned at the Cd  $d$ -bands (no SO coupling): a) without  $\beta$ -correction b) with  $\beta$ -correction fitted to the experimental  $E_0$ , but preserving the LDA band offsets c)  $\beta$ -correction to ideal  $E_0$  and to natural band offsets.

The difficulty in calculating the band offset lies in finding a common reference that would determine the relative band alignment between the two materials [134].

However, for the structures with common cations, for example, CdSe/CdS, in which the  $V_d$ -components of the cation pseudopotentials are the same, it is possible to align the  $d$ -bands in the CdSe and CdS bulk band structures in order to obtain the relative offset.

The reference values for the LDA and natural band offsets measured experimentally were taken from Ref. [120, 134, 135, 136]. The  $\beta$ -correction parameters for CdSe and CdS in the calculations with and without SO coupling are different and therefore specified explicitly in Table 4.7 together with the corresponding material offsets. One should keep in mind that for ZB and WZ binary materials, the CBM is mostly formed by the non-local  $V_s$ -component of the cation (Cd) pseudopotential ( $\beta_{s,c}$ ), and the VBM is mostly formed by the non-local  $V_p$ -component of the anion (Se or S) pseudopotential ( $\beta_{p,a}$ ).

	$E_0$ (CdSe)	$E_0$ (CdS)	VBM offset	CBM offset
no correction	0.227 eV	0.706 eV	0.250 eV	0.229 eV
without SO coupling, LDA $\beta_{s,c}^{CdSe} = 0.050, \beta_{p,a}^{CdSe} = -0.175$ $\beta_{s,c}^{CdS} = 0.025, \beta_{p,a}^{CdS} = -0.180$	1.739 eV	2.572 eV	0.667 eV	0.166 eV
without SO coupling, Natural $\beta_{s,c}^{CdSe} = 0.050, \beta_{p,a}^{CdSe} = -0.175$ $\beta_{s,c}^{CdS} = 0.115, \beta_{p,a}^{CdS} = -0.155$	1.739 eV	2.504 eV	0.427 eV	0.337 eV
with SO coupling, LDA $\beta_{s,c}^{CdSe} = 0.200, \beta_{p,a}^{CdSe} = -0.155$ $\beta_{s,c}^{CdS} = 0.200, \beta_{p,a}^{CdS} = -0.145$	1.732 eV	2.535 eV	0.605 eV	0.198 eV
with SO coupling, Natural $\beta_{s,c}^{CdSe} = 0.080, \beta_{p,a}^{CdSe} = -0.190$ $\beta_{s,c}^{CdS} = 0.080, \beta_{p,a}^{CdS} = -0.160$	1.778 eV	2.465 eV	0.475 eV	0.212 eV
reference values				
Experimental values, Ref.[120]	1.732 eV	2.482 eV	–	–
LDA-offsets, Ref.[136]	–	–	0.61 eV	0.29 eV
Natural offsets, Ref.[134]	–	–	0.35 eV	0.34 eV
Natural offsets, Ref.[135]	1.76 eV	2.50 eV	0.42 eV	0.32 eV

Table 4.7: Band gap and HOMO/LUMO offsets for CdSe and CdS bulk semiconductor with and without SO-coupling in comparison with the reference values. The  $\beta$ -correction sets for LDA and natural offsets are specified.

### 4.3.3 $\beta$ -correction influence on the wave functions

Wave functions projections before and after  $\beta$ -correction are considered (see Eq. (2.7)), to check the influence of the  $\beta$ -parameters on the atomistic wave functions:

$$\langle \psi_i^{\text{AEP}+\beta} | \psi_i^{\text{AEP}} \rangle \leq 1 \quad . \quad (4.11)$$

The closer is the result of projection to 1.0, the more wave functions are similar to each other (1.0 would mean identical). The wave function projections from Eq. (4.11) for Si QD with  $R=7.5 \text{ \AA}$  are shown in Fig. 4.15. An excellent agreement between the wave functions before and after  $\beta$ -correction is observed. This result was expected, because  $\beta$ -correction does not affect any of the basic criteria for the norm-conserving pseudopotentials [137].

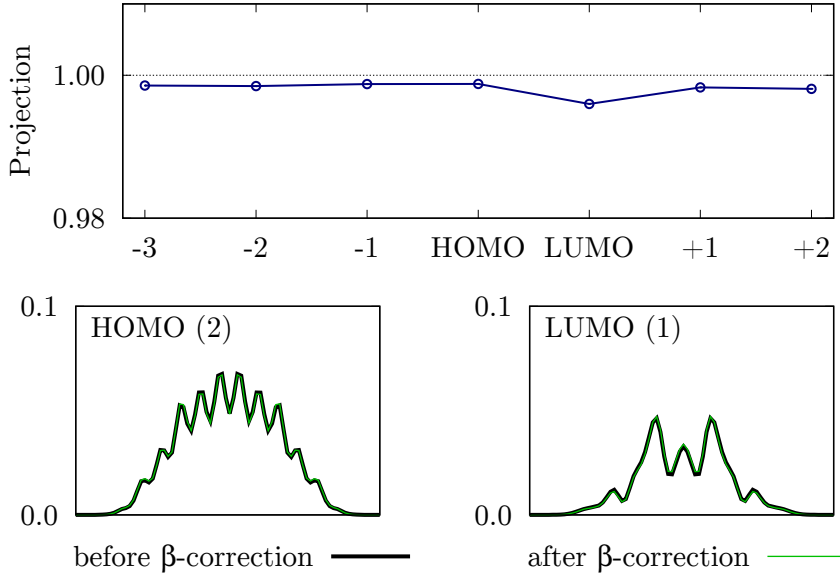


Figure 4.15: Results for the Si QD with  $R=7.5 \text{ \AA}$ . Upper panel: the wave function projections of states near band gap, calculated as described in Eq. (4.11). Lower panel: HOMO and LUMO wave functions before (black) and after (green)  $\beta$ -correction are given explicitly in one-dimension across the QD.

Similar check was done for the  $\beta$ -correction for CdSe/CdS core-shell QD with a core radius  $R=12 \text{ \AA}$  and a shell thickness of  $16.5 \text{ \AA}$ , both for the LDA and natural band offsets. The results are shown in Fig. 4.16.

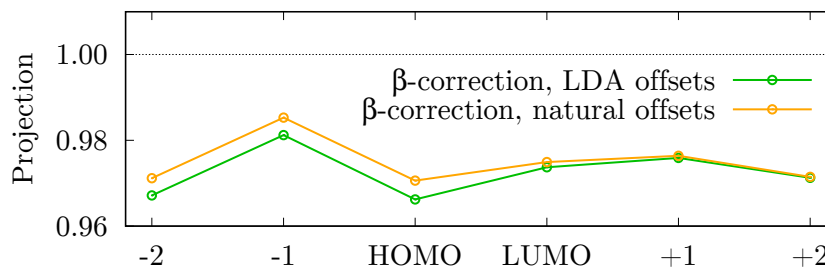


Figure 4.16: The wave function projections of states near band gap for the CdSe/CdS QD with a core radius of 12 Å and a shell thickness of 16.5 Å, calculated as described in Eq. (4.11). The  $\beta$ -sets for SO coupling included for LDA (green) and natural (orange) band offsets are considered.

From Fig. 4.15 and Fig. 4.16 it can be concluded, that the correction scheme does not have any considerable influence on the wave function confinement or distribution. In case of the core-shell QD, even so the projections are not as close to 1 as in case of one-compound nanostructures due to change of the offsets,  $\beta$ -correction still has minimal influence on the wave function shape and distribution.  $\beta$ -set for the QD with natural band offsets returns the wave function projections in VB slightly closer to 1. The role of the band offsets between CdSe and CdS materials will be further investigated in Section 5.4.

#### 4.4 Dielectric screening function for colloidal QDs

The optical properties of colloidal QDs are also affected by the embedding environment [116]. The influence of the solvent and surface passivation on their optical properties is important to consider. Dielectric screening is frequency-dependent and can be subdivided in a high-frequency ( $\epsilon_\infty$ ) and a low-frequency ( $\epsilon_0$ ) response. The optical properties are dominated by the fast electronic response to the charge, which is given by  $\epsilon_\infty$ . The additional ionic response is much slower and contained in  $\epsilon_0$  [138]. Not all of the ionic responses can screen the optical excitation, e.g, solvent reorganization is too slow to screen a typical optical excitation and should not be taken into account in the screening constant  $\epsilon_{\text{out}}$  [86]. Haken [118] has developed a model that describes the part of the ionic response for semiconductors  $\epsilon_{\text{in},0}$  that is fast enough to screen optical excitations. This contribution is called ionic screening (see Section 4.4.2).

#### 4.4.1 Constant screening

The simplest way to model dielectric screening is to use a constant screening  $\epsilon_{\text{in},\infty} = \text{const}$ , in which case the diagonal direct Coulomb integral  $J_{i,j}^{\text{const}}$  can be written within the single-configuration (SC) approximation as:

$$J_{i,j}^{\text{const}} = \frac{1}{\epsilon_{\text{in},\infty}} \sum_{\sigma_1, \sigma_2} \int \int \frac{|\psi_i(\mathbf{r}_1, \sigma_1)|^2 |\psi_j(\mathbf{r}_2, \sigma_2)|^2}{|\mathbf{r}_1 - \mathbf{r}_2|} d\mathbf{r}_1 d\mathbf{r}_2. \quad (4.12)$$

#### 4.4.2 Microscopic screening

A more advanced screening model uses a microscopic description,  $\epsilon(|\mathbf{r}_1 - \mathbf{r}_2|)$ . In the framework of the Thomas-Fermi model, Resta [117] proposed a microscopic dielectric screening model that depends on the Thomas-Fermi wave vector  $q$  and the screening radius  $\rho_\infty$ :

$$J_{i,j}^{\text{micro}} = \sum_{\sigma_1, \sigma_2} \int \int \frac{|\psi_i(\mathbf{r}_1, \sigma_1)|^2 |\psi_j(\mathbf{r}_2, \sigma_2)|^2}{\epsilon(|\mathbf{r}_1 - \mathbf{r}_2|) |\mathbf{r}_1 - \mathbf{r}_2|} d\mathbf{r}_1 d\mathbf{r}_2, \quad (4.13)$$

with  $\epsilon(|\mathbf{r}_1 - \mathbf{r}_2|) =$

$$\begin{cases} \frac{\epsilon_{\text{in},\infty} q \rho_\infty}{\sinh[q(\rho_\infty - |\mathbf{r}_1 - \mathbf{r}_2|)] + q|\mathbf{r}_1 - \mathbf{r}_2|} & \text{if } |\mathbf{r}_1 - \mathbf{r}_2| < \rho_\infty \\ \epsilon_{\text{in},\infty} & \text{if } |\mathbf{r}_1 - \mathbf{r}_2| \geq \rho_\infty \end{cases}.$$

The microscopic screening function tends to 1 (unscreened interaction) when  $\mathbf{r}_1 \rightarrow \mathbf{r}_2$  and tends to  $\epsilon_{\text{in},\infty}$  when  $|\mathbf{r}_1 - \mathbf{r}_2|$  is beyond the screening radius  $\rho_\infty$ .

The contribution of the ionic part of the dielectric screening function  $\epsilon_{\text{ionic}}(|\mathbf{r}_1 - \mathbf{r}_2|)$  can be also included in the microscopic screening term, using the polaronic model of Haken[118]:

$$\frac{1}{\epsilon_{\text{ionic}}(|\mathbf{r}_1 - \mathbf{r}_2|)} = \left[ \frac{1}{\epsilon_{\text{in},0}} - \frac{1}{\epsilon_{\text{in},\infty}} \right] \times \left[ 1 - \frac{e^{-|\mathbf{r}_1 - \mathbf{r}_2|/\rho_h} + e^{-|\mathbf{r}_1 - \mathbf{r}_2|/\rho_e}}{2} \right]. \quad (4.14)$$

Here  $\rho_{e,h} = \sqrt{1/2m_{e,h}\omega_{LO}}$ , where  $m_{e,h}$  stands for electron and hole effective mass, correspondingly, and  $\omega_{LO}$  is a frequency LO-phonon mode of the bulk material. As the radius of QD becomes small compared to  $\rho_e$  and  $\rho_h$ , the relative importance of ionic screening decreases [91].

The lack of explicit dependence of the microscopic screening on  $\mathbf{r}$ , but only on  $|\mathbf{r}_1 - \mathbf{r}_2|$ , allows calculating the Coulomb and exchange integrals in reciprocal space, which is computationally very advantageous [86]. After Fourier transform the  $\epsilon(|\mathbf{r}_1 - \mathbf{r}_2|)$  (Eq. (4.13)) is turned into:

$$\epsilon(k) = \frac{k^2 + q^2}{k^2 + q^2 \sin(k\rho_\infty)/(\epsilon_{\text{in},\infty} k\rho_\infty)} \quad , \quad (4.15)$$

and, correspondingly, the contribution from ionic part  $\epsilon_{\text{ionic}}(|\mathbf{r}_1 - \mathbf{r}_2|)$  from (Eq. (4.14)) can be written as:

$$\epsilon_{\text{ionic}}(k) = \left[ \frac{1}{\epsilon_{\text{in},0}} - \frac{1}{\epsilon_{\text{in},\infty}} \right] \times \left[ \frac{1/2}{1 + \rho_h^2 k^2} + \frac{1/2}{1 + \rho_e^2 k^2} \right] \quad (4.16)$$

(see Ref.[72] for details).

#### 4.4.3 Modified Penn model for $\epsilon_{\text{in}}$

Based on the ideas developed by Penn [119] that the dielectric constant can be related to the band gap of the material, a modified Penn model was developed for QDs[72, 91]. The increased band gap of the QD, compared to the constituting bulk semiconductor material gap, leads to a reduced dielectric constant [72, 91]:

$$\begin{aligned} \epsilon_{\text{in},\infty}^{\text{QD}}(R) &= 1 + (\epsilon_{\text{in},\infty}^{\text{bulk}} - 1) \frac{[E_0^{\text{bulk}} + \Delta E^{\text{bulk}}]^2}{[E_0^{\text{QD}} + \Delta E^{\text{bulk}}]^2} \quad , \quad (4.17) \\ \epsilon_{\text{in},0}^{\text{QD}}(R) &= \epsilon_{\text{in},\infty}^{\text{QD}}(R) + (\epsilon_{\text{in},0}^{\text{bulk}} - \epsilon_{\text{in},\infty}^{\text{bulk}}) \quad , \end{aligned}$$

where  $E_0^{\text{bulk}}$  and  $E_0^{\text{QD}}$  are the single-particle bulk and QD band gaps, respectively, and  $\Delta E^{\text{bulk}}$  denotes the difference between so-called  $E_2$  and  $E_0$  transitions in bulk [5].  $E_2$  is the transition with strongest absorption in a semiconductor with tetrahedral crystal structure (4.87 eV for InP and 6.07 eV for CdSe) [120].

The radius-dependent  $\epsilon_{\text{in},\infty}^{\text{QD}}$  along with the bulk value  $\epsilon_{\text{in},\infty}^{\text{bulk}}$  are shown in Fig. 4.17. The radius-dependent  $\epsilon_{\text{in},0}^{\text{QD}}$  is only used to calculate ionic contribution in the polaronic Haken model (see Eq. (4.14)). The modified Penn model in particular and the radius-dependent dielectric screening for QDs in general are still actively used [139, 140, 141, 142, 143].

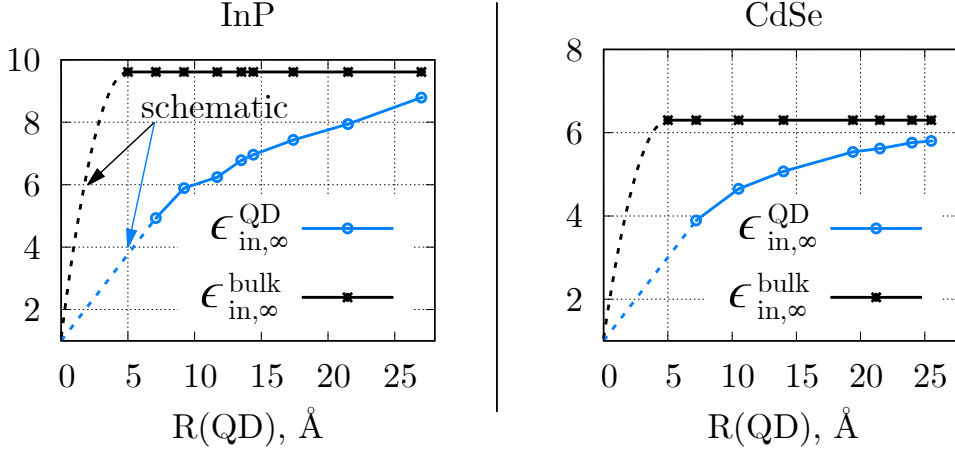


Figure 4.17: Radius-dependent  $\epsilon_{in,\infty}^{QD}$  calculated with the modified Penn model (blue) in comparison with the  $\epsilon_{in,\infty}^{bulk}$  dielectric screening (black) for InP (left panel) and CdSe (right panel) QDs. See Eq. (4.17) for details.

#### 4.4.4 Macroscopic screening

In the macroscopic screening model, the boundary between the QD and the surrounding medium is described by a dielectric function  $\epsilon(\mathbf{r})$  that changes smoothly from  $\epsilon_{in,\infty}$  to  $\epsilon_{out}$  at the QD surface. The transition region has a width in the range of the inter-atomic bond length [92, 91]. In this case, the Coulomb and exchange integrals are calculated by solving the Poisson equation in real space:

$$\begin{aligned} \nabla\epsilon(\mathbf{r})\nabla\Phi_j(\mathbf{r}) &= -4\pi\rho_j(\mathbf{r}), \\ \text{where } \rho_j(\mathbf{r}) &= \sum_{\sigma} |\psi_j(\mathbf{r}, \sigma)|^2, \end{aligned} \quad (4.18)$$

with the electrostatic potential  $\Phi_j(\mathbf{r})$  and the charge density  $\rho_j(\mathbf{r})$ . The direct Coulomb integrals  $J_{i,j}^{macro}$  are obtained from:

$$J_{i,j}^{macro} = \sum_{\sigma} \int |\psi_i(\mathbf{r}, \sigma)|^2 \Phi_j(\mathbf{r}) d\mathbf{r}. \quad (4.19)$$

This term can be written as the sum of a constant screening term  $J_{i,j}^{const}$  (see Eq. (4.12)) and a polarization term  $J_{i,j}^{pol}$ , which accounts for the effects of the dielectric mismatch between the QD and the surrounding material (solvent):

$$J_{i,j}^{macro} = J_{i,j}^{const} + J_{i,j}^{pol}. \quad (4.20)$$

To model the real space dependence of the macroscopic  $\epsilon(\mathbf{r})$  in Eq.(4.18), the function  $m(\mathbf{r})$  [93, 144] is introduced:

$$m(\mathbf{r}) = \frac{1}{1 + \exp[(|\mathbf{r}| - R)/w_0]} \quad , \quad (4.21)$$

where  $|\mathbf{r}|$  is the distance from the center of the QD and  $R$  is the radius of the QD (including atomistic passivants). The constant  $w_0$  determines the width of the transition region and is given as  $0.163a_0$  (as suggested in Ref. [93]), where  $a_0$  is the bulk lattice constant of the semiconductor. Note that the same width of the transition region is used for the polarization term in Eq. (2.30). The resulting dielectric function  $\epsilon(\mathbf{r})$  is:

$$\epsilon(\mathbf{r}) = \epsilon_{\text{out}} + m(\mathbf{r})(\epsilon_{\text{in}} - \epsilon_{\text{out}}) \quad . \quad (4.22)$$

A graphical representation of the macroscopic screening  $\epsilon(\mathbf{r})$  is shown in Fig. 4.18) for a CdSe QD with radius 14 Å.

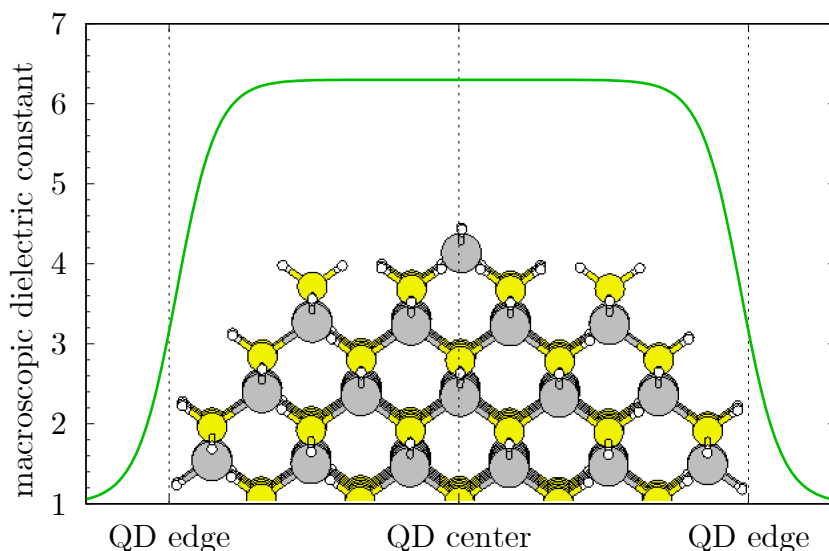


Figure 4.18: Graphical representation of the macroscopic dielectric screening, calculated according to Eq. (4.22) for the CdSe QD with  $R=14$  Å in vacuum ( $\epsilon_{\text{out}} = 1$ ).

To obtain the total Coulomb interaction term, the microscopic contribution have to be added, which is lacking in the Poisson equation solution from Eq. (4.18):

$$J_{i,j}^{\text{total}} = J_{i,j}^{\text{macro}} + (J_{i,j}^{\text{micro}} - J_{i,j}^{\text{const}}) \quad . \quad (4.23)$$

$J_{i,j}^{\text{const}}$  has to be subtracted from  $J_{i,j}^{\text{micro}}$  as it is already included in both the  $J_{i,j}^{\text{micro}}$  and the  $J_{i,j}^{\text{macro}}$  terms. Fig. 4.19 shows a schematic representation of the screening from Eq. (4.23).

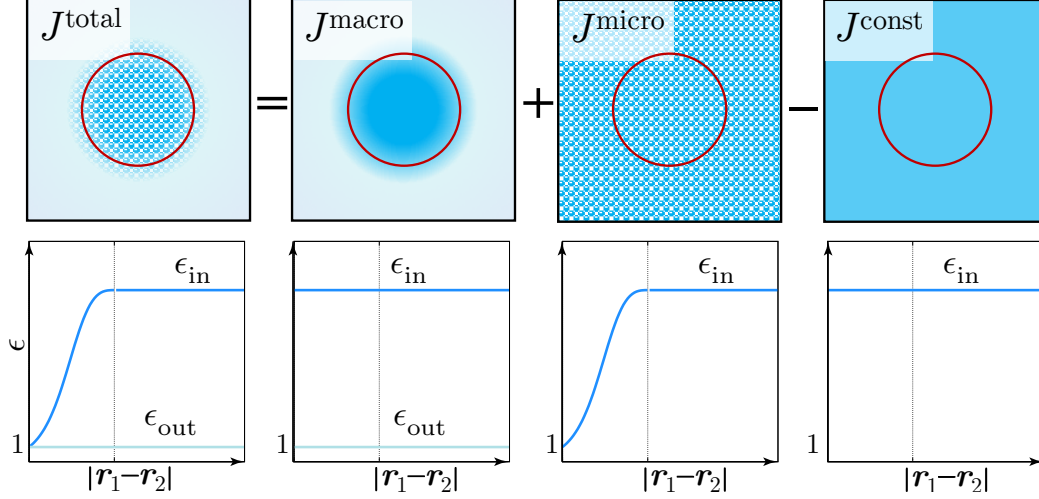


Figure 4.19: Top panels: schematic representation of the different screening types and corresponding Coulomb interactions terms. The solid color fill represents the macroscopic  $\epsilon(r)$  (the gradient from dark-blue to light-blue corresponds to the transition between  $\epsilon_{\text{in}}$  and  $\epsilon_{\text{out}}$ ), the pattern fill represents schematically the microscopic screening  $\epsilon(|\mathbf{r}_1 - \mathbf{r}_2|)$ . Bottom panels: Dielectric function as a function of the distance between two integration points. Reprinted from [94].

#### 4.4.5 Macroscopic screening in reciprocal space and its restrictions

Since real-space calculations of the electrostatic potential (see Eq. (4.18)) lead to relatively long computational times, an effort to calculate Coulomb terms  $J_{i,j}^{\text{total}}$  (see Eq. (4.23)) fully in reciprocal space was made by substituting the radius-dependent dielectric screening function  $\epsilon(\mathbf{r})$  from Eq. (4.22) directly into the microscopic screening model (Eq. (4.13)):

$$\begin{aligned}
 J_{i,j}^{\text{total,gs}} = & \quad (4.24) \\
 \sum_{\sigma_1, \sigma_2} \int \int & \frac{1}{|\mathbf{r}_1 - \mathbf{r}_2|} \left[ \frac{|\psi_i(\mathbf{r}_1, \sigma_1)|^2 |\psi_j(\mathbf{r}_2, \sigma_2)|^2}{\epsilon_{\text{out}}(|\mathbf{r}_1 - \mathbf{r}_2|)} + \right. \\
 & + \frac{|\psi_i(\mathbf{r}_1, \sigma_1)|^2 |\psi_j(\mathbf{r}_2, \sigma_2)|^2 m(\mathbf{r}_1) m(\mathbf{r}_2)}{\epsilon_{\text{in}}(|\mathbf{r}_1 - \mathbf{r}_2|)} - \\
 & \left. - \frac{|\psi_i(\mathbf{r}_1, \sigma_1)|^2 |\psi_j(\mathbf{r}_2, \sigma_2)|^2 m(\mathbf{r}_1) m(\mathbf{r}_2)}{\epsilon_{\text{out}}(|\mathbf{r}_1 - \mathbf{r}_2|)} \right] d\mathbf{r}_1 d\mathbf{r}_2 \quad .
 \end{aligned}$$

The transformation of the  $R$ -dependent function  $m(\mathbf{r})$  into reciprocal space is quite complicated because in fact there is no dielectric boundary between the QD and surrounding medium in the reciprocal space. At the same time, it is non-trivial task to map distance-dependent microscopic screening  $\epsilon(|\mathbf{r}_1 - \mathbf{r}_2|)$  (Eq. (4.13)) in the real space. However, from Eq. (4.24) it follows, that the radius-dependent function  $m(\mathbf{r})$  could be applied not only to the dielectric function  $\epsilon$  but also to the wave functions  $\psi_i$ . In this case, “screened” wave functions will replace initial ones in real space and will be later Fourier-transformed to the reciprocal space, and Eq. (4.21) might be re-written as:

$$m_{\psi_i}(\mathbf{r}) = \frac{1}{1 + \exp((|\mathbf{r}| - R_{\psi_i})/w_0)} \quad . \quad (4.25)$$

In Eq. (4.25) the  $R_{\psi_i}$  is the radius of the individual wave function, which is defined by quantum confinement and therefore indirectly also by QD radius. However, the radius of the wave function confinement  $R_{\psi_i}$  tends to scale differently than QD radius  $R$ , and it depends on the wave functions individually, whereas QD radius  $R$  is an averaged value. All wave functions obtained from ground state calculations are orthonormal by definition (Eq. (2.7)). After applying Eq. (4.25), though, wave functions will be not normalized anymore:

$$\int m_{\psi_i}(\mathbf{r})\psi_i^*(\mathbf{r})\psi_i(\mathbf{r})d^3\mathbf{r} = norm < 1 \quad . \quad (4.26)$$

The *norm* of the wave function is an individual parameter which can be used as a criteria for the  $R_{\psi_i}$  choice. It is possible to fix the *norm* parameter in Eq. (4.26) that way, that the final result for the  $J_{i,j}^{\text{total,gs}}$  from Eq. (4.24) will coincide with the  $J_{i,j}^{\text{total}}$  from Eq. (4.23). The necessity of the  $m(\mathbf{r})$  to  $m_{\psi_i}(\mathbf{r})$  modification is demonstrated for the Si QD ( $R = 16.7\text{\AA}$ ) in Fig. 4.20. The final result is obtained with *norm* = 0.6.

The *norm* value is highly transferable for different sizes and materials. To estimate the possible consequences after the “denormalization” of the wave functions, several tests were performed. First of all, the influence on the electron self-polarization term  $\sum_e^{\text{pol}}$  (Eq. (2.29), the radius for polarization potential  $V_s$  is the radius of QD in both cases) is shown in Fig. 4.21.

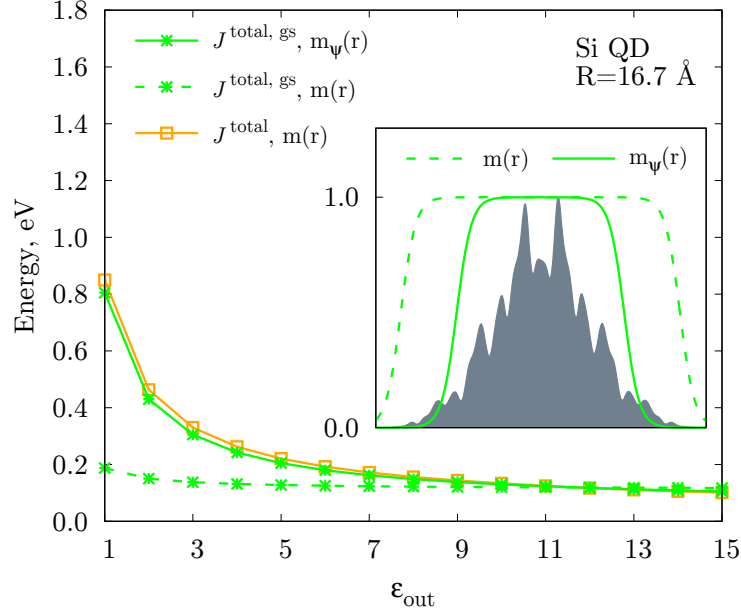


Figure 4.20: Graphical representation of the  $J^{\text{total}}$  (Eq. (4.23)) and  $J^{\text{total,gs}}$  (Eq. (4.24)) in SC for the Si QD with  $R=16.7 \text{ \AA}$ . Inset: corresponding one-dimensional LUMO wave function and its spatial relation to the radius-dependent functions  $m(\mathbf{r})$  (see Eq. (4.22)) and  $m_{\psi_i}(\mathbf{r})$  (see Eq. (4.25)).

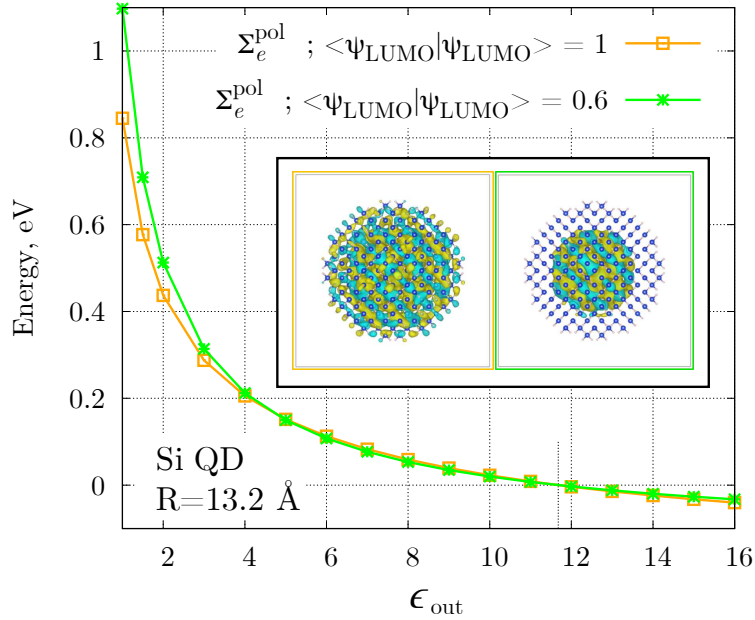


Figure 4.21: Influence of the reduced *norm* value of the LUMO wave function of the Si QD with  $R=13.2 \text{ \AA}$  on the electron self-polarization term  $\Sigma_e^{\text{pol}}$  with respect to  $\epsilon_{\text{out}}$  (see Eq. (2.29)). Inset: Corresponding three-dimensional isosurface of the LUMO wave function before (orange frame) and after (green frame) *norm* reduction (Eq. (4.26)).

In Fig. 4.21 a noticeable increase of the self-polarisation term in case of reduced  $norm$  value can be observed for low  $\epsilon_{out}$ , which most probably happens because of the clearly confined wave function and charge localization relatively far from the QD dielectric border. This effect might vanish in case of large QDs, where the wave functions are initially well-confined inside the NC. Similar effect is observed for the  $\sum_h^{pol}$ , and thus not shown explicitly.

The orthogonality of the wave functions (Eq. (2.7)) after the “denormalization” was investigated additionally, and the results for CdSe QD with  $R = 14.0 \text{ \AA}$  are shown in Fig. 4.22. It is demonstrated that some of the wave functions loose also orthogonality after  $norm$  value reduction, which leads to over-ranging of the exciton DB splitting (see Section 2.5.1 for details), especially for the  $\epsilon_{out}$  close to 1, and some other undesirable consequences such as abnormally high correlation effects. Therefore, the idea of the full reciprocal-space screening model requires further research and will not be considered in the next sections.

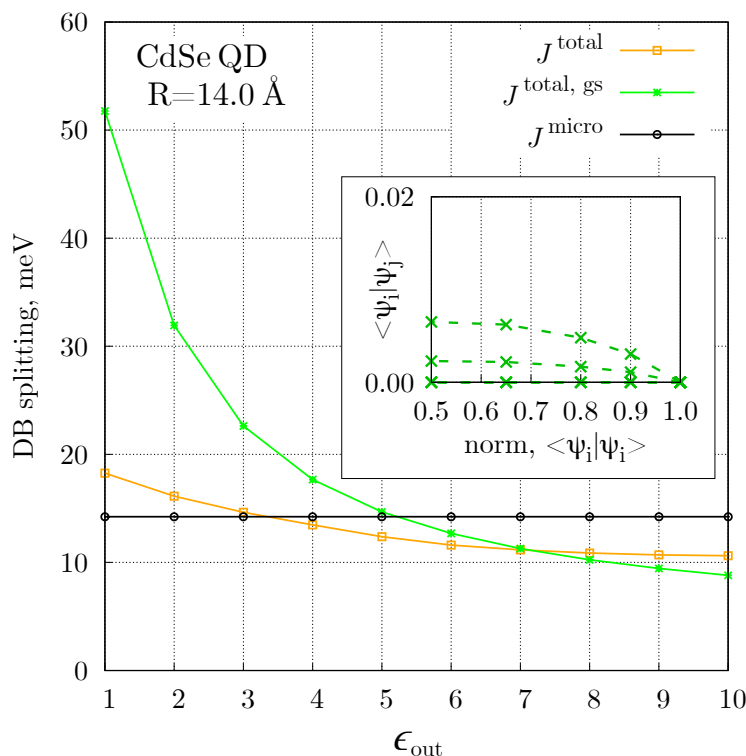


Figure 4.22: Exciton dark-bright splitting of the ZB CdSe QD with  $R=14.0 \text{ \AA}$  with respect to the  $\epsilon_{out}$ . Solvent-independent model  $J^{micro}$  is compared with state-of-art solvent-dependent model  $J^{total}$  and full reciprocal space model  $J^{total,gs}$ , where value of norm 0.6 is used. Inset: change of the orthogonality with respect to the  $norm$  value for wave functions within a 6-6 basis set (6 electron and 6 hole wave functions around the band gap were considered in CI).



## Chapter 5

# Results and discussion

### 5.1 Optical transitions in ZnS 2D nanoplatelets

The band structure for ZnS bulk (WZ) with  $\beta$ -correction and SO-coupling is shown in Fig. 5.1.

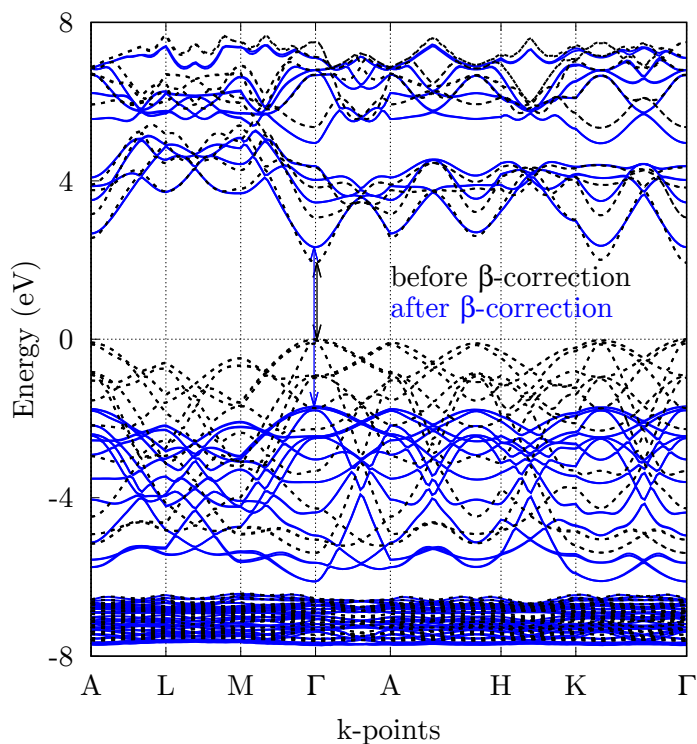


Figure 5.1: Band structure of the WZ ZnS bulk (with SO coupling) before (black dashed) and after (blue solid)  $\beta$ -correction (see Eq. (4.10)). The band structure parameters are specified in Table 5.1. The transition corresponding to the band gap at  $\Gamma$ -point is shown schematically with arrows.

In Fig. 5.1 the Zn bands at the relatively deep energies are formed entirely by  $d$ -component of the pseudopotential), which is not affected by the  $\beta$ -correction. ZnS is a direct-gap semiconductor and belongs to large-gap materials, therefore quite significant  $\beta$ -correction is implemented to fit the experimental results. Band structure parameters for chosen  $\beta$ -set are specified in Table 5.1 and initially were fitted to ZnS bulk GW band gap ([145]. The experimental values at room temperature are taken from Ref.[145, 146].

ZnS bulk (WZ)	$E_0$	$\Delta\text{CF}$	$\Delta\text{SO}$	$m_{e,l}$	$m_{e,t}$	$m_{h,l}$	$m_{h,t}$
no $\beta$ -correction	1.93 eV	33 meV	75 meV	0.16	0.17	1.49	0.50
$\beta_{s,c}^{\text{ZnS}} = 0.14$ $\beta_{p,a}^{\text{ZnS}} = -0.164$	4.02 eV	35 meV	59 meV	0.34	0.37	1.83	0.77
experimental values	3.90 eV	29 meV	92 meV	0.28	–	1.40	0.49

Table 5.1: Band gap and  $e/h$  effective mass values for ZnS bulk semiconductor with and without  $\beta$ -correction in comparison with experimental values [145, 146].  $\beta_{s,c}$  corresponds to the  $V_s$ -component of the cation (Zn) pseudopotential, and  $\beta_{p,a}$  affects the  $V_p$ -component of the anion (S) pseudopotential. Both electron and hole (A-band) effective masses  $m_{e,h}$  are anisotropic and consist of the longitudinal (**100**) and transverse (**010**), (**120**) components.

The AEP-based calculations with  $\beta$ -correction and SO-coupling of the ZnS WZ slab with 1.91 nm thickness along [**1120**] (or [**110**]) growth direction and pseudo-hydrogen surface passivation were performed in order to predict the ground state band structure, simulate the dipole transitions and explain the absorption spectra features of the ZnS 2D nanoplatelets (NPLs) with  $1.81 \pm 0.2$  nm thickness along [**1120**] growth direction, observed in the experiment [147]. The absorption spectrum was modeled by calculation of the dipole transitions matrix elements within SC approximation (see Section 2.4). Temperature-dependent broadening of the dipole transitions was implemented in agreement with Ref.[148]. The calculated and experimental absorption spectra along with single-particle eigenvalues and eigenfunctions of the relevant near-band-gap states are shown in Fig. 5.2.

In the experiment, the appearance of several absorption features in the absorption spectra of colloidal CdSe NPLs, and generally in 2D systems, was attributed to electronic transitions from h0 (heavy-hole (hh) in ZB or A-band in WZ), h1 (light-hole (lh) in ZB or B-band in WZ), and h2 (spin-orbit (SO) in ZB or C-band in WZ) valence bands to the e0 (CBM) [20], as well as inter-band transitions from lower valence to higher conduction bands [149]. From the theoretical simulation of the dipole transitions using  $\Gamma$ -point wave functions, it can be concluded that the first absorption peak for WZ ZnS NPLs corresponds to a sum of three transitions, namely, from the h0, h1, and h2 nodeless states derived from the A-, B-, and C-bulk valence bands to the e0 nodeless state (CBM). The observed first absorption peak

is dominated by the third valence band state ( $h_2$ ), which has an offset from the  $h_0$  (VBM) less than 100 meV. The dominance of the  $h_2$  state in the absorption peak obviously contributes to the considerable Stokes shift observed.

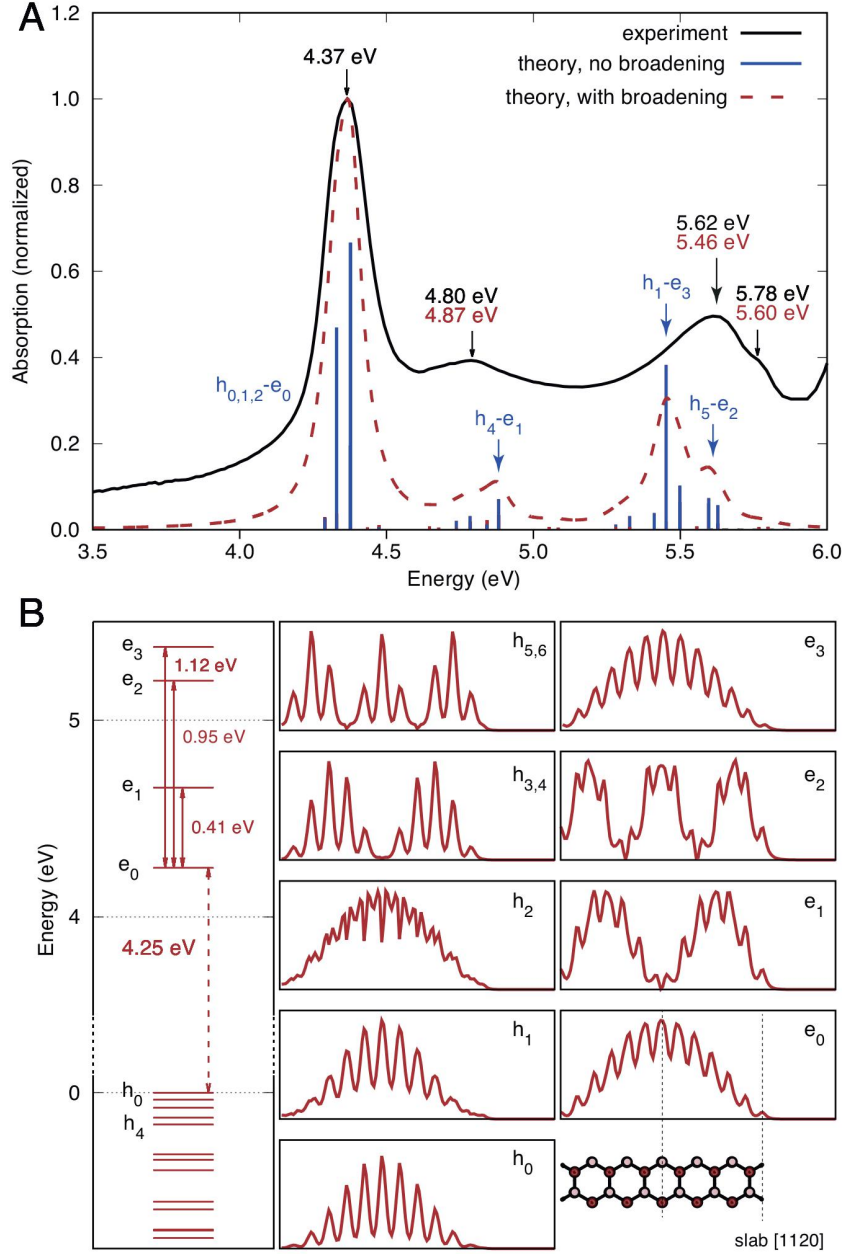


Figure 5.2: (A) Normalized absorption spectrum (black) of ZnS WZ NPLs after subtraction of a scattering background along with calculated dipole transitions (red dashed). The first exciton energy was fitted to the experimental value and a temperature broadening applied to the results. (B) Single-particle eigenvalues at  $\Gamma$ -point (left) and 1d atomistic wave functions (right) of the relevant near-band-gap states. Bottom right: atomic structure of the ZnS slab used in the simulations. Reprinted from [147].

The calculations show that crystal field and SO splitting between  $h_0$ ,  $h_1$  and  $h_2$

states in the valence band for ZnS NPLs are in the range of tens of meV and hence not large enough to produce experimentally resolved absorption peaks. This explains the relatively large broadening of the first absorption band. The second absorption peak at around 4.8 eV corresponds to a transition between lower conduction and higher valence band states with a single node (h4-e1 transition). The third absorption peak at around 5.62 eV corresponds to the transition between nodeless states (h1-e3 transition), where the electron state e3 originates from the second bulk conduction band at the  $\Gamma$ -point. The weak shoulder corresponds to the transitions between relatively deep bands, to the two-nodes states (h5-e2 transition).

The agreement between the calculations and the experimental results is qualitatively good with some quantitative differences. The second absorption peak is slightly too high in energy and the lowest peak slightly too low. Note that the single particle gap is at 4.25 eV, which is over 100 meV below the experimental result. The differences can be attributed to the lack of correlation effects in the calculations and possibly the presence of out-of-plane strain, which would explain the underestimated band gap, for example due to surface reconstruction, when the inter-atomic distances may be altered leading to the appearance of strain [121].

## 5.2 Solvent-dependent dielectric screening

In this part different approaches to treat theoretically the environmental dependence of the optical properties of QDs are used and compared and a detailed matching to experimental results is presented, which is used to validate the AEP approach (with SO coupling and  $\beta$ -correction) in combination with the final screening model.

### 5.2.1 The role of the polarization terms

First of all, a comparison to earlier theoretical work and assessment of the famous cancellation of the Coulomb surface polarization term  $J_{\text{pol}}$  with the surface self-energy term  $\Sigma^{\text{pol}}$  [92, 89] was done. In Fig. 5.3a) single-particle ( $E_0$ ), quasiparticle ( $E_{\text{QP}}$ ) and optical ( $E_{\text{opt}}$ ) band gaps are shown for an InP QD with 17.5 Å radius as a function of the dielectric constant of the environment  $\epsilon_{\text{out}}$ .

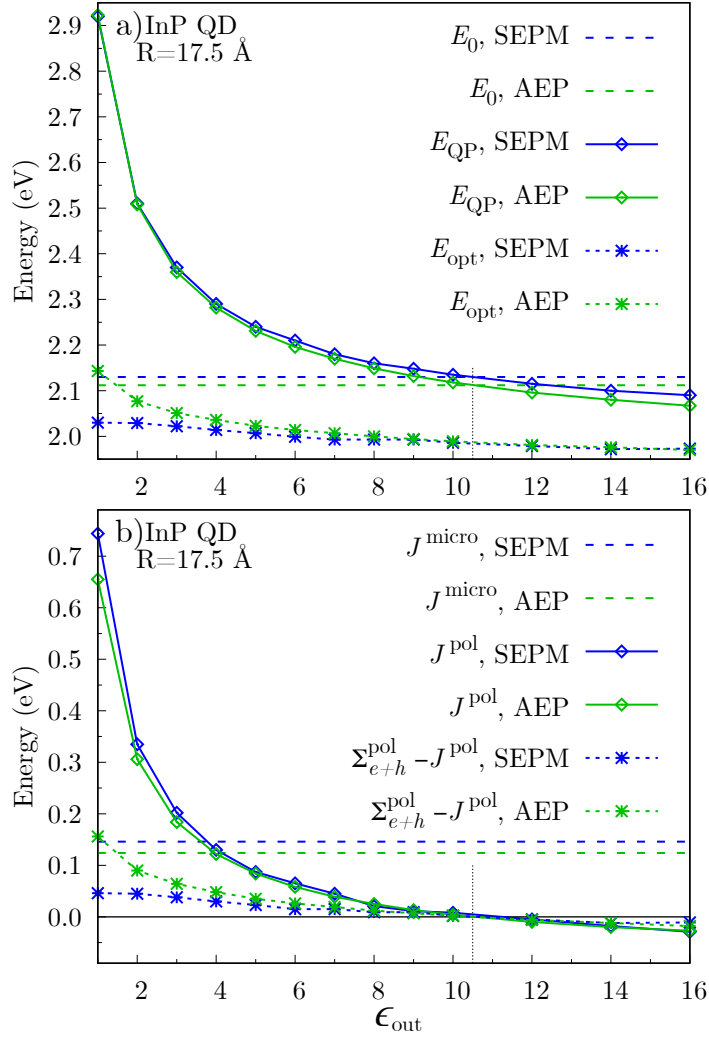


Figure 5.3: a) Single-particle, quasiparticle and optical band gaps as a function of the dielectric constant of the surrounding  $\epsilon_{\text{out}}$ . b) microscopic  $J^{\text{micro}}$ , polarization  $J^{\text{pol}}$  and difference  $\Sigma_{e+h}^{\text{pol}} - J^{\text{pol}}$  as a function of  $\epsilon_{\text{out}}$ . The AEP results (green) are compared to the semi-empirical pseudopotential method (SEPM) results of Ref.[91] (blue), both are obtained for a spherical InP QD with  $17.5 \text{ \AA}$  radius and  $\epsilon_{\text{in}} = 10.5$ . Reprinted from [94].

Fig. 5.3 demonstrates, that  $E_0$  is independent of  $\epsilon_{\text{out}}$ , while  $E_{\text{opt}}$  depends weakly and  $E_{\text{QP}}$  strongly on  $\epsilon_{\text{out}}$ . The results are compared to the previously developed model of Zunger and Franceschetti [91], where SEPs were used [81]. An overall very good agreement between AEP and SEPM approaches is observed, the only noticeable difference is for a strong dielectric mismatch (small values of  $\epsilon_{\text{out}}$ ), where the optical band gap from the AEP is somewhat larger than from the SEPM calculations. This difference is attributed to the different treatment of the surface, where the non-spherical AEPs are used [130], while in the SEPM approach the empirical Gaussian potentials on the surface are considered [91].

In Fig. 5.3b) the individual terms entering the calculation of  $E_{\text{opt}}$  are shown:

$$E_{\text{opt}} = E_0 + \sum_{e+h}^{\text{pol}} - J^{\text{pol}} + J^{\text{micro}} \quad , \quad (5.1)$$

where  $\sum_{e+h}^{\text{pol}} = \sum_{e0}^{\text{pol}} + \sum_{h0}^{\text{pol}}$ . The microscopic term  $J^{\text{micro}}$  is independent of  $\epsilon_{\text{out}}$ , whereas the polarization terms show a strong dependence.

The same analysis was performed for the InP and CdSe QDs of the similar size (with the radius 13.5 Å and 14.0 Å, correspondingly) to show the transferability of the results. The calculated Coulomb and self-polarization terms are shown in Fig. 5.4.

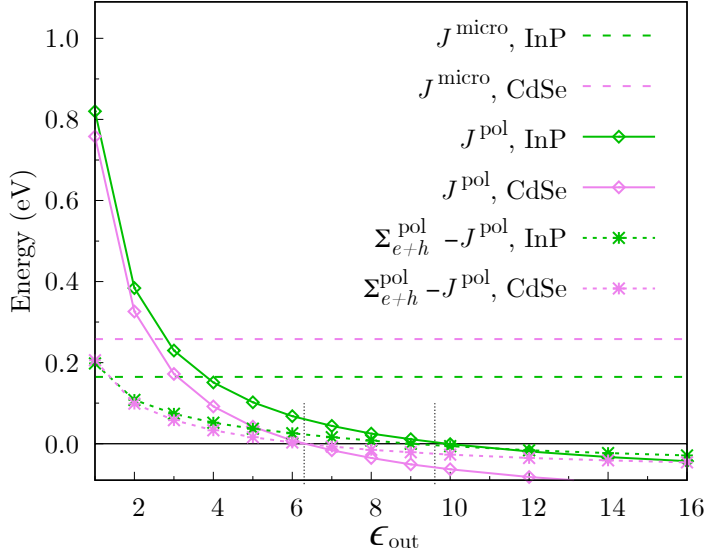


Figure 5.4: Microscopic  $J^{\text{micro}}$ , polarization  $J^{\text{pol}}$  and difference  $\sum_{e+h}^{\text{pol}} - J^{\text{pol}}$  as a function of  $\epsilon_{\text{out}}$ . The results for spherical InP QD with 13.5 Å radius and  $\epsilon_{\text{in},\infty}^{\text{bulk}} = 9.61$  (green) and spherical CdSe QD with 14.0 Å radius and  $\epsilon_{\text{in},\infty}^{\text{bulk}} = 6.3$  (pink) are shown.

The difference ( $\sum_{e+h}^{\text{pol}} - J^{\text{pol}}$ ) is rather small for both materials, which is in line with the expected cancellation of polarization terms based on electrostatic arguments [89] and tight binding GW[92]. However, this difference becomes none negligible for large dielectric mismatch (low dielectric constant of the outside material), where deviations up to 100 meV are observed.

### 5.2.2 Optical properties of CdSe and InP QDs in non-polar solvents

In Fig. 5.5 the quasiparticle band gap  $E_{\text{QP}}$  for spherical ZB InP and CdSe QDs in hexane ( $\epsilon_{\text{out}} = 1.89$ ) is plotted. The results of the most accurate solvent-dependent

model ( $J^{\text{total}}$ , see section 4.4.4) are shown as green stars. The experimental results for CdSe are shown as red squares and are in excellent agreement with the solvent-dependent results. The large discrepancy between the solvent-dependent (green) and the solvent-independent models (black) is easily understood: in the absence of dielectric boundary, as in the solvent-independent model, the polarization effects are absent and hence  $E_{\text{QP}} = E_0$ . The missing polarization self-energy term can become very significant for large dielectric mismatch, in agreement with what was shown in Fig.5.4).

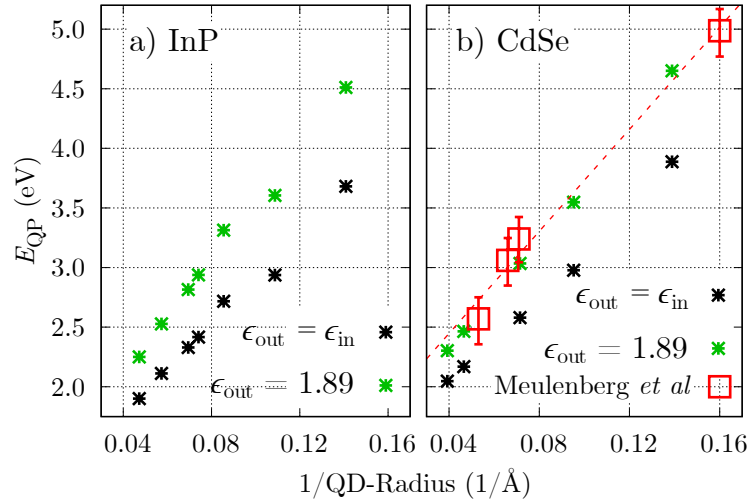


Figure 5.5: Quasiparticle band gap  $E_{\text{QP}}$  for a) InP and b) CdSe QDs as a function of the inverse QD radius for the solvent-independent screening model ( $\epsilon_{\text{in}} = \epsilon_{\text{out}}$ , black stars) and the solvent-dependent model for hexane ( $\epsilon_{\text{out}} = 1.89$ , green stars). The experimental results of Meulenber *et al.* [150] for CdSe in hexane are shown as red squares. The red dashed line is a guide to the eye. Reprinted from [94].

In Fig. 5.6 the calculated and measured [151, 150, 152, 153] optical band gaps for ZB InP and CdSe QDs are plotted. For the solvent-dependent screening model  $\epsilon_{\text{out}} = 1.89$  is considered. All calculations and experiments correspond to a large dielectric mismatch between the NC and the solvent ( $\epsilon_{\text{in},\infty}^{\text{bulk}}$  (CdSe) = 6.3 and  $\epsilon_{\text{in},\infty}^{\text{bulk}}$  (InP) = 9.61). The experiments of Refs. [151] and [150] (red squares) are in hexane ( $\epsilon_{\text{out}} = 1.89$ ), while the Refs. [152] and [153] (yellow squares) are in an unspecified oil mixture ( $\epsilon_{\text{out}} \approx 2$ ). Three types of calculations are performed: (i) using the exact solvent-dependent model with bulk  $\epsilon_{\text{in},\infty}^{\text{bulk}}$  (green stars) and (ii) using a solvent-independent ( $J^{\text{micro}}$ ) screening (see section 4.4.2) with a QD radius-dependent  $\epsilon_{\text{in},\infty}^{\text{QD}}$  (modified Penn model, see Section 4.4.3 for details) following Eq. (4.17) (gray circles) and (iii) using a solvent-independent model and bulk screening  $\epsilon_{\text{in},\infty}^{\text{bulk}}$  (black stars).

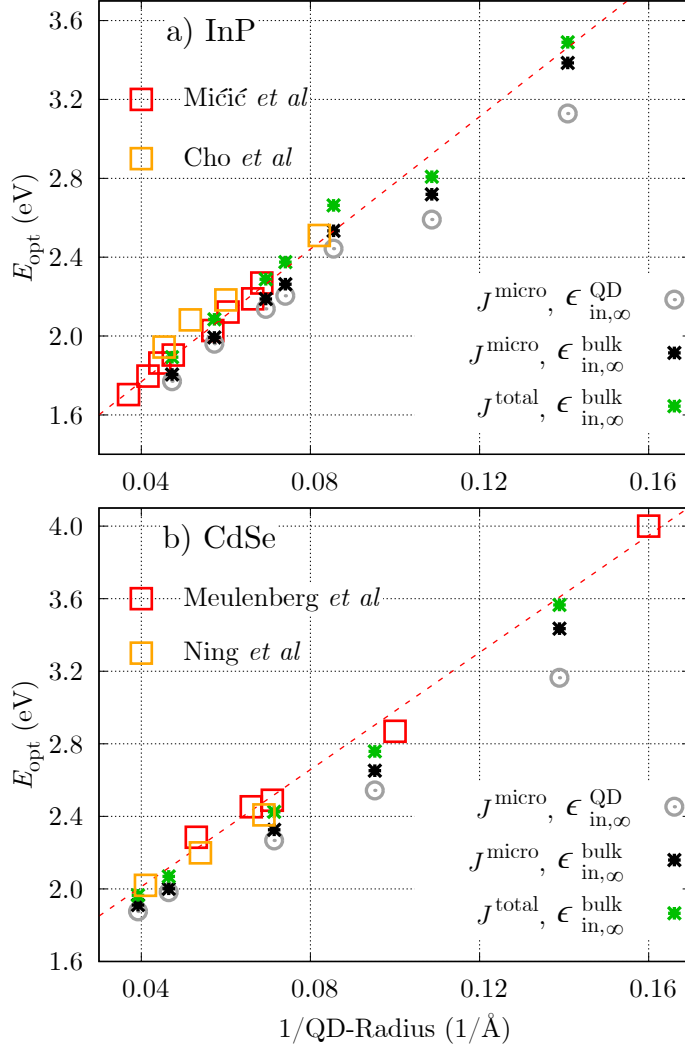


Figure 5.6: Optical gap  $E_{\text{opt}}$  for a) InP and b) CdSe QDs as a function of the inverse QD radius. The solvent-dependent screening model  $J^{\text{total}}$  with  $\epsilon_{\text{in},\infty}^{\text{bulk}}$  (green stars) and the solvent-independent screening models with  $\epsilon_{\text{in},\infty}^{\text{bulk}}$  (black stars) and  $\epsilon_{\text{in},\infty}^{\text{QD}}$  (gray circles) are shown. The experimental results for InP [151, 152] and CdSe [150, 153] are shown as squares. The experiments of Refs.[151] and [150] are in hexane ( $\epsilon_{\text{out}} = 1.89$ ) and of Refs.[152] and [153] are in an unspecified oil mixture ( $\epsilon_{\text{out}} \approx 2$ ). The red dashed line is a guide to the eye. Reprinted from [94].

The optical gaps calculated with the exact solvent-dependent model (green) are in very good agreement with experiment for the entire size range. In case of solvent-independent models (gray and black) it can be seen that the  $E_{\text{opt}}$  is underestimated, especially for the QDs with small sizes. However, the results using high-frequency bulk screening (black stars) are in reasonable agreement with the experiment and the full dielectric model (green). Comparing both solvent-independent models, one may notice that the usage of the QD-radius-dependent screening (gray) performs

significantly worse than the plain bulk screening (black). Generally, it is advisable to use the full bulk dielectric constant  $\epsilon_{\text{in},\infty}^{\text{bulk}}$  instead of the reduced  $\epsilon_{\text{in},\infty}^{\text{QD}}$  (modified Penn model) value and present the understanding of the effect qualitatively in Fig.4.17: While the modified Penn model (blue in Fig.4.17) leads to a smooth but steady reduction of  $\epsilon_{\text{in},\infty}$  when the QD size is reduced, a more abrupt transition from the bulk value to a lower value probably occurs (black dashed line, drawn qualitatively). So that the modified Penn model leads to a significantly too low dielectric constant. Further important conclusion is that the deviation between the different screening models for the calculation of the optical gap becomes insignificant for large QDs, where  $\epsilon_{\text{in},\infty}^{\text{QD}}$  approaches  $\epsilon_{\text{in},\infty}^{\text{bulk}}$  and the polarization Coulomb interaction term  $J^{\text{pol}}$  and the electron-hole polarization self-energies  $\sum_{e,h}^{\text{pol}}$  almost cancel each other.

Additionally, calculated and experimental exciton binding energies (Eq. (2.33)) are compared for CdSe QDs in Fig. 5.7.

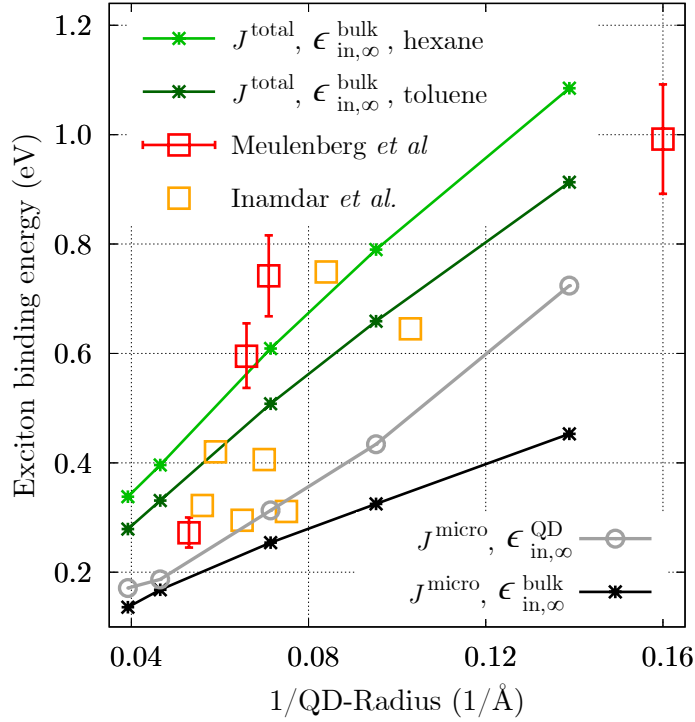


Figure 5.7: Exciton binding energy for CdSe QDs as a function of the inverse QD radius, calculated using the solvent-dependent screening model  $J^{\text{total}}$  with  $\epsilon_{\text{in},\infty}^{\text{bulk}}$  for hexane (light green stars) and toluene (dark green stars) as well as using the solvent-independent screening model  $J^{\text{micro}}$  with  $\epsilon_{\text{in},\infty}^{\text{bulk}}$  (black stars) and radius-dependent  $\epsilon_{\text{in},\infty}^{\text{QD}}$  (gray circles). The corresponding experimental results for hexane [150] ( $\epsilon_{\text{out}} = 1.89$ ) and toluene [154] ( $\epsilon_{\text{out}} = 2.39$ ) solvents and are shown as red and yellow squares, respectively. Reprinted from [94].

It can be seen that the solvent-independent  $J^{\text{micro}}$  screening model with  $\epsilon_{\text{in},\infty}^{\text{bulk}}$

(black stars) heavily underestimates the exciton binding energy. On the other hand, the solvent-independent screening model  $J^{\text{micro}}$  together with the modified Penn model  $\epsilon_{\text{in},\infty}^{\text{QD}}$  (gray circles) shows reasonable qualitative dependence, even though the exciton binding energy is quantitatively underestimated. Both solvent-dependent models reproduce the experimental results rather well. Results for the exciton binding energy for toluene ( $\epsilon_{\text{out}} = 2.39$ ) are from 10 meV up to 170 meV lower, depending on the QD size. Overall, the solvent-dependent model combined with  $\epsilon_{\text{in},\infty}^{\text{bulk}}$  shows again the best agreement with the experimental results.

### 5.2.3 The role of the shape and crystal structure (CdSe QDs)

In Fig. 5.8  $E_{\text{opt}}$  is compared to further experimental [155, 156, 13] and theoretical results[155] for CdSe QDs in solvents with higher dielectric constants ( $\epsilon_{\text{out}} \approx 5.0$ ). The results for ZB and WZ CdSe QDs are shown, as well as two different shapes for the large ZB QDs: default spherical as well as faceted (truncated octahedron). Both shapes are shown in the inset of Fig. 5.8.

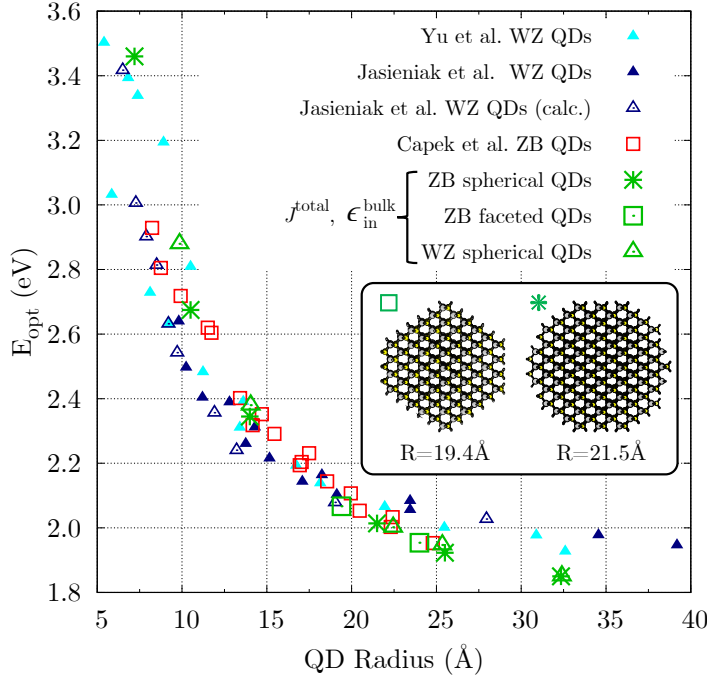


Figure 5.8:  $E_{\text{opt}}$  as a function of QD radius with  $\epsilon_{\text{in},\infty}^{\text{bulk}}$  for ZB spherical (green stars), ZB faceted (green squares) and WZ spherical (green triangles) QDs in chloroform ( $\epsilon_{\text{out}} = 4.72$ ) together with theoretically predicted [155] (empty triangles) and experimentally measured (filled triangles) optical gaps for WZ CdSe QDs in chloroform [155] (dark-blue) and aqueous (light-blue) solution [156] ( $\epsilon_{\text{out}} = 5.2$ ) as well as experimental data for ZB QDs in chloroform (red squares) [13]. In addition to the different crystal structures, QDs with spherical and faceted shapes are considered (see inset). Reprinted from [94].

An overall excellent agreement between theory and experiment is obtained for the ZB QDs. However, unlike the experimental results from Ref.[13], there is no significant shift in the optical band gap observed when going from WZ (triangles) to ZB QDs (squares). It can be explained by the differences in surface passivation, which will be discussed in the next section. Also the shape of the NCs does not influence the optical band gap significantly, at least with the definition of the QD radius which simply uses the distance from the central QD atom to the outmost atom, including pseudo-hydrogen atoms on the surface. Please note, that the TEM measurements of the diameter of the QDs have an uncertainty that has been quantified [155, 156] to be around 10-15%.

#### 5.2.4 The role of the passivant length (CdSe QDs)

To include the effect of the passivants on the dielectric environment, a third region with dielectric constant  $\epsilon_{\text{pass}}$  and width  $L_{\text{pass}}$  around the QD was introduced to the mask function (see Eq. (4.21)). The functional form is according to:

$$m_{\text{pass}}(\mathbf{r}) = \frac{1}{1 + \exp[(|\mathbf{r}| - (R + L_{\text{pass}}))/w_0]} ,$$

$$\epsilon(\mathbf{r}) = \epsilon_{\text{out}} + m(\mathbf{r})(\epsilon_{\text{in}} - \epsilon_{\text{pass}}) + m_{\text{pass}}(\mathbf{r})(\epsilon_{\text{pass}} - \epsilon_{\text{out}}) . \quad (5.2)$$

In Fig. 5.9a) the resulting  $\epsilon(\mathbf{r})$  is plotted for a QD with Radius  $R = 10.5 \text{ \AA}$ , a passivant width  $L_{\text{pass}} = 10 \text{ \AA}$  and  $w_0 = 1.89 \text{ \AA}$ . The black (blue) curve represents the case with toluene (chloroform) as solvent. For  $\epsilon_{\text{pass}}$  the value 2.1 is used, since it approximately corresponds to the high-frequency dielectric constant of most of the widely used organic long-chained passivants, including ODPA ( $\epsilon_{\text{pass}} = 2.13$ ).

In Fig. 5.9b) the optical band gap shift is shown as a function of the passivant length  $L_{\text{pass}}$  for two different solvents: toluene ( $\epsilon_{\text{out}}=2.39$ , shown in black) and chloroform ( $\epsilon_{\text{out}}=4.72$ , shown in blue). The  $L_{\text{pass}} = 0$  results correspond to the pseudo-hydrogen passivation results. The infinity results corresponds to the one-step  $\epsilon(\mathbf{r})$  results from Eq. (4.21) with  $\epsilon_{\text{out}} = 2.1$ . It can be seen that for long-chained organic passivants, such as ODPA, the dielectric properties are only weakly affected by the solvent; with an optical band gap shift of only 13 meV in the specific case. On the other hand, for short or atomistic passivation the dielectric properties of the solvent are important and the shift in the optical band gap reaches 58 meV in this case.

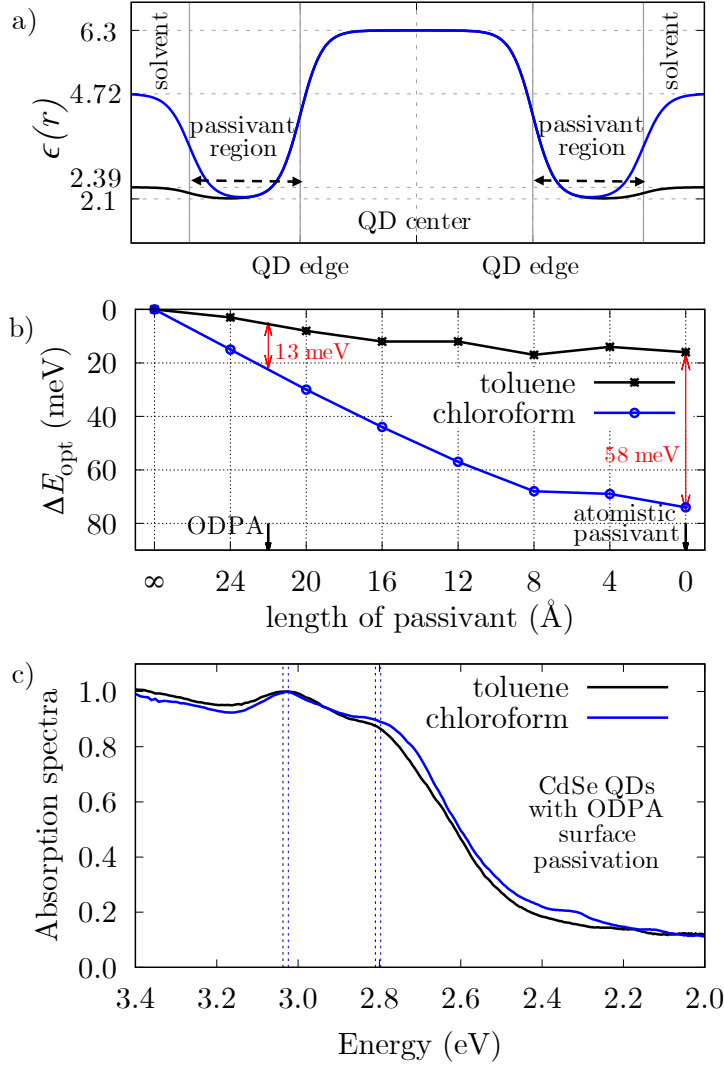


Figure 5.9: a) Two-step dielectric function  $\epsilon(r)$  including a passivant region (see Eq. (5.2)) for a QD with Radius  $R = 10.5 \text{ \AA}$  and a passivant width  $L_{\text{pass}} = 10 \text{ \AA}$ . b) Optical band gap shift  $\Delta E_{\text{opt}}$  for a CdSe QD with  $R = 10.5 \text{ \AA}$  and varying passivant length  $L_{\text{pass}}$  in toluene (black stars) and chloroform (blue circles). The length of ODPA and of atomistic passivants are shown with black arrows. c) Experimental absorption spectra (normalized) for the two identical fractions of ODPA-passivated CdSe QDs dispersed in toluene (black) and chloroform (blue). Reprinted from [94].

In Fig. 5.9c) the experimental absorption spectra is shown for two identical fractions of ODPA-passivated CdSe QDs dispersed in toluene and chloroform. The experimental results show no significant shift in the absorption peaks, in good agreement with the calculations that predicts a small shift of 13 meV, which cannot be resolved by experiment.

### 5.3 QD-QD coupled systems

Besides isolated nanocrystals, the advanced screening model was implemented to the QD-QD coupled systems in order to investigate the coupling effects observed experimentally in the close-packed films of colloidal QDs.

#### 5.3.1 Coupled systems of Si QDs with different QD radius

First, two coupled systems of Si QDs are considered, one with two QDs of  $R = 7.7\text{\AA}$  each and one with two QDs of  $R = 15\text{\AA}$  each. The inter-dot distance was fixed to  $3\text{\AA}$  in both cases. The normalized wave functions for the bonding-antibonding states originating from former isolated HOMO and LUMO QD states are shown in Fig. 5.10.

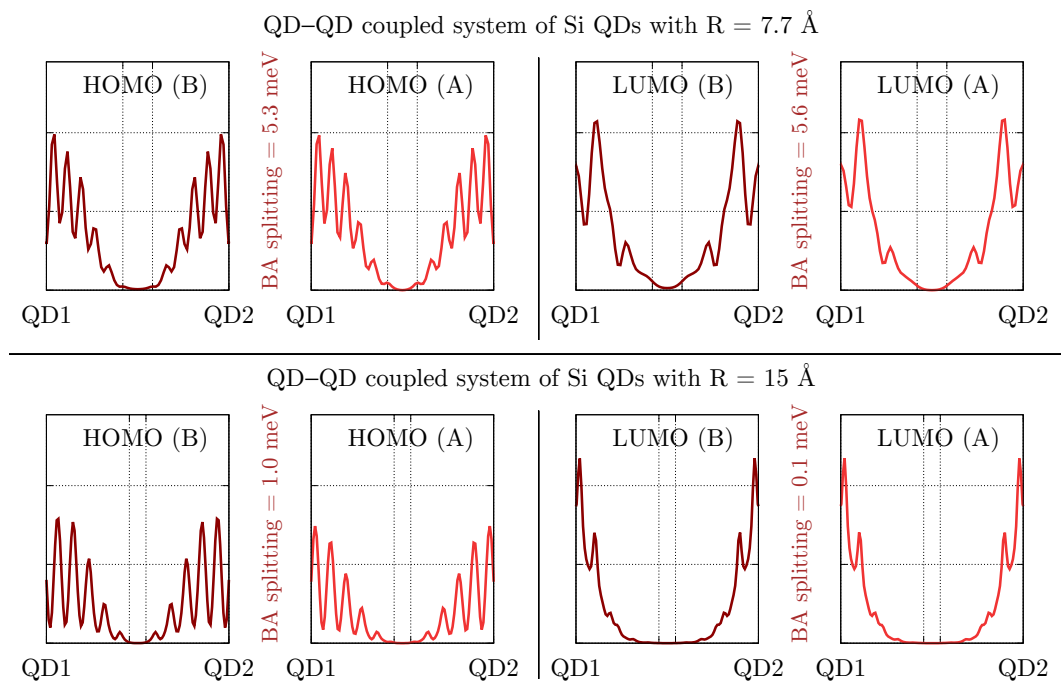


Figure 5.10: one-dimensional wave functions (normalized) of BA-states for coupled systems of small ( $R = 7.7\text{\AA}$ , upper panel) and relatively big Si QDs ( $R = 15\text{\AA}$ , lower panel). The plot starts at the center of the first QD and finishes at the center of the second QD. Inter-dot distance is fixed to  $3\text{\AA}$  in both cases.

From the electron density in the inter-dot region and bonding-antibonding (BA) splitting of HOMO and LUMO states, it can be concluded, that the coupling strength depends on the QD size, and direct coupling effect is stronger between the relatively

small QDs ( $R < 10\text{\AA}$ ). This effect can be explained by the wave function distribution inside the nanoparticle. The smaller is the QD, the more electron density is "leaking" to the surface and passivant atoms, and therefore coupling with the neighbors is easily possible. On the contrary, the bigger is the QD radius, the more electron density is confined within the central part, therefore the effective distance between the neighboring QDs is increased.

### 5.3.2 Formation of bonding–antibonding states in coupled systems of small Si, InP and CdSe QDs

The BA splitting versus distance and  $E_0$  band gap change in the QD-QD coupled systems of two small CdSe, InP and Si QDs ( $R < 10\text{\AA}$ ) are shown in Fig. 5.11.

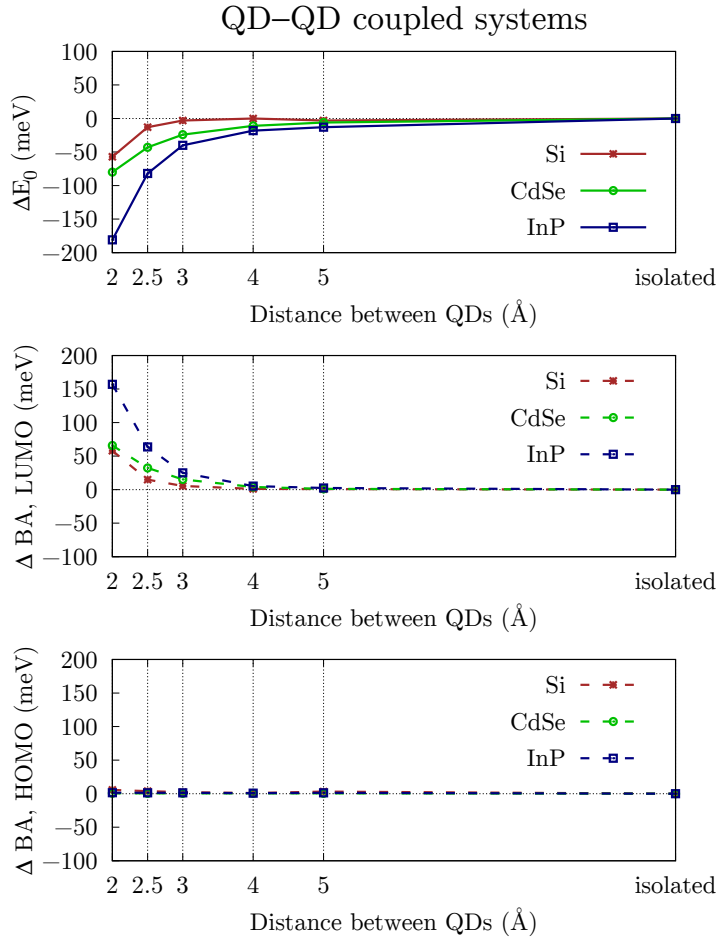


Figure 5.11: Top panel: reduction of the  $E_0$  band gap versus distance between coupled CdSe (green), InP (blue) and Si (red) QDs with  $R < 10\text{\AA}$ . BA splitting of HOMO and LUMO states are shown in the bottom and middle panels, correspondingly.

The  $2\text{\AA}$  distance is approaching the atomic bond length between the surface atom and its passivant and corresponds to the close-packed film. It is clear that the direct coupling effect and considerable closing of the band gap  $E_0$  occurs at distances less than  $4\text{\AA}$ , where the direct overlap of the wave functions is possible. InP QDs tend to be more sensitive to the coupling effect than the CdSe and Si QDs of the same size. The indirect nature of the Si QDs band gap leads to the strong inter-valley interactions between LUMO and upper CB states within one QD (see Fig. 4.1). Therefore Si QDs demonstrate more localised CB states and the smallest band gap change and BA splitting.

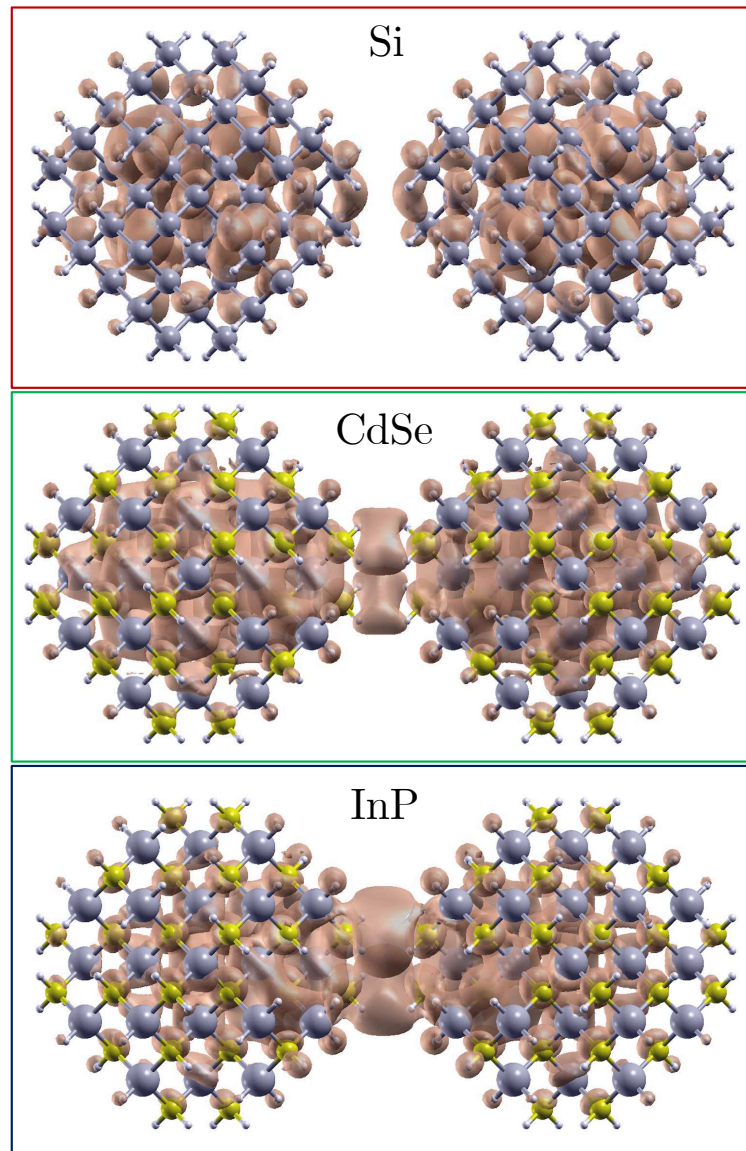


Figure 5.12: Wave function isosurfaces of LUMO binding states at 65% of electron density for coupled Si (red frame), CdSe (green frame) and InP (blue frame) QDs with  $R < 10\text{\AA}$ . Inter-dot distance is fixed at  $2.5\text{\AA}$  in all cases.

From the Fig. 5.11 it follows that the LUMO states are clearly more affected by the QD-QD coupling (BA splitting in order of tens of meV) than the HOMO states (BA splitting in order of meV), independently of the semiconductor material, which can be explained by the relatively low electron effective mass  $m_e$  in comparison with effective mass of the holes  $m_{hh}, m_{lh}$ .

The three-dimensional LUMO binding state wave function isosurfaces at 65% of electron density for the QD-QD coupled systems of different materials with inter-dot distance 2.5 Å are shown in Fig. 5.12. The isosurfaces qualitatively confirm the different coupling strength and show a direct connection between BA splitting (Fig. 5.11) and electron density in the inter-dot region.

### 5.3.3 InP QDs in close-packed films: absorption peak shift

First of all, the correlation effects were estimated in the coupled systems of InP QDs with  $R = 9\text{Å}$  versus distance using the single-particle wave functions and SC and CI theory (see Sections 2.4) with solvent-independent screening with  $\epsilon_{\text{in},\infty}^{\text{QD}}$  (modified Penn model). Observed correlation effects are shown in Fig. 5.13. It can be seen that correlation in the QD-QD coupled systems is quite strong (up to 150 meV) and has complicated non-linear behavior vs distance, therefore SC approximation cannot be used in such systems. We have used a CI basis of 5 valence and 3 conduction states (SO coupling included).

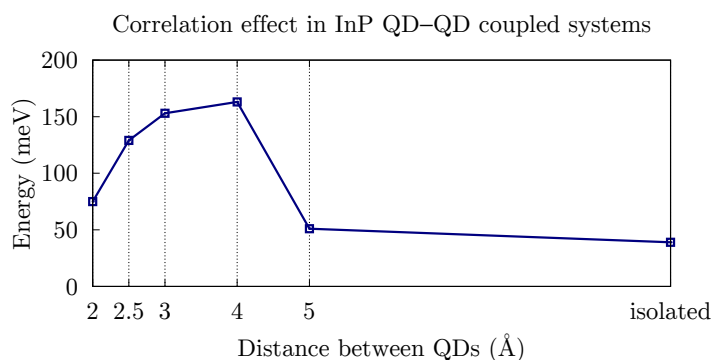


Figure 5.13: Correlation energy (meV) for the lowest exciton state in InP QD-QD ( $R = 9\text{Å}$  each) coupled systems versus inter-dot distance. CI basis of 5 valence and 3 conduction states is used (SO coupling included).

For the optical band gap  $E_{\text{opt}}$  calculations, besides modified Penn model, the solvent-dependent screening with  $\epsilon_{\text{in},\infty}^{\text{bulk}}$  and different surrounding environment, such as vacuum ( $\epsilon_{\text{out}} = 1.0$ ), toluene ( $\epsilon_{\text{out}} = 2.39$ ) and chloroform ( $\epsilon_{\text{out}} = 4.72$ ) is used (see Section 4.4 for details). The change of polarization terms depending on the  $\epsilon_{\text{out}}$

and inter-dot distance is investigated and shown in Fig. 5.14. The polarization self-energy term is calculated for single QD with reduced supercell size, because, unlike Coulomb interaction term  $J^{\text{pol}}$ , it cannot be calculated  $\sum_{e+h}^{\text{pol}}$  directly for the QD-QD coupled system due to limitations of the analytical model (see Eq. (2.29)). Please note that  $J^{\text{pol}}$  which is shown on the graph is only interaction between the first valence and first conduction state. It is the strongest polarization term, however, as it was already mentioned above, due to the correlation effects in close-packed films other  $J^{\text{pol}}$  terms should generally not be neglected.

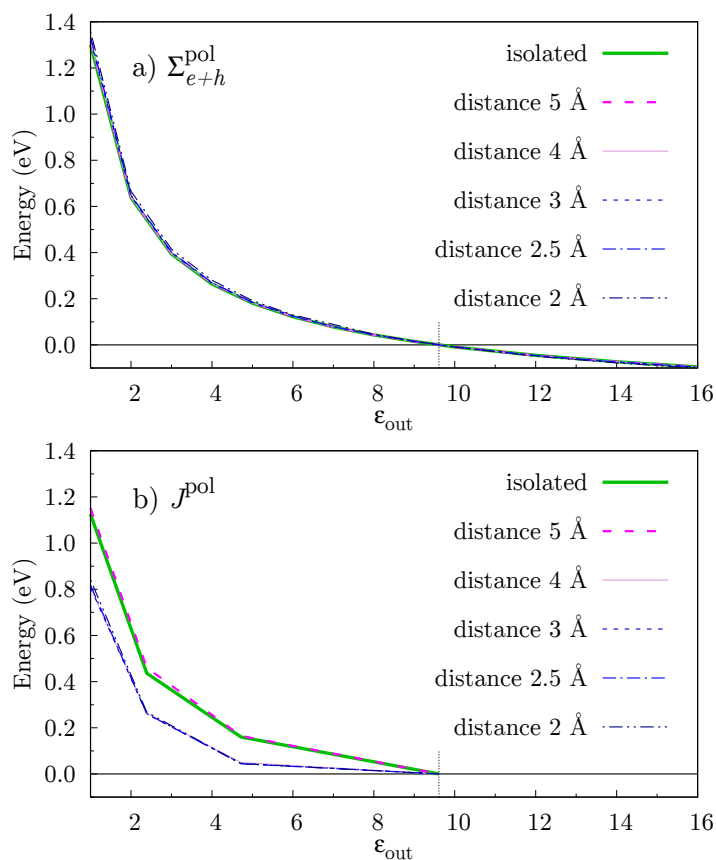


Figure 5.14: Polarization self-energy term (upper panel)  $\sum_{e+h}^{\text{pol}}$  and Coulomb polarization term  $J^{\text{pol}}$  (lower panel) for isolated InP QD with  $R = 9\text{\AA}$  and QD in close-packed film as a function of  $\epsilon_{\text{out}}$ .

The predicted optical band gap  $E_{\text{opt}}$  and absorption peak shift in the close-packed systems in comparison with isolated InP QDs was compared with experimental values for InP QDs with  $R=9\text{\AA}$  capped with hexylamine ( $\epsilon_{\text{out}} = 4.08$ ) and initially dispersed in an octane-hexane mixture ( $\epsilon_{\text{out}} \approx 2$ ) [151]. Close-packed films are formed in the experiment after the solvent evaporation. The closest inter-dot distance reached in the experiment is  $9\text{\AA}$ , but the length of the hexylamine molecule

used for QD surface passivation ( $l \approx 7.5\text{\AA}$ ), which might contribute to the wave function delocalization, should be considered. It is assumed, that the experimental close-packed distance corresponds to the  $2\text{\AA}$  inter-dot distance in the model system with atomistic passivant. The results are shown in Table 5.2.

	$\epsilon_{\text{in},\infty}^{\text{QD}}$ $\epsilon_{\text{in}} = \epsilon_{\text{out}}$	$\epsilon_{\text{in},\infty}^{\text{bulk}}$ $\epsilon_{\text{out}} = 1.0$	$\epsilon_{\text{in},\infty}^{\text{bulk}}$ $\epsilon_{\text{out}} = 2.39$	$\epsilon_{\text{in},\infty}^{\text{bulk}}$ $\epsilon_{\text{out}} = 4.72$	Mičić <i>et al</i> (opt. abs.)
$E_{\text{opt}}$	2.629 eV	2.997 eV	2.904 eV	2.867 eV	<b>2.86 eV</b>
red shift	66 meV	77 meV	72 meV	86 meV	<b>140 meV</b>

Table 5.2: Optical band gap of the single InP QDs with  $R = 9\text{\AA}$  as well as red shift of the absorption peak versus QD-QD distance, which was calculated as a difference between  $E_{\text{opt}}$  of isolated and close-packed QDs (inter-dot distance  $2\text{\AA}$ ) using different screening models. Experimental results from Ref.[151].

From the Table 5.2 it follows that the  $E_{\text{opt}}$  is underestimated by modified Penn model and predicted the most accurate with the solvent-dependent model and chloroform outside (which has dielectric constant close to the hexylamine). The absorption red shift is slightly underestimated by the calculations in all cases. This may be explained by the increased number of close neighbours in the experimental close-packed films or imperfection of the analytic calculation of the polarization self-energy term  $\sum_{e+h}^{\text{pol}}$  for coupled systems and requires further investigations.

## 5.4 Core-shell CdSe/CdS QDs with the sharp and alloyed interface

Besides one-compound materials, core-shell nanostructures with the sharp and alloyed interface were simulated, with the radius up to  $68\text{\AA}$  ( $> 50\,000$  atoms) - well beyond the capabilities of the standard *ab initio* methods such as DFT.

### 5.4.1 The role of the CdS shell thickness

Shell thickness plays an important role in the electronic and optical properties of the core-shell QDs and was the first point of the interest. CdSe/CdS QDs with the CdSe core radius of  $12\text{\AA}$  were chosen as model systems. According to experiment [157], they correspond to quasi-type II QDs, where valence (HOMO and lower) wave functions are confined within the CdSe core while conduction (LUMO and higher) wave functions are up to certain extent deconfined into the CdS shell (see Fig. 5.15).

The  $\beta$ -correction set for natural offsets is used in this case, and SO coupling is not included.

It is clear, that even very thin shell (3.0 Å correspond to 1 monolayer CdS) leads to the significant reduction of the band gap presumably due to conduction wave functions deconfinement. Further growth of the shell thickness mostly affects the LUMO/LUMO+1 offset which might be also connected to the relative confinement of the core and shell material and relative energy offset change. At shell thickness 16.5 Å, which corresponds to approximately 5 monolayers of CdS, the eigenvalues near band gap reach equilibrium, and it means, that the band gap and LUMO/LUMO+1 offset will no longer be dependent on further shell growth. This shell thickness will be further considered as stable enough to allow a separate study of the influence of the core-shell interface on the electronic properties.

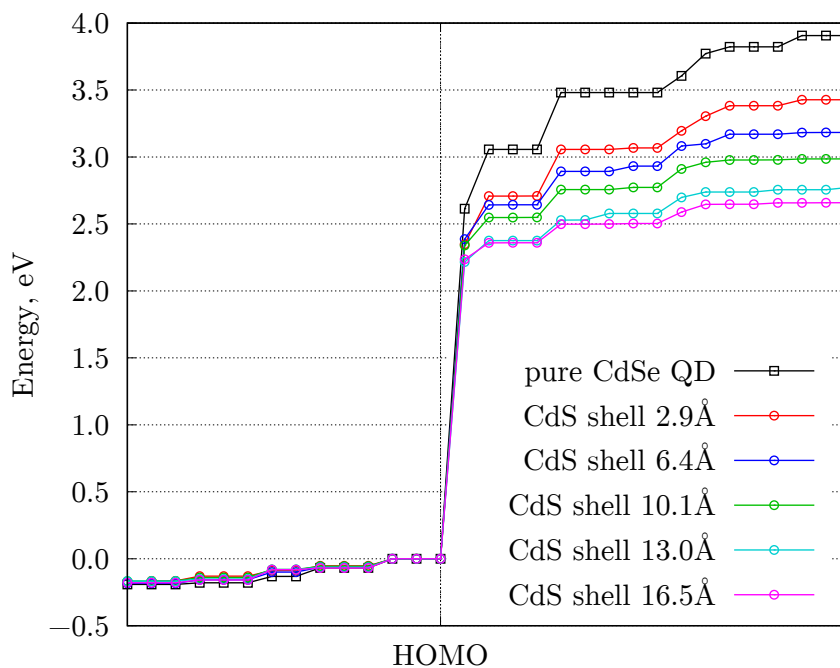


Figure 5.15: Eigenstates near band gap and corresponding eigenvalues for the CdSe/CdS core-shell QD with the CdSe core radius of 12 Å and gradually increased CdS shell thickness. Eigenvalues are aligned at HOMO.

The influence of the sharp and alloyed interface between core and shell materials on the electronic properties is investigated for the CdSe/CdS core-shell QDs with the CdSe core radius of 12 Å and 16.5 Å shell. In case of the alloyed interface, the alloy width of 12 Å with step and graduate alloy distributions plus 4 – 4.5 Å-thick CdS shell on top is used. With regard to step alloy, the probability to find core anion atom is literally the same in proximity to the core and to the surface

of QD (experimental probabilities vary from 52% near core to 46% near surface [39, 136]), whereas in case of graduate alloy the probability to find core anion atom changes gradually from 75% near core to 25% near surface [40, 136]. The eigenvalues without alignment as well as selected wave functions near band gap are presented in Fig. 5.16).

It can be observed that the presence of the alloyed interface affects mostly valence states, whereas conduction wave functions remain unchanged (see lower panel). In particular, the graduate alloyed interface leads to HOMO deconfinement to the shell and therefore the more significant reduction of the band gap. Please note, that the degeneracy of the valence wave functions is in fact slightly disturbed (several meV splitting) due to the broken symmetry of the alloyed core. The difference would become more pronounced if the alloyed interface was broader. However, the step alloy will be used in the further calculations to be consistent with the experimental data [39].

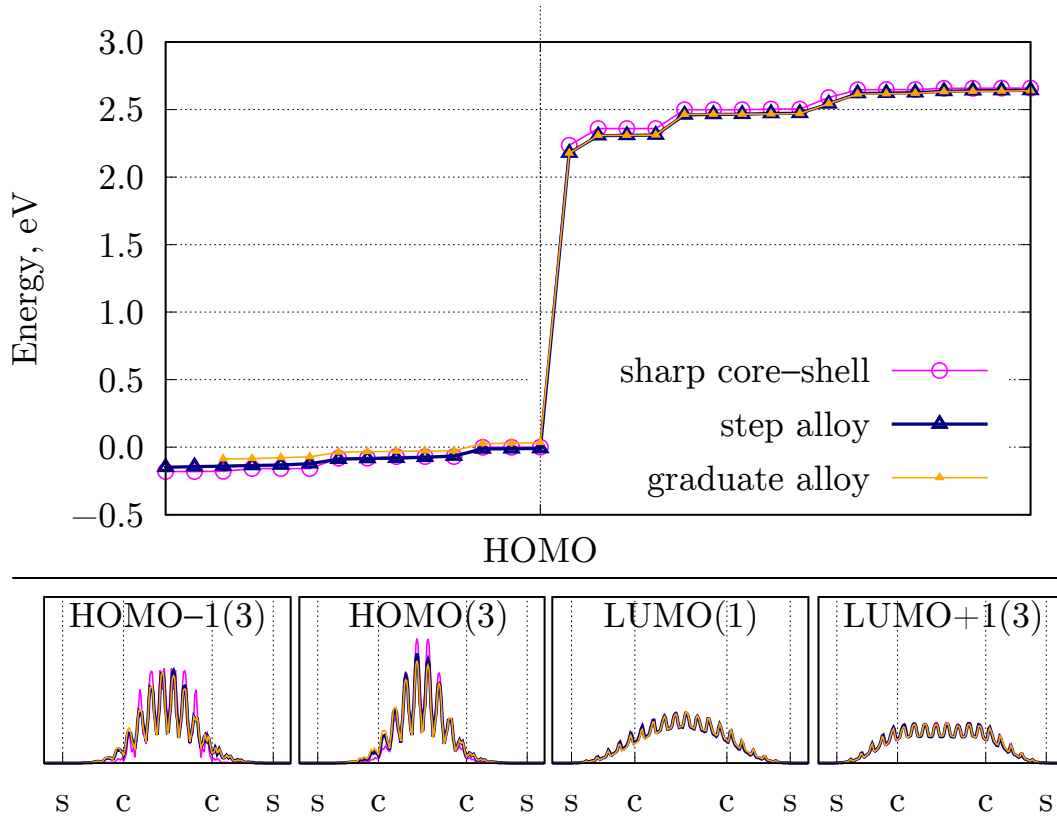


Figure 5.16: Upper panel: the eigenvalues of the CdSe/CdS core-shell QD with the CdSe core radius of  $12\text{\AA}$  and CdS shell thickness of  $16.5\text{\AA}$  (SO coupling is not included). The sharp core-shell (pink) interface is compared with the step (navy) and graduate (orange) alloyed interface. Lower panel: selected one-dimensional wave functions (normalized) around the band gap with the same color map for the sharp and alloyed interface. The core (c) and shell (s) border of QD are shown with the dashed lines.

### 5.4.2 The role of the CdSe core size

As the next step, the electronic properties for the different CdSe core radii are calculated, namely 12Å, 15Å and 19Å, in order to check how the core size influences on the QD electronic properties (band gap and LUMO/LUMO+1 as well as HOMO/HOMO-1 offsets). Pure CdSe QD is compared with core-shell CdSe/CdS QDs both with the sharp (shell thickness 16.0-16.5 Å) and step alloy (12 Å alloy thickness + 4.5 Å pure shell to avoid alloy directly at the QD surface) interfaces. The  $\beta$ -correction for the natural offsets was used, as before, but now for the case with SO coupling included in the calculation. The results can be observed in Fig. 5.17.

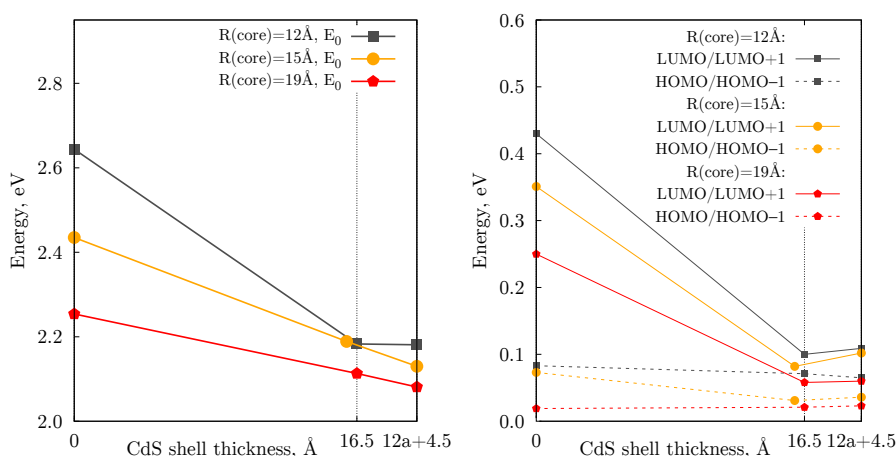


Figure 5.17: Optical properties of the pure CdSe and core-shell CdSe/CdS QDs with the different CdSe core radii (12 Å, 15 Å and 19 Å) and with the sharp (shell thickness 16.0-16.5 Å) and alloyed interface (12 Å alloy thickness + 4.5 Å pure shell).  $E_0$  band gap (left panel) and LUMO/LUMO+1 and HOMO/HOMO-1 offsets (right panel) versus shell thickness.

In Fig. 5.17, left panel, one can notice, that  $E_0$  gap for core-shell QDs with the core radii 12Å and 15Å are basically the same, presumably due to deconfinement of the conduction wave functions from CdSe core into CdS shell. For the core radius 19Å the  $E_0$  band gap changes less drastically from pure CdSe QD to core-shell QD. Overall, the reason for the observed effect is relative core and shell confinement which also alter energy offset between CdSe and CdS conduction states (see Fig. 4.14). This is confirmed by the change of LUMO/LUMO+1 offsets (right panel), which shrinks drastically after the addition of the shell. With regard to HOMO/HOMO-1 offsets, it can be seen that they are less sensitive to the shell. Alloy interface does not considerably change HOMO/HOMO-1 offsets and slightly increase LUMO/LUMO+1 offsets, but it leads to a slight decrease of the band gap  $E_0$  due to valence states deconfinement.

To show explicitly the effect of the deconfinement and check the experimentally

observed core-dependent transfer from quasi-type II ( $R(\text{core}) = 12\text{\AA}$ ) to type I ( $R(\text{core}) = 19\text{\AA}$ ) core-shell CdSe/CdS QDs [157], one-dimensional wave functions (normalized) are plotted for the corresponding QDs (shell thickness  $16.5\text{\AA}$ ) with the sharp and alloyed interface (see Fig. 5.18).

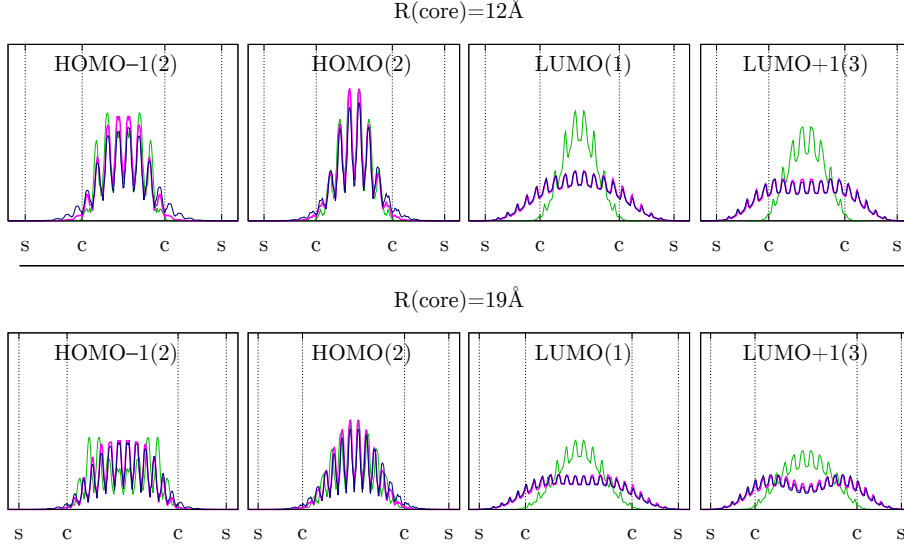


Figure 5.18: One-dimensional wave functions (normalized) near band gap for the pure CdSe (green) and core-shell CdSe/CdS QDs with the sharp (pink) and alloyed interface (step alloy, blue) and CdSe core radii of  $12\text{\AA}$  (upper panel) and  $19\text{\AA}$  (lower panel). Please note, that degeneracy of the alloyed wave functions is in fact slightly disturbed due to broken symmetry of the core. The core (c) and shell (s) border of QD are shown with the dashed lines.

The wave functions behavior in Fig. 5.18 supports the results shown previously. Unlike experimental results from Ref. [157], a considerable deconfinement of the conduction wave functions to the shell is observed even for the QD with  $R(\text{core}) = 19\text{\AA}$ , whereas valence wave functions are confined within core region, which means, no transfer from quasi-type II to type I core-shell CdSe/CdS QDs is observed (see Fig. 1.2). The alloyed interface does not affect conduction wave functions but leads to a slight deconfinement of the valence wave functions into the shell.

Additionally to the  $\beta$ -correction set with natural offsets between CdSe and CdS material, the case where bulk LDA offset is kept after the  $\beta$ -correction for the QDs with sharp core-shell interface and  $R(\text{core}) = 1\text{\AA}$  and  $R(\text{core}) = 19\text{\AA}$  was considered. For quantitative comparison the partial norm value of the LUMO wave function is calculated based on Eq. (2.7), but with the core radius as a limiting parameter. The results are shown in Fig. 5.19. Please note that due to the specificity of the one-dimensional wave function visualization (each point of the one-dimensional wave function along Z-direction of the supercell is in fact the sum of the values on

the corresponding XY plane) the central part of the wave function also partially includes the shell contribution.

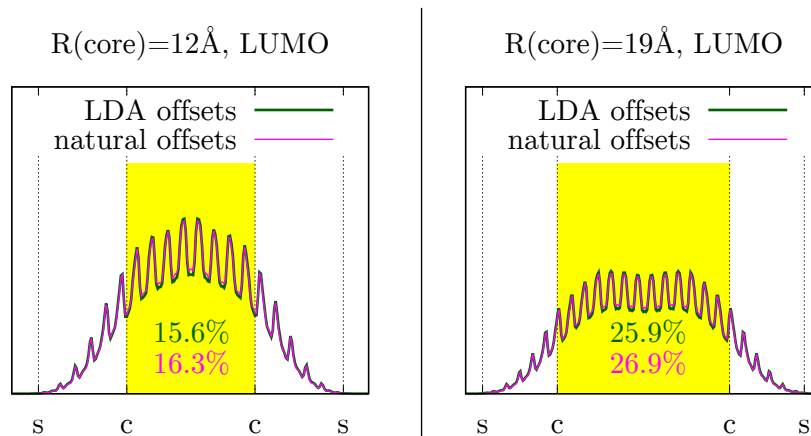


Figure 5.19: The influence of the  $\beta$ -correction sets with LDA (green) and natural (pink) bulk offset (see Fig. 4.14 for exact values) onto LUMO wave functions (one-dimensional, normalized). The core-shell CdSe/CdS QDs with the sharp interface and CdSe core radii of 12Å (left panel) and 19Å (right panel) are considered. The core (c) and shell (s) borders of QDs are shown with the dashed lines.

Relative core confinement for the LUMO wave functions obtained using  $\beta$ -correction with LDA and natural bulk offsets reveals noticeable, but insignificant difference in the wave function distribution. This can be partially justified by the really small difference for the CB offsets, in particular for the calculations with SO coupling (see Table 4.7). The partial norm of the LUMO wave function located in the core directly depends on the core size, so it can be presumed that with the further increase of the core radius and with the different choice of the  $\beta$ -set (make an emphasis on maintaining CB offset) the wave functions for LUMO and higher conduction states should eventually become fully confined in the core.

Finally, the single-particle band gaps for the CdSe/CdS QDs with the CdSe core radius 15Å and 16Å, 27Å and 52Å CdS shell on top are presented. For the two biggest shell sizes, the core-shell interface was simulated both sharp and with 15Å-wide alloy. The biggest QD ( $R = 68\text{\AA}$ ), calculated here on an atomistic level, consists of 55691 atoms (including 5436 passivants). The results were compared with the experimentally determined optical band gaps for the same NCs [39] on a qualitative basis. The results are shown in Fig. 5.20.

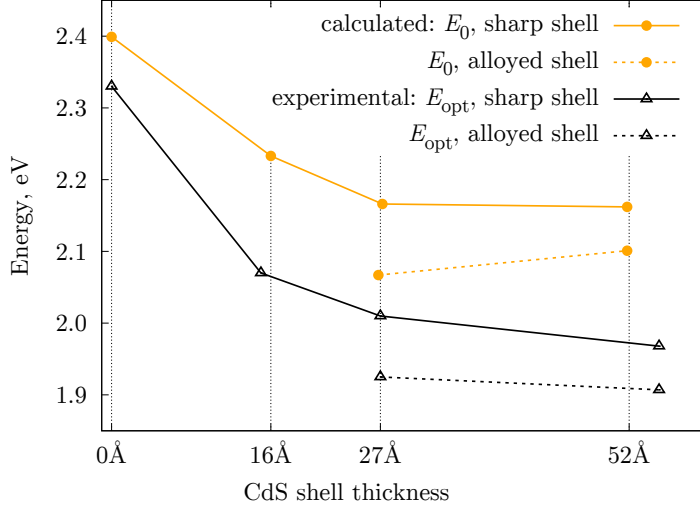


Figure 5.20: Theoretically predicted single-particle  $E_0$  band gap (orange) in comparison with experimentally measured optical band gap  $E_{opt}$  (black) (from Ref.[39]) for the CdSe/CdS QDs ( $R(\text{core}) = 15\text{\AA}$ ) with respect to the shell thickness, both for the sharp (solid lines) and  $15\text{\AA}$ -wide alloyed (dashed lines) core-shell interface.

From Fig. 5.20 it follows, that very good qualitative agreement of the changes caused by shell thickness modification is observed between single-particle (calculated) band gap and optical (experimentally observed) band gap. Also the features introduced by the alloyed interface are correctly captured in the calculation. The quantitative deviations might origin from the changes in polarisation term and will require calculations with the full screening model.

## Chapter 6

# Summary and outlook

In this work a new method to derive non-spherical AEPs for the passivant atoms was presented, which improves the results compared to the more traditional spherical pseudopotentials at no additional computational cost. It is shown that the imaginary part of the AEP introduces a local asymmetry in the vicinity of the passivant atom and energy offset on the border between vacuum and nanostructure, in agreement with the general understanding of surface-induced dipoles in physics. In the test cases of Si, InP and CdSe nanostructures an excellent transferability of the passivant AEPs is demonstrated and maximum energy deviations from standard *ab initio* DFT-LDA method prediction are within 200 meV for the small QWs, where surface effects are very important. The new AEP method, therefore, represents a significant improvement over former approaches that only lead to a qualitative result for the passivant, such as an absence of surface states within the band gap. For larger QD structures the agreement with DFT improves to an error below 100 meV. The AEP method is rather universal, so that not only passivant such as hydrogen or pseudo-hydrogen (for III-V and II-VI group semiconductors), but other atomic passivants like Chlorine (Cl) or Fluorine (F) can be constructed, and there are also possibilities to include other functional groups like Hydroxyl ( $\text{OH}^-$ ) or Methyl ( $\text{CH}_3^-$ ).

The main benefit of the improved AEP approach is that it opens the possibility to study surface-related phenomena at the *ab initio* level literally for the whole experimental size range and that it represents a large simplification in the generation of the pseudopotentials because of simple analytic connection with the DFT-LDA method. Furthermore, the AEP approach was supplemented with an empirical bulk single-particle band gap correction ( $\beta$ -correction). The latter comprehensive approach together with the VFF interface relaxation was implemented for rather complex core-shell QDs with the CdSe core radii from 12Å to 19Å, sharp and alloyed interface. It was demonstrated, that the shell thickness for the CdSe/CdS QDs

plays an important role in the band gap determination due to strong conduction states deconfinement, whereas the alloyed core-shell interface influences mostly on the valence wave functions properties. No significant influences are traced of the LDA and natural band offsets between CdSe and CdS, used in the  $\beta$ -correction, on the wave function confinement for the selected core-shell QDs. The theoretically predicted single-particle band gaps show the excellent qualitative agreement in comparison with experimentally measured optical band gaps.

The AEP-based approach was also implemented for Si, InP, and CdSe QD-QD coupled systems and observed BA splitting as a result of the direct coupling between QDs of different sizes. The coupling is the strongest between QDs with  $R < 10\text{\AA}$  due to near-surface wave function distribution in the nanocrystal, and BA splitting is much stronger for conduction states than for valence, presumably due to differences between electron and hole effective masses. A very clear (and even technically implemented) perspective for the quantitative comparison of the calculated and experimentally measured optical band gaps for core-shell QDs with sharp and alloyed interface can be seen. Moreover, the developed method has wide perspectives for even more complex structures modeling, such as core-shell-shell QDs, Quantum rods and QD-Qrod coupled systems.

The single-particle wave functions from the AEP approach were used within the CI framework in combination with various modeling techniques for the dielectric screening to account for the influence of the surrounding medium on the optical properties of the colloidal NCs. The quasiparticle and optical gaps of the ZnS 2D NPLs, InP and CdSe QDs are calculated. The final screening model consists of a constant bulk dielectric constant inside the QD with a sharp transition at the QD interface to the high-frequency dielectric constant of the environment. The AEP results in comparison with the earlier SEPM results show deviations in the 100 meV range for the large dielectric mismatch, which validates both computational approaches. Additionally, a broad comparison of the final screening model with experimental measurements is performed, and an excellent agreement is demonstrated. It is shown, that the sum of the polarization self-energy and the Coulomb surface polarization terms nearly cancels, when the dielectric mismatch is small, but sums up to 50 – 140 meV for the largest mismatches. The given energy range corresponds to results for QDs of different sizes, with the tendency to become smaller for larger QDs. It was also demonstrated that a simplified solvent-independent screening model (with lower computational cost) leads to rather small errors for the optical gaps (below 140 meV) and can be considered as a good alternative. Interestingly, this good agreement is obtained using the full dielectric constant of the semiconductor and not the reduced radius-dependent value based on the modified

Penn model. However, the use of these models is inappropriate for the calculation of quasiparticle gaps or exciton binding energies which require the surface self-energy term, since it can be as large as 700 meV for QDs with the large dielectric mismatch.

For isolated CdSe quantum dots, the environment is modeled considering separately passivant with varying length and solvent contributions. It is shown that commonly used long-chained organic passivant molecules effectively shield the effect of the solvent so only small shifts in the optical gap for different solvents (within 10 meV) are traceable. For short-chained or atomic passivants, however, the solvent effects on the optical gap are more significant (up to 100 meV). Using the same approach, as for the passivant-solvent screening function, it is already technically possible to implement two-step macroscopic screening for the core-shell QDs.

Finally, the correlation effects and the optical red-shift occurring because of the coupling of two InP QDs is calculated, with a good agreement between experimental data and the final screening model. However, the analytical model for the self-polarisation term is not optimized for coupled systems, and there are promising perspectives in the screening method development for the non-spherical nanostructures as well as QD-QD coupled systems with the atomic bridge. Another challenging topic would be modeling of trions and biexcitons in QDs as well as exciton-trion interactions in coupled systems of QDs using the developed comprehensive method.



# Bibliography

- [1] J.R. Christman. *Fundamentals of Solid State Physics*. Wiley, New York, 1988.
- [2] N.W. Ashcroft and N.D. Mermin. *Solid state physics*. Harcourt College Publishers, 1976.
- [3] A.G. Jackson. *Handbook of Crystallography for Electron Microscopists and Others*. Springer, 1991.
- [4] F. Seitz. *The modern theory of solids*, volume 548. New York: McGraw-Hill, 1940.
- [5] P.Y. Yu and M. Cardona. *Fundamentals of semiconductors: physics and materials properties*. Springer, 4th edition, 2010.
- [6] K. Seeger. *Semiconductor physics*. Springer Science & Business Media, 2013.
- [7] B. Davari, R.H. Dennard, and G.G. Shahidi. CMOS scaling for high performance and low power — the next ten years. *Proceedings of the IEE*, 83(4):595–606, 1995.
- [8] D.J. Frank, R.H. Dennard, E. Nowak, P.M. Solomon, Y. Taur, and H.S. Wong. Device scaling limits of Si MOSFETs and their application dependencies. *Proceedings of the IEE*, 89(3):259–288, 2001.
- [9] W. Hafez and M. Feng. Experimental demonstration of pseudomorphic heterojunction bipolar transistors with cutoff frequencies above 600 GHz. *Applied Physics Letters*, 86(15):152101, 2005.
- [10] D.W. Langer, Y.S. Park, and R.N. Euwema. Phonon coupling in edge emission and photoconductivity of CdSe, CdS, and Cd(Se(x)S(1-x)). *Physical Review*, 152(2):788, 1966.
- [11] A. Kudo and M. Sekizawa. Photocatalytic h<sub>2</sub> evolution under visible light irradiation on ni-doped zns photocatalyst. *Chemical Communications*, 15:1371–1372, 2000.

- 
- [12] K.B. Subila, G. Kishore Kumar, S.M. Shivaprasad, and K. George Thomas. Luminescence properties of CdSe quantum dots: role of crystal structure and surface composition. *The Journal of Physical Chemistry Letters*, 4(16):2774–2779, 2013.
- [13] R.K. Čapek, I. Moreels, K. Lambert, D. De Muynck, Q. Zhao, A. Van Tomme, F. Vanhaecke, and Z. Hens. Optical properties of zincblende CdSe quantum dots. *Journal of Physical Chemistry C*, 114:6371–6376, 2010.
- [14] A. Teitelboim and D. Oron. Broadband near-infrared to visible upconversion in quantum dot-quantum well heterostructures. *ACS nano*, 10(1):446–452, 2016.
- [15] M. Fox. *Optical properties of solids*. Oxford University Press, 2002.
- [16] C.J. Delerue and M. Lannoo. *Nanostructures: theory and modeling*. Springer Science & Business Media, 2013.
- [17] H. Weller. Quantized semiconductor particles: a novel state of matter for materials science. *Advanced Materials*, 5(2):88–95, 1993.
- [18] L. Brus. Electronic wave functions in semiconductor clusters: experiment and theory. *The Journal of Physical Chemistry*, 90(12):2555–2560, 1986.
- [19] J.S. Son, J.H. Yu, S.G. Kwon, J. Lee, J. Joo, and T. Hyeon. Colloidal synthesis of ultrathin two-dimensional semiconductor nanocrystals. *Advanced Materials*, 23(28):3214–3219, 2011.
- [20] S. Ithurria, M.D. Tessier, B. Mahler, R.P.S.M. Lobo, B. Dubertret, and A.L. Efros. Colloidal nanoplatelets with two-dimensional electronic structure. *Nature materials*, 10(12):936, 2011.
- [21] C. Bouet, M.D. Tessier, S. Ithurria, B. Mahler, B. Nadal, and B. Dubertret. Flat colloidal semiconductor nanoplatelets. *Chemistry of Materials*, 25(8):1262–1271, 2013.
- [22] V. Biju, T. Itoh, A. Anas, A. Sujith, and M. Ishikawa. Semiconductor quantum dots and metal nanoparticles: syntheses, optical properties, and biological applications. *Analytical and bioanalytical chemistry*, 391(7):2469–2495, 2008.
- [23] F. Wang, A. Dong, and W.E. Buhro. Solution–liquid–solid synthesis, properties, and applications of one-dimensional colloidal semiconductor nanorods and nanowires. *Chemical reviews*, 116(18):10888–10933, 2016.

- [24] Y. Pu, F. Cai, D. Wang, J.X. Wang, and J.F. Chen. Colloidal synthesis of semiconductor quantum dots toward large-scale production: a review. *Industrial & Engineering Chemistry Research*, 57(6):1790–1802, 2018.
- [25] M.H. Huang, S. Mao, H. Feick, H. Yan, Y. Wu, H. Kind, E. Weber, R. Russo, and P. Yang. Room-temperature ultraviolet nanowire nanolasers. *Science*, 292(5523):1897–1899, 2001.
- [26] M. Bruchez, M. Moronne, P. Gin, S. Weiss, and A.P. Alivisatos. Semiconductor nanocrystals as fluorescent biological labels. *Science*, 281(5385):2013–2016, 1998.
- [27] I.L. Medintz and H. Mattoussi. Quantum dot-based resonance energy transfer and its growing application in biology. *Physical Chemistry Chemical Physics*, 11(1):17–45, 2009.
- [28] M. Cheki, M. Moslehi, and M. Assadi. Marvelous applications of quantum dots. *European Review for Medical and Pharmacological Sciences*, 17(9):1141–1148, 2013.
- [29] A.A. Karpulevich, E.G. Maksimov, N.N. Sluchanko, A.N. Vasiliev, and V.Z. Paschenko. Highly efficient energy transfer from quantum dot to allophycocyanin in hybrid structures. *Journal of Photochemistry and Photobiology B: Biology*, 160:96–101, 2016.
- [30] H.V. Demir, S. Nizamoglu, T. Erdem, E. Mutlugun, N. Gaponik, and A. Eychmüller. Quantum dot integrated LEDs using photonic and excitonic color conversion. *Nano Today*, 6(6):632–647, 2011.
- [31] K. Bourzac. Quantum dots go on display. *Nature*, 493(7432):283, 2013.
- [32] D. Ge, E. Lee, L. Yang, Y. Cho, M. Li, D.S. Gianola, and S.A. Yang. A robust smart window: reversibly switching from high transparency to angle-independent structural color display. *Advanced Materials*, 27(15):2489–2495, 2015.
- [33] W.U. Huynh, J.J. Dittmer, and A.P. Alivisatos. Hybrid nanorod-polymer solar cells. *Science*, 295(5564):2425–2427, 2002.
- [34] A.J. Nozik, M.C. Beard, J.M. Luther, M. Law, and R.J. Ellingson. Semiconductor quantum dots and quantum dot arrays and applications of multiple exciton generation to third-generation photovoltaic solar cells. *Chemical reviews*, 110(11):6873–6890, 2010.

- 
- [35] C.R. Kagan and C.B. Murray. Charge transport in strongly coupled quantum dot solids. *Nature nanotechnology*, 10(12):1013, 2015.
- [36] C.R. Kagan, E. Lifshitz, E.H. Sargent, and D.V. Talapin. Building devices from colloidal quantum dots. *Science*, 353(6302):aac5523, 2016.
- [37] O. Chen, J. Zhao, V.P. Chauhan, J. Cui, C. Wong, D.K. Harris, H. Wei, H.S. Han, D. Fukumura, R.K. Jain, and M.G. Bawendi. Compact high-quality CdSe–CdS core–shell nanocrystals with narrow emission linewidths and suppressed blinking. *Nature materials*, 12(5):445–451, 2013.
- [38] B.C. Fitzmorris, J.K. Cooper, J. Edberg, S. Gul, J. Guo, and J.Z. Zhang. Synthesis and structural, optical, and dynamic properties of core/shell/shell CdSe/ZnSe/ZnS quantum dots. *The Journal of Physical Chemistry C*, 116(47):25065–25073, 2012.
- [39] W.K. Bae, L.A. Padilha, Y.S. Park, H. McDaniel, I. Robel, J.M. Pietryga, and V.I. Klimov. Controlled alloying of the core–shell interface in CdSe/CdS quantum dots for suppression of Auger recombination. *ACS nano*, 7(4):3411–3419, 2013.
- [40] G.E. Cragg and A.L. Efros. Suppression of Auger processes in confined structures. *Nano letters*, 10(1):313–317, 2010.
- [41] P. Reiss, M. Protiere, and L. Li. Core/shell semiconductor nanocrystals. *Small*, 5(2):154–168, 2009.
- [42] C. Zhai, H. Zhang, N. Du, B. Chen, H. Huang, Y. Wu, and D. Yang. One-pot synthesis of biocompatible CdSe/CdS quantum dots and their applications as fluorescent biological labels. *Nanoscale*, 6(1):31, 2011.
- [43] Y. Zhang, Y. Li, and X.P. Yan. Aqueous layer-by-layer epitaxy of type-II CdTe/CdSe quantum dots with near-infrared fluorescence for bioimaging applications. *Small*, 5(2):185–189, 2009.
- [44] Z. Ning, H. Tian, C. Yuan, Y. Fu, H. Qin, L. Sun, and H. Ågren. Solar cells sensitized with type-II ZnSe–CdS core/shell colloidal quantum dots. *Chemical Communications*, 47(5):1536–1538, 2011.
- [45] M.C. Payne, M.P. Teter, D.C. Allan, T.A. Arias, and J.D. Joannopoulos. Iterative minimization techniques for ab initio total-energy calculations: molecular dynamics and conjugate gradients. *Reviews of Modern Physics*, 64:1045, 1992.

- [46] E. Schrödinger. *Quantisierung als Eigenwertproblem*. *Annalen der physik*, 1926.
- [47] D. Chatfield. *Essentials of Computational Chemistry: Theories and Models*. Wiley, New York, 2002.
- [48] M. Born and R. Oppenheimer. Zur Quantentheorie der Molekeln. *Annalen der physik*, 389(20):457–484, 1927.
- [49] U. Barth and C.D. Gelatt. Validity of the frozen-core approximation and pseudopotential theory for cohesive energy calculations. *Physical Review B*, 21(6):2222, 1980.
- [50] W. Pauli. Über den Zusammenhang des Abschlusses der Elektronengruppen im Atom mit der Komplexstruktur der Spektren. *Zeitschrift für Physik*, 31(1):765–783, 1925.
- [51] D.R. Hartree. The wave mechanics of an atom with a non-coulomb central field, part I-II. *Mathematical Proceedings of the Cambridge Philosophical Society*, 24(1):89–110,111–132, 1928.
- [52] V. Fock. Näherungsmethode zur Lösung des quantenmechanischen Mehrkörperproblems. *Zeitschrift für Physik*, 61(1-2):126–148, 1930.
- [53] A.L. Fetter and J.D. Walecka. *Quantum Theory of Many-Particles Systems*. McGraw-Hill, New York, 1971.
- [54] I. Morgenstern. Quantum-Monte-Carlo simulations for fermionic systems. *Zeitschrift für Physik B Condensed Matter*, 77(2):267–273, 1989.
- [55] P. Hohenberg and W. Kohn. Inhomogeneous electron gas. *Physical Review*, 136(3B):B864, 1964.
- [56] W.Kohn and L.J. Sham. Self-consistent equations including exchange and correlation effects. *Physical Review*, 140(4A):1133–1138, 1965.
- [57] R. Stowasser and R. Hoffmann. What do the Kohn-Sham orbitals and eigenvalues mean. *Journal of the american chemical society*, 121(14):3414–3420, 1999.
- [58] M.S. Hybertsen and S.G. Louie. Electron correlation in semiconductors and insulators: band gaps and quasiparticle energies. *Physical Review B*, 34(8):5390–5413, 1986.

- 
- [59] F. Aryasetiawan and O. Gunnarsson. The GW method. *Reports on Progress in Physics*, 61:237, 1998.
- [60] W. Kohn and L.J. Sham. Quantum density oscillations in an inhomogeneous electron gas. *Physical Review*, 137(6A):A1697, 1965.
- [61] P. Mori-Sánchez, A.J. Cohen, and W. Yang. Localization and delocalization errors in density functional theory and implications for band-gap prediction. *Physical Review Letters*, 100(14):146401, 2008.
- [62] J.P. Perdew, K. Burke, and M. Ernzerhof. Generalized gradient approximation made simple. *Physical review letters*, 77(18):3865, 1996.
- [63] J.P. Perdew, M. Ernzerhof, and K. Burke. Rationale for mixing exact exchange with density functional approximations. *The Journal of chemical physics*, 105(22):9982–9985, 1996.
- [64] A.D. Becke. Density-functional exchange-energy approximation with correct asymptotic behavior. *Physical Review A*, 38(6):3098, 1988.
- [65] P.R.T. Schipper, O.V. Gritsenko, and E.J. Baerends. Kohn-Sham potentials corresponding to Slater and Gaussian basis set densities. *Theoretical Chemistry Accounts*, 98(1):16–24, 1997.
- [66] F. Bloch. Über die Quantenmechanik der Elektronen in Kristallgittern. *Zeitschrift für Physik*, 52(7-8):555–600, 1929.
- [67] B. Oetzel, M. Preuss, F. Ortman, K. Hannewald, and F. Bechstedt. Quantum transport through nanowires: ab initio studies using plane waves and supercells. *Physica status solidi (b)*, 245(5):854–858, 2008.
- [68] J. Ihm and M.L. Cohen. Self-consistent pseudopotential calculations of the equilibrium properties of bulk and surface Si. *Solid State Communications*, 29(10):711–714, 1979.
- [69] L.-W. Wang and J. Li. First-principles thousand-atom quantum dot calculations. *Physical Review B*, 69(15):153302, 2004.
- [70] J.R. Cárdenas and G. Bester. Atomic effective pseudopotentials for semiconductors. *Physical Review B*, 86(11):115332, 2012.
- [71] L. Kleinman and D.M. Bylander. Efficacious form for model pseudopotentials. *Physical Review Letters*, 48(20):1425, 1982.

- [72] A. Franceschetti, H. Fu, L.-W. Wang, and A. Zunger. Many-body pseudopotential theory of excitons in InP and CdSe quantum dots. *Physical Review B*, 60(3):1819–1829, 1999.
- [73] F. Zirkelbach, P.Y. Prodhomme, P. Han, R. Cherian, and G. Bester. Large-scale atomic effective pseudopotential program including an efficient spin-orbit coupling treatment in real space. *Physical Review B*, 91(7):075119, 2015.
- [74] N.Troullier and J.L. Martins. Efficient pseudopotentials for plane-wave calculations. *Physical Review B*, 43(3):1993–2006, 1991.
- [75] A. Franceschetti and A. Zunger. Direct pseudopotential calculation of exciton Coulomb and exchange energies in semiconductor quantum dots. *Physical Review Letters*, 78(5):915–918, 1997.
- [76] L.-W. Wang, A. Franceschetti, and A. Zunger. Million-atom pseudopotential calculation of  $\Gamma$ -X mixing in GaAs/AlAs superlattices and quantum dots. *Physical Review Letters*, 78(14):2819, 1997.
- [77] F.A. Reboledo and A. Zunger. Surface-passivation-induced optical changes in Ge quantum dots. *Physical Review B*, 63(23):235314, 2001.
- [78] L.-W. Wang, M. Califano, A. Zunger, and A. Franceschetti. Pseudopotential theory of Auger processes in CdSe quantum dots. *Physical Review Letters*, 91(5):056404, 2003.
- [79] G. Bester, S. Nair, and A. Zunger. Pseudopotential calculation of the excitonic fine structure of million-atom self-assembled  $\text{In}(1-x)\text{Ga}(x)\text{As}/\text{GaAs}$  quantum dots. *Physical Review B*, 67(16):161306, 2003.
- [80] L.-W. Wang and A. Zunger. Local-density-derived semiempirical pseudopotentials. *Physical Review B*, 51:17398, 1995.
- [81] H. Fu and A. Zunger. Local-density-derived semiempirical nonlocal pseudopotentials for InP with applications to large quantum dots. *Physical Review B*, 55(3):1642–1653, 1997.
- [82] Y.H. Li, X.G. Gong, and S.H. Wei. Ab initio all-electron calculation of absolute volume deformation potentials of IV-IV, III-V, and II-VI semiconductors: the chemical trends. *Physical Review B*, 73(24):245206, 2006.
- [83] A.L. Efros, M. Rosen, M. Kuno, M. Nirmal, D.J. Norris, and M. Bawendi. Band-edge exciton in quantum dots of semiconductors with a degenerate valence band: dark and bright exciton states. *Physical Review B*, 54(7):4843, 1996.

- 
- [84] H. Bui, A. Karpulevich, and G. Bester. Excitonic fine structure of zincblende and wurtzite colloidal CdSe nanocrystals and comparison to effective mass results. *Physical Review B*, accepted, 2020.
- [85] J.C. Slater. The theory of complex spectra. *Physical Review*, 34(10):1293, 1929.
- [86] G. Bester. Electronic excitations in nanostructures: an empirical pseudopotential based approach. *Journal of Physics: Condensed Matter*, 21(2):023202, 2009.
- [87] C.D. Sherrill. *An introduction to configuration interaction theory*. School of Chemistry and Biochemistry, Georgia Institute of Technology, 1995.
- [88] N.S. Ostlund and A. Szabo. *Modern quantum chemistry: introduction to advanced electronic structure theory*. Macmillan, 1982.
- [89] L. Banyai, P. Gilliot, Y.Z. Hu, and S.W. Koch. Surface polarization instabilities of electron-hole pairs in semiconductor quantum dots. *Physical Review B*, 45(24):14136–14142, 1992.
- [90] L.E. Brus. A simple model for the ionization potential, electron affinity, and aqueous redox potentials of small semiconductor crystallites. *The Journal of chemical physics*, 79(11):5566–5571, 1983.
- [91] A. Franceschetti and A. Zunger. Pseudopotential calculations of electron and hole addition spectra of InAs, InP, and Si quantum dots. *Physical Review B*, 62(4):2614–2623, 2000.
- [92] C. Delerue, M. Lannoo, and G. Allan. Excitonic and quasiparticle gaps in Si nanocrystals. *Physical Review Letters*, 84(11):2457–2460, 2000.
- [93] X. Cartoixa and L.-W. Wang. Microscopic dielectric response functions in semiconductor quantum dots. *Physical Review Letters*, 94(23):236804, 2005.
- [94] A. Karpulevich, H. Bui, Z. Wang, S. Hapke, C. Palencia Ramirez, H. Weller, and G. Bester. Dielectric response function for colloidal semiconductor quantum dots. *The Journal of chemical physics*, 151(22):224103, 2019.
- [95] J. Perez-Conde, A.K. Bhattacharjee, M. Chamarro, P. Lavallard, V.D. Petrikov, and A.A. Lipovskii. Photoluminescence Stokes shift and exciton fine structure in CdTe nanocrystals. *Physical Review B*, 64(11):113303, 2001.

- [96] Z. Yu, J. Li, D.B. O'Connor, L.-W. Wang, and P.F. Barbara. Large resonant stokes shift in CdS nanocrystals. *The Journal of Physical Chemistry B*, 107(24):5670–5674, 2003.
- [97] M. Nirmal, D.J. Norris, M. Kuno, M.G. Bawendi, A.L. Efros, and M. Rosen. Observation of the “dark exciton” in CdSe quantum dots. *Physical Review Letters*, 75(20):3728, 1995.
- [98] D.C. Harris and M.D. Bertolucci. *Symmetry and spectroscopy: an introduction to vibrational and electronic spectroscopy*. Courier Corporation, 1989.
- [99] L.-W. Wang and A. Zunger. Pseudopotential calculations of nanoscale CdSe quantum dots. *Physical Review B*, 53(15):9579, 1996.
- [100] P.A. Graf, K. Kim, W.B. Jones, and L.-W. Wang. Surface passivation optimization using DIRECT. *Journal of Computational Physics*, 224(2):824–835, 2007.
- [101] M. Califano, G. Bester, and A. Zunger. Prediction of a shape-induced enhancement in the hole relaxation in nanocrystals. *Nano letters*, 3:1197, 2003.
- [102] C. Sevik and C. Bulutay. Auger recombination and carrier multiplication in embedded Si and Ge nanocrystals. *Physical Review B*, 77(12):125414, 2008.
- [103] S. Baskoutas and G. Bester. Transition in the optical emission polarization of ZnO nanorods. *Journal of Physical Chemistry C*, 115(32):15862–15867, 2011.
- [104] A. Molina-Sánchez, A. García-Cristóbal, and G. Bester. Semiempirical pseudopotential approach for nitride-based nanostructures and ab initio based passivation of free surfaces. *Physical Review B*, 86(20):205430, 2012.
- [105] L.-W. Wang and A. Zunger. Electronic structure pseudopotential calculations of large (approximate to 1000 atoms) Si quantum dots. *J. Phys. Chem.*, 98(8):2158, 1994.
- [106] J.T. Hu, L.S. Li, W.D. Yang, L. Manna, L.-W. Wang, and A.P. Alivisatos. Linearly polarized emission from colloidal semiconductor quantum rods. *Science*, 292(5524):2060–2063, 2001.
- [107] M. Califano and A. Zunger. Anisotropy of interband transitions in InAs quantum wires: an atomistic theory. *Physical Review B*, 70(16):165317, 2004.
- [108] M.S. Nikolic, M. Krack, V. Aleksandrovic, A. Kornowski, S. Förster, and H. Weller. Tailor-made ligands for biocompatible nanoparticles. *Angew. Chem. Int. Edit.*, 45(39):6577–6580, 2006.

- 
- [109] V.I. Klimov, S.A. Ivanov, J. Nanda, M. Achermann, I. Bezel, J.A. McGuire, and A. Piryatinski. Single-exciton optical gain in semiconductor nanocrystals. *Nature*, 447(7143):441–446, 2007.
- [110] Z. Hens and C.J. Martins. A solution NMR toolbox for characterizing the surface chemistry of colloidal nanocrystals. *Chemistry of Materials*, 25(8):1211–1221, 2013.
- [111] P.D. Howes, R. Chandrawati, and M.M. Stevens. Colloidal nanoparticles as advanced biological sensors. *Science*, 346(6205):1247390–1247390, 2014.
- [112] M.V. Kovalenko, L. Manna, A. Cabot, Z. Hens, D.V. Talapin, C.R. Kagan, R. Cherie, V.I. Klimov, A.L. Rogach, P. Reiss, D.J. Milliron, P. Guyot-Sionnest, G. Konstantatos, W.J. Parak, T. Hyeon, B.A. Korgel, C.B. Murray, and W. Heiss. Prospects of nanoscience with nanocrystals. *ACS nano*, 9(2):1012–1057, 2015.
- [113] S.A. Fischer, A.M. Crotty, S.V. Kilina, S.A. Ivanov, and S. Tretiak. Passivating ligand and solvent contributions to the electronic properties of semiconductor nanocrystals. *Nanoscale*, 4(3):904–914, 2012.
- [114] N. Yazdani, D. Bozyigit, K. Vuttivorakulchai, M. Luisier, I. Infante, and V. Wood. Tuning electron–phonon interactions in nanocrystals through surface termination. *Nano letters*, 18(4):2233–2241, 2018.
- [115] J.H. Morkath. Probing the role of capping ligands, ligand loss and solvent effects on the optoelectronic properties of CdS quantum dots. *Journal of Physics and Chemistry of Solids*, 131:10–14, 2019.
- [116] C.M. Evans, L.C. Cass, K.E. Knowles, D.B. Tice, R.P. Chang, and E.A. Weiss. Review of the synthesis and properties of colloidal quantum dots: the evolving role of coordinating surface ligands. *Journal of Coordination Chemistry*, 65(13):2391–2414, 2012.
- [117] R. Resta. Thomas-Fermi dielectric screening in semiconductors. *Physical Review B*, 16(6):2717–2722, 1977.
- [118] H. Haken. Kopplung nichtrelativistischer Teilchen mit einem Quantisierten Feld. *Il Nuovo Cimento*, 3:1230–1253, 1956.
- [119] D.R. Penn. Wave-number dependent dielectric function of semiconductors. *Physical Review*, 128(5):2093–2097, 1962.
- [120] O. Madelung. *Semiconductors: data handbook*. Springer, 2012.

- [121] A.M. Smith, A.M. Mohs, and S. Nie. Tuning the optical and electronic properties of colloidal nanocrystals by lattice strain. *Nature nanotechnology*, 4(1):56–63, 2009.
- [122] X. Gonze, B. Amadon, P.M. Anglade, J.M. Beuken, F. Bottin, P. Boulanger, F. Bruneval, D. Caliste, M. Côté, T. Deutsch, L. Genovese, P. Ghosez, M. Giantomassi, S. Goedecker, D.R. Hamann, P. Hermet, G. Jomard, S. Leroux, M. Mancini, S. Mazevet, M.J.T. Oliveira, G. Onida, Y. Pouillon, T. Rangel, G.M. Rignanese, D. Sangalli, R. Shaltaf, M.J. Verstraete, and J.W. Zwanziger. ABINIT: first-principles approach to material and nanosystem properties. *Computer Physics Communications*, 180(12):2582–2615, 2009.
- [123] T.A. Arias, M.C. Payne, and J.D. Joannopoulos. Ab initio molecular-dynamics techniques extended to large-length-scale systems. *Physical Review B*, 45:1538, 1992.
- [124] P.N. Keating. Effect of invariance requirements on the elastic strain energy of crystals with application to the diamond structure. *Physical Review*, 145(2):637–645, 1966.
- [125] D. Camacho and Y.M. Niquet. Application of Keating’s valence force field model to non-ideal wurtzite materials. *Physica E*, 42:1361–1364, 2010.
- [126] E. Deligoz, K. Colakoglu, and Y. Ciftci. Elastic, electronic, and lattice dynamical properties of CdS, CdSe, and CdTe. *Physica B: Condensed Matter*, 373(1):124–130, 2006.
- [127] P. Han and G. Bester. Interatomic potentials for the vibrational properties of III-V semiconductor nanostructures. *Physical Review B*, 83(17):174304, 2011.
- [128] X. Gonze, J.M. Beuken, R. Caracas, F. Detraux, M. Fuchs, G.M. Rignanese, L. Sindic, M. Verstraete, G. Zerah, F. Jollet, and M. Torrent. First-principles computation of material properties: the ABINIT software project. *Computational Materials Science*, 25(3):478–492, 2002.
- [129] J. Kobljar and M.R. Pederson. Accurate forces in a local-orbital approach to the local-density approximation. *Physical Review B*, 42(6):3276, 1990.
- [130] A. Karpulevich, H. Bui, D. Antonov, P. Han, and G. Bester. Nonspherical atomic effective pseudopotentials for surface passivation. *Physical Review B*, 94(20):205417, 2016.
- [131] X. Huang, E. Lindgren, and J.R. Chelikowsky. Surface passivation method for semiconductor nanostructures. *Physical Review B*, 71(16):165328, 2005.

- 
- [132] D. Ahn. Intervalley interactions in Si quantum dots. *Journal of Applied Physics*, 98(3):033709, 2005.
- [133] M.S. Levinshtein, editor. *Handbook series on semiconductor parameters*. World Scientific, 1997.
- [134] Y. Hinuma, A. Grüneis, G. Kresse, and F. Oba. Band alignment of semiconductors from density-functional theory and many-body perturbation theory. *Physical Review B*, 90(15):155405, 2014.
- [135] S.-H. Wei, S.B. Zhang, and A. Zunger. First-principles calculation of band offsets, optical bowings, and defects in CdS, CdSe, CdTe, and their alloys. *Journal of Applied Physics*, 87(3):1304–1311, 2000.
- [136] V. Kocevski, J. Rusz, O. Eriksson, and D.D. Sarma. First-principles study of the influence of different interfaces and core types on the properties of CdSe/CdS core-shell nanocrystals. *Scientific reports*, 5:10865, 2015.
- [137] D.R. Hamann, M. Schlüter, and C. Chiang. Norm-conserving pseudopotentials. *Physical Review Letters*, 43:1494, 1979.
- [138] M.G. Bawendi, M.L. Steigerwald, and L.E. Brus. The quantum mechanics of larger semiconductor clusters (“quantum dots”). *Annual Review of Physical Chemistry*, 41(1):477–496, 1990.
- [139] D. Mourad, A. Guille, T. Aubert, E. Brainis, and Z. Hens. Random-alloying induced signatures in the absorption spectra of colloidal quantum dots. *Chemistry of Materials*, 26:6852–6862, 2014.
- [140] D. Mourad. Structure-related optical fingerprints in the absorption spectra of colloidal quantum dots: Random alloy vs. core/shell systems. *Journal of Applied Physics*, 121:014307, 2017.
- [141] Y. Al-Douri, H. Baaziz, Z. Charifi, R. Khenata, U. Hashim, and M. Al-Jassim. Further optical properties of CdX (X= S, Te) compounds under quantum dot diameter effect: Ab initio method. *Renewable Energy*, 45:232–236, 2012.
- [142] L. Ding, T.P. Chen, Y. Liu, C.Y. Ng, and S. Fung. Optical properties of silicon nanocrystals embedded in a SiO<sub>2</sub> matrix. *Physical Review B*, 72:125419, 2005.
- [143] Y. Al-Douri, N. Badi, and C. H. Voon. Synthesis of carbon-based quantum dots from starch extracts: Optical investigations. *Luminescence*, 33(2):260–266, 2018.

- [144] C. Delerue, M. Lannoo, and G. Allan. Concept of dielectric constant for nanosized systems. *Physical Review B*, 68(11):115411, 2003.
- [145] O. Zakharov, A. Rubio, X. Blase, M.L. Cohen, and S.G. Louie. Quasiparticle band structures of six II-VI compounds: ZnS, ZnSe, ZnTe, CdS, CdSe, and CdTe. *Physical Review B*, 50(15):10780–10787, 1994.
- [146] M. Dong, J. Zhang, and J. Yu. Effect of effective mass and spontaneous polarization on photocatalytic activity of wurtzite and zinc-blende zns. *APL Materials*, 3(10):104404, 2015.
- [147] L. Dai, R. Lesyuk, A. Karpulevich, A. Torche, G. Bester, and C. Klinkel. From wurtzite nanoplatelets to zinc blende nanorods: Simultaneous control of shape and phase in ultrathin ZnS nanocrystals. *The Journal of Physical Chemistry Letters*, 10(14):3828–3835, 2019.
- [148] R. Chen, D. Li, B. Liu, Z. Peng, G.G. Gurzadyan, Q. Xiong, and H. Sun. Optical and excitonic properties of crystalline ZnS nanowires: toward efficient ultraviolet emission at room temperature. *Nano letters*, 10(12):4956–4961, 2010.
- [149] H. Fang, H.A. Bechtel, E. Plis, M.C. Martin, S. Krishna, E. Yablonovitch, and A. Javey. Quantum of optical absorption in two-dimensional semiconductors. *Proceedings of the National Academy of Sciences*, 110(29):11688–11691, 2013.
- [150] R.W. Meulenbergh, J.R. Lee, A. Wolcott, J.Z. Zhang, L.J. Terminello, and T. Van Buuren. Determination of the exciton binding energy in CdSe quantum dots. *ACS nano*, 3(2):325–330, Jan 2009.
- [151] O.I. Mičić, S.P. Ahrenkiel, and A.J. Nozik. Synthesis of extremely small InP quantum dots and electronic coupling in their disordered solid films. *Applied Physics Letters*, 78(25):4022–4024, 2001.
- [152] E. Cho, H. Jang, J. Lee, and E. Jang. Modeling on the size dependent properties of InP quantum dots: a hybrid functional study. *Nanotechnology*, 24:215201, 2013.
- [153] Z. Ning, M. Molnàr, Y. Chen, P. Friberg, L. Gan, H. Ågren, and Y. Fu. Role of surface ligands in optical properties of colloidal CdSe/CdS quantum dots. *Physical Chemistry Chemical Physics*, 13:5848–5854, 2011.
- [154] S.N. Inamdar, P.P. Ingole, and S.K. Haram. Determination of band structure parameters and the quasi-particle gap of CdSe quantum dots by cyclic voltammetry. *ChemPhysChem*, 9:2574–2579, 2008.

- [155] J. Jasieniak, L. Smith, J. Van Embden, P. Mulvaney, and M. Califano. Re-examination of the size-dependent absorption properties of CdSe quantum dots. *Journal of Physical Chemistry C*, 113:19468–19474, 2009.
- [156] W.W. Yu, L. Qu, W. Guo, and X. Peng. Experimental determination of the extinction coefficient of CdTe, CdSe, and CdS nanocrystals. *Chemistry of Materials*, 15:2854–2860, 2003.
- [157] D. Kong, Y. Jia, Y. Ren, Z. Xie, K. Wu, and T. Lian. Shell-thickness-dependent biexciton lifetime in type I and quasi-type II CdSe/CdS core/shell quantum dots. *Journal of Physical Chemistry C*, 122(25):14091–14098, 2018.

# Acknowledgements

At first, I would like to thank my supervisor, Prof. Dr. Gabriel Bester for giving me the opportunity to do very challenging and interesting research, for constant advising and guidance through the PhD studies.

I would like to acknowledge Prof. Dr. Holger Lange for the support as co-advisor, Prof. Dr. Horst Weller and Prof. Dr. Gabriel Bester as the assigned experts for the careful review and grading of the written part, Prof. Dr. Gabriel Bester again together with Prof. Dr. Carmen Herrmann and Prof. Dr. Alf Mews for the participation in the oral examination committee.

I would like to thank my colleagues, namely Dr. Denis Antonov, Dr. Peng Han and Hanh Bui for collaboration on the non-spherical potentials project; Dr. Abderresak Torche for advising and assistance in the project on 2D materials; Dr. Zhi Wang, Hanh Bui and Sören Hapke for collaborative work on the dielectric screening functions project; all mentioned above plus Dr. Elisabeth Dietze, Walter Pfäffle, Jens Hühnert, Fritz Weyhausen-Brinkmann, Surender Kumar and Dr. Torben Steenbock for the sharing ideas, fruitful discussions and friendly support during and beyond the doctoral studies.

Thank you, Dr. Daniel Mourad, Dr. Jerome Jackson, Dr. Elisabeth Dietze and Fritz Weyhausen-Brinkmann for supporting me during the very first months in Hamburg. Very special thanks to Hanh Bui, for more than four years working together side by side, sharing not only working space, but also all successes and failures. Many thanks to Sören Hapke and Benjamin Bolbrinker for the long-term contribution in several projects as student assistants and the inspiration in our joint work. Warm thanks to the team assistant Marie Meins for patience and support all around working and living issues.

Many thanks to Dr. Eugene G. Maksimov for raising my interest in scientific research and in particular in nanoscience during my Diploma program. Very special thanks to Prof. Dr. Christian Klinke and Dr. Rostyslav Lesyuk for beneficial collaboration on the 2D materials study as well as Prof. Dr. Horst Weller and Dr. Cristina Palencia Ramírez for the great collaboration on the dielectric screening functions project, and all of them together plus Felix Bourier for the scientific dis-

cussions and explanations from the experimental point of view.

I am grateful to my friends, especially to Caspar Aumüller, Swjatoslaw Pertschichin, Eduard Lebold, Lev Marchenko, Maria Gordenchuk, Dr. Viktor Valmispild, Evgeny Zolotov, Natascha Frumkina, Daria Hansen, Liza Misonzhnikova, Vladimir Schenikov, Artem Kuznetsov, Grigory Stepanov, Dr. Evelina Nikelshparg and Fedor Balabin for the huge moral and physical support, relevant advising and care, without which I would not be able to withstand during the hard periods.

Last, but not the least, I am grateful to my family, my parents Andrey Karpulevich and Tatiana Khodova, my brother Evgeny Karpulevich and his wife Olga Karpulevich for providing the opportunities and all kinds of support to let me pursue and reach my goals.

Financial support was provided by the Cluster of Excellence “Advanced Imaging of Matter” - EXC 2056 - project ID 390715994 and “The Hamburg Centre for Ultrafast Imaging” - EXC 1074 - project ID 194651731 of the Deutsche Forschungsgemeinschaft (DFG).

# List of Chemicals

No hazardous compounds according to the GHS (Globally Harmonized System of Classification and Labeling of Chemicals) regulation have been used within the scope of this work.



# Declaration on oath

I hereby confirm that I have taken the oath of the present dissertation and that I have not used anything besides the specified materials. The submitted written version corresponds to that on the electronic storage medium. I assure that this dissertation was not submitted in an earlier doctoral procedure.

# Eidesstattliche Versicherung

Hiermit versichere ich an Eides statt, die vorliegende Dissertation selbst verfasst und keine anderen als die angegebenen Hilfsmittel benutzt zu haben. Die eingereichte schriftliche Fassung entspricht der auf dem elektronischen Speichermedium. Ich versichere, dass diese Dissertation nicht in einem früheren Promotionsverfahren eingereicht wurde.

Anastasia Karpulevich  
February 12, 2020